EXPERIMENTAL DYNAMIC CHARACTERIZATION OF META-CONFIGURED STRUCTURES FOR AEROSPACE APPLICATIONS

By

TIMOTHY A. EMERSON

Bachelor of Science in Mechanical Engineering

Oklahoma State University

Stillwater, OK

2018

Submitted to the Faculty of the
Graduate College of the
Oklahoma State University
in partial fulfillment of
the requirements for
the Degree of
MASTER OF SCIENCE
July, 2020

EXPERIMENTAL DYNAMIC CHARACTERIZATION

OF META-CONFIGURED STRUCTURES FOR

AEROSPACE APPLICATIONS

Thesis Approved:

Dr. James Manimala

Thesis Adviser

Dr. James Kidd

Dr. Yujiang Xiang

ACKNOWLEDGEMENTS

To say thank you is an understatement as to how much each person who has made an impact within my life has been a blessing to me. While the list is much longer than what I could ever configure, here is to those who oversaw my last few years.

To Dr. James Manimala, I recently told you that I had looked through my notes and I could see the growth throughout my time under your guidance. I thank you for your continued guidance, continued support, and all the times you felt like I did not understand but never gave up. It was in these moments that I grew the most, this moment would have never been possible without the help you have given me.

To Dr. Kidd and Dr. Good, I thank you for the dedication that you both showed me to help me learn and grow in your classes. Both classes have prepared me for my research and have prepared me for my future within engineering, the knowledge learned will never be forgotten. Thank you also for the time spent helping me on my thesis and research and standing on my committee.

To Dr. Xiang, while our time may have been short I appreciate the ability to step in at the last minute and help guide me in the final steps of my research and standing on my committee.

A special thank you to DARPA for supporting and sponsoring the research done.

To Milkyas Afework and Alexander Svetgoff, the countless times we have shared complaining over the time that we seem to be lacking, the classes shared, the help given, and the friendships have all led to this. You have both given me more help than could have ever been asked for; it is very dearly appreciated.

To Jully Lee and Alessio Lozzi, the countless hours you both spent under my guidance, learning and researching, has helped me to grow as a leader and as a friend. Thank you both for the time spent helping me through my research and through my endeavors. To Bablu, Paul, Sam, Zach, Will, and those who have been through the lab doors, thank you for the continued help and support throughout my graduate research.

To John and Sam Thompson and Tanner Gore, thank you all for the hospitality given for the countless nights I spent away from home. The time spent being there for me is more than I could ever ask for.

To Mr. Hallmark and Mrs. Franklin, thank you for the time spent instilling the love of mathematics and school into my life.

To Blocker Baptist Church, thank you for showing me who I am and always supporting me in whatever endeavors I went on. To those who are closest to me, thank you for the continued support and for helping me grow into who I am.

To my lovely wife, there can never be enough words to thank you for what you have done for me. From encouragement, guidance, support, and love you have shown and given it all to me. Forever can never be long enough…thank you for everything!

To the one that made this all possible the only words I can say are your own words: "Phil. 4:13, I can do all things through God who strengthens me."

Thank you all from the bottom of my heart

Name: TIMOTHY A. EMERSON

Date of Degree: July, 2020

Title of Study: EXPERIMENTAL DYNAMIC CHARACTERIZATION OF META-CONFIGURED STRUCTURES FOR AEROSPACE APPLICATIONS

Major Field: MECHANICAL AND AEROSPACE ENGINEERING

Abstract:

Drawing inspiration from acoustic metamaterials, meta-configuration as a means to improve coactive mechanisms between sub-structures to enhance overall structural performance is investigated with a primary focus on aerospace applications. Two prototypical meta-configured structures for dynamic load manipulation were designed, constructed and experimentally characterized. The first of these is a directional wave guide (DWG) that utilizes tailored spatio-spectral band gap regions to selectively attenuate or propagate frequency components within tunable bandwidths along designated paths. Finite element simulations were performed to evaluate designs for various resonator sub-structures and their patterning within a plate-type wave guide. Relative band structures for the resonators were tuned to span a frequency range from 16 to 20 kHz. The DWG is fabricated by chemically etching a patterned array of cantilever beam-type resonators on a 50-micron thick brass sheet. A custom test-rig consisting of an adjustable mount with low-stiffness boundary, piezo-actuator and a mechanically-staged laser vibrometer was used to conduct the experiments. Overall, reasonable correlation is indicated for the designed versus measured extents for the band gap frequency ranges along each path, although further detuning of global modes and minimization of resonator and boundary variability would help improve correlation. The second prototypical structure investigated is a passive-adaptive tuned vibration absorber (TVA). In contrast to conventional TVAs which are tuned to absorb vibrations within a preset bandwidth, the passive-adaptive TVA would be able to self-tune based solely on the input excitation to deliver appreciable absorption spanning larger bandwidths. An approach based on a riding mass retained under spring force on a cantilever beam resonator is explored for a low-frequency (~40-80 Hz) passive-adaptive TVA. Test articles with various configurations for the riding mass attachment were constructed and dynamically characterized using non-contact transduction techniques. An increase of about 55 % over the mass-equivalent, conventional TVA's absorption bandwidth is obtained for the passive-adaptive TVA without altering its lower bound. These results indicate that meta-configured structures may provide improved solutions in applications such as isolation of payloads from structure-borne vibrations having a meandering dominant frequency content.

TABLE OF CONTENTS

Chapter Page

I. LITERATURE REVIEW 1

Motivation 1
Engineering Structures and Materials 2
Acoustic Metamaterials 3
Meta-Configured Structures 7
Potential Applications 9
Chapter Overviews 11

II. PASSIVE-ADAPTIVE DIRECTIONAL WAVE GUIDE 13

Introduction 13
Material and Methods 22
Experimental Setup 23
Resonator Design 27
Wave Guide Design 33
Test Cases 38
Simulation Modeling 40
Discussion of Results 41
Boundary Stiffness 41
Transient Finite Element Analysis 43
Steady-State Transmissibility Tests 57
Summary 64

III. PASSIVE-ADAPTIVE TUNED VIBRATION ABSORBER 65

Introduction 65
Materials and Methods 69
Experimental Setup 70
Baseline TVA 73
Passive-Adaptive TVA 74
Test Cases 76
Simulation Model 79
Discussion of Results 82
Baseline TVA 82

Chapter ..... Page

Passive-Adaptive TVA 85
Base-Attached TVA 85
Tip-Attached TVA 93
Summary 101

IV. CONCLUSIONS AND RECCOMMENDATIONS 103

Summary and Conclusions 103
Recommendations for Future Research 105
Wave Guide 105
Tuned Vibration Absorbers 107

REFERENCES 109

APPENDICES 116

Appendix A 116
Metamaterials-Inspired Smart Composite 116
Appendix B 122
Base-Attached PATVA 'Left' Cantilever Results 122
Tip-Attached PATVA 'Left' Cantilever Results 125

LIST OF TABLES

Table Page

2.1: Geometric details of built-in resonators in the passive-adaptive wave guide....32

2.2: Wave guide and built-in resonator simulation and experimental test cases 40

2.3: FEM mesh convergence study for the passive-adaptive wave guide's simulation model.....41

2.4: Summary of foam boundary stiffness investigation 43

2.5: Band gap frequency ranges for the built-in resonators in the passive-adaptive wave guide 47

3.1: Torqueing guidelines chart 73

3.2: Summary of tip-attached PATVA test cases 79

3.3: FEM mesh convergence study for the TVAs simulation model.....80

3.4: Summary of base-attached TVA test cases.....86

LIST OF FIGURES

Figure Page

2.1: (a) Components of the experimental set-up and (b) schematic depiction of the wave rejection test article.....14

2.2: Displacement transmissibility versus excitation frequency at various monitoring locations on the wave rejection test article under low excitation amplitude conditions. 15

2.3: Displacement transmissibility versus excitation frequency at various monitoring locations on the wave rejection test article under high excitation amplitude conditions 16

2.4: Photograph of the wave sorting test article (left) showing resonator types and its schematic depiction (right) showing monitoring locations.....17

2.5: Normalized displacement transmissibility spectra for (a) the input monitored at location P00 and the outputs monitored at locations (b) P50, (c) P05 and (d) P55 for high amplitude input excitation 18

2.6: Normalized displacement transmissibility spectra for (a) the input monitored at location P00 and the outputs monitored at locations (b) P50, (c) P05 and (d) P55 for high amplitude input excitation 19

2.7: Band gap regions with spatial configuration of resonator units – the colored line contours correlate to the area where the resonator of the same color is missing.....21

2.8: Relative band gap structures corresponding to the R0-R4 resonators of the passive-adaptive directional wave guide 22

2.9: LabVIEW program for data analysis, illustrating the steps and integration process used to obtain the kinematic data.....24

2.10: Passive-adaptive directional wave guide testing apparatus shown with test article mounted.....25

2.11: Wave guide test article mounted on foam boundary 26

Figure Page

2.12: CAD model of the R0 resonator unit with dimensions.....28

2.13: CAD model of the R1 resonator unit with dimensions.....29

2.14: CAD model of the R2 resonator unit with dimensions.....30

2.15: CAD model of the R3 resonator unit with dimensions.....31

2.16: CAD model of the R4 resonator unit with dimensions.....31

2.17: Resonator plate configuration illustrating the directional nomenclature and the resonator type missing along each axial direction 34

2.18: DRIE-mask created to manufacture a micro scale wave guide test article using a silicon wafer 35

2.19: Images of 3-D printed test articles: Left – metal version, Right – polymer version. Both versions give an idea as to the lack of adequate precision in the resonator features required.....36

2.20: Manufactured passive-adaptive directional wave guide test article 37

2.21: First mode shape of R0 resonator at 15739 Hz.....44

2.22: First mode shape of R1 resonator at 15938 Hz.....45

2.23: First mode shape of R2 resonator at 16321 Hz.....45

2.24: First mode shape of R3 resonator at 16883 Hz.....46

2.25: First mode shape of R4 resonator at 17702 Hz.....46

2.26: First (global) mode shape of the wave guide at 94.1 Hz 47

2.27: Frequency spectra of the output responses at the axial monitoring locations for a harmonic input of 16 kHz at the center 49

2.28: Frequency spectra of the output responses at the axial monitoring locations for a harmonic input of 17 kHz at the center 50

2.29: Frequency spectra of the output responses at the axial monitoring locations for a harmonic input of 18 kHz at the center 51

Figure Page

2.30: Frequency spectra of the output responses at the axial monitoring locations for a harmonic input of 19 kHz at the center 52

2.31: Frequency spectra of the output responses at the axial monitoring locations for a harmonic input in the North direction (R1 missing) 53

2.32: Frequency spectra of the output responses at the axial monitoring locations for a harmonic input in the West direction (R2 missing) 54

2.33: Frequency spectra of the output responses at the axial monitoring locations for a harmonic input in the South direction (R3 missing) 55

2.34: Frequency spectra of the output responses at the axial monitoring locations for a harmonic input in the East direction (R4 missing) 56

2.35: Displacement transmissibility versus excitation frequency for the passive-adaptive wave guide test article monitored at the North location under steady-state condition 59

2.36: Displacement transmissibility versus excitation frequency for the passive-adaptive wave guide test article monitored at the East location under steady-state condition 60

2.37: Displacement transmissibility versus excitation frequency for the passive-adaptive wave guide test article monitored at the South location under steady-state condition 61

2.38: Displacement transmissibility versus excitation frequency for the passive-adaptive wave guide test article monitored at the West location under steady-state condition 62

2.39: Displacement transmissibility versus excitation frequency for the passive-adaptive wave guide test article monitored at the South-East location under steady-state condition 63

3.1: SolidWorks model of the base attachment fixture for the TVA test articles 71

3.2: TVA experimental set-up showing various components involved 72

3.3: Constructed baseline TVA using washers to act as the tip mass 74

3.4: CAD model of the baseline TVA with dimensions in m 74

3.5: PATVA riding mass installation 75

Figure Page

3.6: Base-attached PATVA configuration showing the riding mass configuration..76

3.7: CAD modeled base-attached PATVA showing locations of the parts 77

3.8: CAD model of tip-attached PATVA showing its components.....77

3.9: TVA finalized mesh obtained through Abaqus 80

3.10: Cantilever first mode shape at 18.9 Hz from FEM.....81

3.11: First mode shape of the Baseline TVA, with a frequency of 53.72 Hz 83

3.12: TVA vibration testing monitoring locations.....84

3.13: Normalized displacement transmissibility results for the nonlinear base-attached TVA with 3 tip and 1 riding masses 88

3.14: Normalized displacement transmissibility results for the base-attached PATVA with 3 tip and 2 riding masses 89

3.15: Normalized displacement transmissibility results for the base-attached PATVA with 3 tip and 3 riding masses 90

3.16: Normalized displacement transmissibility results for the base-attached PATVA with 2 tip and 1 riding masses 91

3.17: Normalized displacement transmissibility results for the base-attached PATVA with 1 tip and 2 riding masses 92

3.18: Normalized displacement transmissibility results for the tip-attached PATVA with 3 tip and 1 riding masses 95

3.19: Normalized displacement transmissibility results for the tip-attached PATVA with 3 tip and 2 riding masses 96

3.20: Normalized displacement transmissibility results for the tip-attached PATVA with 3 tip and 3 riding masses 97

3.21: Normalized displacement transmissibility results for the tip-attached PATVA with 2 tip and 1 riding masses 98

3.22: Normalized displacement transmissibility results for the tip-attached PATVA with 1 tip and 2 riding masses 99

Figure Page

3.23: D_5^* bandwidths of the different TVA cases.....100

3.24: D_5^* bandwidths of the different TVA cases compared to the Baseline TVA .101

LIST OF SYMBOLS AND ABBREVIATIONS

AM	Acoustic Metamaterials
BA	Base-Attached
BL	Baseline
DAQ	Data Acquisitioning System
D*	Normalized Displacement Transmissibility
DRIE	Deep Reactive-Ion Etching
DWG	Directional Wave Guide
E	Young's Modulus
EM	Electromagnetic
f_n	Natural Frequency
FEM	Finite Element Modeling
FFT	Fast Fourier Transform
I	Area Moment of Inertia
k	Stiffness
L	Cantilever Arm Length
LR	Left Riding Mass
LT	Left Tip Mass
m_1	Non-Resonating Mass
m_2	Resonating Mass
m_{eqv}	Mass Equivalent

MEMS	Micro-Electro-Mechanical Systems
MISC	Metamaterials-Inspired Smart Composites
MRE	Magnetorheological Elastomer
NLAM	Nonlinear Acoustic Metamaterial
ρ	Density
PATVA	Passive-Adaptive Tuned Vibration Absorber
RR	Right Riding Mass
RT	Right Tip Mass
SMA	Shape-Memory-Alloys
TA	Tip-Attached
TVA	Tuned Vibration Absorber
ν	Poisson's Ratio
ω	Circular Frequency
ω_L	Lower Bound of the Band Gap
ω_U	Upper Bound of the Band Gap

CHAPTER I

LITERATURE REVIEW

1.1 Motivation

Current studies within engineering has pushed towards the ability to enhance performance and capabilities through the addition of novel materials. Within the work presented it is the goal to introduce the term of meta-configuration, give examples of meta-configurations, and give concept of how they impact the future of materials. To design a meta-configured structure the concepts within metamaterials are introduced, and an understanding of the ability to engineer features at the local level is presented.

Drawing inspiration from current research, the studies have been expanded to encompass wave guiding techniques at a micro-electro-mechanical systems (MEMS) scale and the ability to passive-adaptively implement a bandwidth that expands the capabilities of a baseline tuned vibration absorber.

The research presented gives experimental approaches to the concepts of dynamic characterization within engineered structures, utilizing their local resonant features. The modal responses of the structures are studied to understand the wave guiding and vibration isolation techniques presented. The findings and limitations of the techniques are discussed and areas of expansion are given for further research capabilities.

1.2 Engineered Structures and Materials

Engineering structures and materials have expanded towards tailored performances for damping capabilities [1], microstructure incorporation [2], and tunable band gaps [3]. To broaden the existing materials scientists and engineers are exploring new configurations to achieve desired dynamic characteristics. For example, increasing damping in civil structures exposed to seismic vibration [4] can improve their resistance to damage by reducing peak loads. By taking a more multifaceted approach to solve these problems, the ability to enhance performance and implement a more diverse set of functionalities becomes more apparent. This allows for advances in a wide variety of concepts to be incorporated into structures that furthers the innovation in different fields in both commercial and industrial applications.

In the optical domain, enhancements such as tuning an optical band gap to vary light by producing optical variants that completely hide or cloak an object from view, led to studies in optical wave guiding [5]. The progress in the study of light and photonic applications have led to novel utilizations and a unique understand, while also introducing an ability to manipulate other energy forms. These advances in technology can be used as a basis for further research in other fields such as acoustics and structural dynamics as well, taking the concepts such as an ability to tune a band gap or controlling damping effects. This would lead to more synergistic or multifunctional capabilities for engineered structures, which is desirable when addressing emerging challenges.

In order to design and manufacture such materials or structures a more holistic approach to design needs to be taken where configurations address several competing requirements through innovative interactions between constituent materials and structures. As material scientists continue to create new material variants, structural engineers take advantage of unique design approaches using current materials to enrich the functionalities obtainable in applications.

1.3 Acoustic Metamaterials

In the last few decades, Acoustic Metamaterials (AM) have been researched and developed in order to realize the unique effects that they can exhibit. A metamaterial can be classified as an artificial material that exhibit dynamic features that differ from the parent material. These features themselves can extend to and encompass a wide variety of functions. The functions themselves can vary from manipulation of mechanical wave passage through AM to reconfiguration of functionalities such as stiffness, density or conformity for instance based on external dynamic inputs. Examples of specific implementations include the use of phononic crystals and their inherent deep subwavelength behavior to enable negative stiffness [6], negative effective bulk moduli, and negative effective mass density [7-8]. The effect of the negative mass density has been studied extensively by Huang et al. [9-11], the basis behind the work is the use of a mass in mass system and the frequency dependency of the response.

The study of acoustic cloaking using AMs, by Norris et al. [12], focused on the ability to mask objects from acoustic probing using transformation mapping techniques. Sought after in defense applications, as it gives the ability to redirect a wave and gives a cloaked effect to the object of interest. The study has shown that the material composition is dependent on an anisotropic parameter such as stiffness or mass. In example, when considering stiffness an infinitely large cloak would be required; however, the finite mass case can be achieved by seeking an anisotropic stiffness. The performance of an acoustic cloak can also be extended by increasing variations in the local engineered configurations within the structure [13]. This allows for the encompassed area to be imperceptible to acoustic probing along a designated path. A similar concept is used in the current study by adding multiple unit types with different features to enrich wave manipulation.

Metamaterials initially introduced within the realm of electromagnetic (EM) wave propagation, however, due to their analogous relationship with acoustic metamaterials [14] they

were introduced into the realm of acoustics. Since the introduction of EMs to the acoustic realm EMs have experienced high success in the direction of technological advances. By studying the energy transmissibility spectrum and the inability of waves to propagate within the band gap [15-16], band gap can be tailored to eliminate propagation for specific frequency ranges. One way to create this structure is via "locally resonant materials" where when the resonance phenomena occurs energy pertaining to the band gap frequency range is sequestered in the local degrees of freedom. This use of a band gap is the prominent feature within such structures. The upper limit of this band gap can be theoretically calculated and outside of the band gap elastic waves will propagate as per the host material's dispersion relationship [17]. Such AM can be tailored by changing the local structures in the locally resonant AM, and the band gap can be tuned to display negative effective properties for frequency ranges of interest. An analysis [18] has been done regarding these claims and further investigations can be shown by involving periodic resonator structures. It was found that the wave attenuation mechanisms were a direct consequence of the sub systems, and the band gaps could be expanded by manipulating these resonant features.

The key idea behind this approach are the integration of "locally resonant features" within host structures or materials. The resultant structures themselves are rendered incapable of permitting mechanical waves within certain frequency ranges to persist within them. There are several specific ways to inherently incorporate such local engineered features or 'microstructures' to achieve wave manipulation and noise isolation. More advanced versions of tuning include space-coiling [19], holey [20-21], and labyrinthine metamaterials [22]. These holey structures are found to be materials that have a series of perforations or holes increasing the energy harvesting capabilities. The concept of the holey structures can be used in ultrasound testing [20] and imaging for engineering materials. The holey structures resonant modes are created by manipulating the metamaterial's parameters of diameter, length and periodicity of the holes. The holey structures

[21] would also give a basis to create a structure with extraordinary resonant features through their transmissibility capacities.

The use of locally resonant features has also been employed to study ultrasonography [16, 21] on the MEMS scale, however, it is noted that the ability to test and analyze the system would be easier when done on a larger scale. If the experimental results matched up with the theoretical results on the macroscale it may be possible to apply scaling laws to estimate the behavior at smaller scales. Inasmuch as these "locally resonant" features could be manufactured having a sequence of such resonators within a prescribed pattern would deliver spatial and spectral regimes of attenuation that can be adapted to different application scenarios. The resonators themselves could have invariant bounding dimensions to give a form of symmetry, however, the local mass (or stiffness) of the resonators themselves could be modified to tune their response at specific locations in the spatial array.

An example from nature for structured wave guides is found in the method of acoustic reception in Porpoises. Porpoises use a similar type of wave manipulation [23] and acoustic cloaking techniques being investigated within this study, the similarities are worth discussing when compared to the research being presented. The porpoises emit a biosonar sound beam allowing for wave manipulations in the omnidirectional fields, when a surface is reached the wave is reflected back. This emission of the waves in different fields is what is being searched for with the wave guide, however, in the wave guides case wave manipulation is sought after to direct the waves within a plate.

Recent studies have brought to light the characteristics of nonlinear acoustic metamaterials (NLAM) [24] in which plate-type NLAM are introduced and studied to understand their wave manipulation behavior. These structures give a better understanding of what happens when incorporating nonlinearity into subcomponents of the plate-type wave guide being considered. One

parameter that can be changed is that of the finite-strain [25], this incorporates a nonlinearity, which can be modeled by an array of nonlinear spring-mass resonator attachments. The study done by Khajehtourian *et al*. [25] incorporates a 1-D structure and shows that both location and size of the band gap is changed by the nonlinearity, however, the nonlinearity also gives rise to a dual band gap formation. This gives rise to the wave guide in which the formation of band gaps can be manipulated by varying not just the in-out excitation's frequency but also its amplitude. A 2-D study on elastic metamaterials introducing Kirchhoff-Love plates [26] is done by Al Ba'ba'a et al in order to predict the local resonance band gap(s) more accurately and to understand potential for energy harvesting.

Plate modes also extend to the concept of vibration suppression [27]; initial studies demonstrate the ability to design vibration suppression structures by incorporating the resonant absorbers as inclusions. These vibration absorption studies are furthered by investigating the low-end frequency band gap ranges [28] where the Lamb modes and torsional modes tend to couple creating new opportunities for vibration suppression. These Lamb waves are often used as a basis for ultrasound testing and the ability to detect flaws or defects within plates or structures.

Other possible techniques are also employed such as using periodic cells with built in resonances [29] or periodically perforated plates [30] giving enhanced wave manipulation performance in form-factors suitable for various application scenarios.

One of the objectives of the current study is to understand the behavior of wave motion within an AM with patterned resonances and the ability of such a structure to display novel wave manipulation capabilities. By applying the knowledge gained from previous work done with negative effective mass (locally resonant) AM new designs are investigated to achieve specific propagation outcomes. By tailoring the system to have different locally resonant features and tuning their relative spatial and spectral location, wave guides for rejection, steering, sorting or directional

beaming of mechanical waves could be possible. Manipulation of the waves can be engineered for prescribed directions and can have as many different local resonator configurations as needed, however, for illustration only four beaming directions and five different resonator types are used for the passive-adaptive wave guide considered in this study. Such wave guide structures could be classified as a 'meta-configured' structure as described in the ensuing section.

The prime structural composition of the AM would be able to have an optimal sound-absorbent property [31], utilizing the ability to manipulate the band gap of the structure. The AM would also need to have a tailored ability of attenuating the frequencies for the directions of interest. So by using different locally resonant structures sequenced in a unique way and using the techniques of the AM design approach, waves can be caused to attenuate in a specific manner within the AM wave guide.

1.4 Meta-Configured Structures

The acoustic metamaterial field has slowly merged in certain aspects into the studies of Micro-Electro-Mechanical Systems (MEMS), Microsystems [32-33] at one end of the spectrum, and into macroscale applications such as in civil infrastructure for seismic wave mitigation. MEMS devices have become more popular in the recent years since the ability to scale down operations to a miniaturized application enables new mission capabilities. Novel microscale devices can also be used in vibrational energy harvesting [32] (i.e. to harvest energy from ambient vibrations). Such vibration-powered generators are typically composed of a resonant element coupled to a harvesting circuit. In many cases, inertial spring and mass systems are used as the resonant element, however, other configurations are also possible [33]. One of these alternate embodiments are piezoelectric generators [32] which employ piezoelectric materials that generate a current when mechanically stressed. These piezoelectric generators provide a straightforward way to produce electric power

from mechanical deformations, however, their efficiency is low when ambient vibrational amplitudes are small.

The idea behind meta-configured structures is that overall performance is enhanced, or functionalities enriched by coupled interactions between sub-configurations within an overarching structural configuration. The thought is that if the sub-configurations interact synergistically rather than behave as independent entities within the structure then performance and functionality of the overall structure can also be enhanced. Engineering innovative modes of interaction between the sub-configurations which are not otherwise employed, through the use of novel design approaches such as those utilized in AM is key to achieving such an outcome. Therefore, the term 'meta-configuration' has been proposed to denote this approach, since the resultant structure is envisioned to have capabilities beyond conventionally designed structures.

It is of interest to explore parallels to this terminology (meta-configuration) in other areas of study. Within Biology, the term 'meta-configured' has been used to understand competences [34] within the animal kingdom's learning capacity. The diversity of the evolutionary processes and their interactions with development are interpreted in terms of artificial learning and cognitive science [34]. In chemistry, meta-configuration indicates the positions of substituents in aromatic cyclic compounds [35]. The term "meta" can also relate to undergoing transformations such as polymorphism [36], and the ability of the compounds and constituents of the material to remain constant and stable. These concepts can then be tied together in light of a common theme, which focusses on the abilities or capabilities of the sub-system to interact holistically. Therefore, in a similar vein, the proposed terminology of a "meta-configured structure or material" can also be interpreted in the same context as the aforementioned fields.

An exploratory study of meta-configured structures by Emerson et al. [37] investigates a multifunctional plate consisting of cantilever beam type resonators sandwiched between two core

plates. Each core plate is equipped with harvesting coils and neodymium magnets sit in the center of the resonators. The central resonant plate has features of a reentrant cantilever beam design, which utilizes innovative sub-structure designs to obtain the desired low frequency tunability for energy harvesting. The study introduces the capabilities of this Metamaterials-Inspired Smart Composite (MISC), which can be interpreted as a meta-configured structure and the enhanced functionalities demonstrable using such structures for multifunctional applications such as vibration isolation, energy harvesting, sensing and monitoring, a as well as structural load bearing. A summary of the results for the MISC is given in appendix A.

Drawing inspiration from the approach implemented in the MISC, second part of this thesis explores the possibility of implementing a passive-adaptive scheme to expand the bandwidth of isolation for a Tuned Vibration Absorber (TVA). Both this Passive-Adaptive TVA (PATVA) as well as the directional wave guide mentioned earlier that are explored as part of this thesis leverage principles of meta-configuration to enhance overall performance and functionalities. Moreover, the directional wave guide and the PATVA have implications for aerospace applications such as isolation of sensitive payloads on launch vehicles and suppression of aero-structural vibrations arising from low-frequency onboard sources.

1.5 Potential Applications

The primary application focus for the two concepts (directional wave guide and the PATVA) studied in this thesis are for aerospace domain. In several launch and recovery scenarios for aerospace vehicles, sensitive payloads are required to be isolated from ambient structure-borne vibrations while retaining primary load bearing capabilities and structural conformity. In such cases, if the structural disturbance can be steered away from or around the payload, its prospects for survivability are enhanced. The directional wave guide could be employed to achieve this end.

One idea behind the directional wave guide is that a device can be implemented that allows travel of only certain frequencies in prescribed directions. This could also be used for acoustic transduction in collision avoidance [38], sonar-based aids for obstacle detection [39], and location sensing elements [40].

In this sense, the directional wave guide can also be used for applications such as acoustic imaging. Acoustic imaging has been used within the aerospace industry to identify cracks within panels by ways of acoustic emission [41] for structural health monitoring. Other applications for imaging is use of ultrasonic transducers to effectively define early stage tumors [42] and growths. With the ability to focus incident energy pertaining to a signal frequency bandwidth within a specific spatial region while rejecting noise frequency bandwidths, one can imagine the potential of such a wave guide to impact the performance in transduction applications. This opens up possibilities for applications in the medical field as well.

The second concept is that of the passive-adaptive tuned vibration absorbers or PATVA, which could adaptively isolate bandwidth to suit meandering input frequencies and perturbations in its amplitude. This presents a unique and useful feature for certain aerospace applications. For instance, entirely passive TVAs are commonly employed as vibration dampers for aero structures to isolate them from structure-borne disturbances such as those from propellers or engines, which typically have a dominant low-frequency (<~500 Hz) frequency content. Several applications such as this have also been used in controlling the dynamics of wind turbines [43], interior noise control of aircraft [44], and seismic energy absorption [45-46]. For the aerospace case, oftentimes, depending on the flight regimes, the specific frequencies that need to be isolated for can vary due to conditions such as engine or propeller RPM. Therefore, a passive TVA tuned to a specific frequency has limitations as to the bandwidth of isolation that can be provided. Typically, these bandwidths are narrow and hence multiple TVAs tuned to different frequency become necessary. It would be ideal if the TVA has a passive-adaptive capability that inherently tunes its resonance

frequency to suit the input frequency of the disturbance. The PATVA uses an innovative arrangement of sub-systems within the TVA to attempt to broaden the bandwidth of isolation response. It would be even more desirable if this could be achieved without a significant increase in mass, which also a possibility using the PATVA approach is reinforcing its claim to being classified as a meta-configured structure.

1.6 Chapter Overviews

This chapters (Chapter 1) presents an overview of the motivation, literature review, the concept of meta-configuration for structures and an outline of the two new structural configurations to be explored as well as their potential applications. Passive-adaptivity is emphasized as a common theme. Details of the technical objectives for these two meta-configured structures and their desirability from an application point of view are also discussed in this chapter.

Next, in Chapter 2 experimental dynamic characterization of a passive-adaptive directional wave guide is presented. Preliminary discussions on the conceptual background for such devices are first presented. Based on these, design and testing of a structural-scale or macroscale prototype wave guide using a custom test rig is discussed. The results motivate the exploration of scalability to micro-scale manifestations with enhanced functionalities. Therefore, a directional wave guide with microscale features is designed for higher frequency bandwidths. This wave guide is fabricated and test. Discussion of results including correlation with some finite element simulations are presented to bring out the underlying mechanisms involved.

In Chapter 3, the second meta-configured structure, the passive-adaptive TVA is explored. The fundamental conceptual basis for implementing the passive-adaptive feature is discussed. A more detailed literature review pertaining to TVAs is presented. Firstly, a baseline (conventional) TVA is designed and tested using a custom rig. Next two basic variants of the passive-adaptive TVA are introduced. These are the base-attached and the tip-attached versions. Test articles for

both these cases are fabricated and tested. Both constant and varying mass configurations are investigated. Using a common metric, the bandwidth of isolation for the baseline and the passive-adaptive cases are compared and contrasted. The experimental observations are correlated with simulations for approximate (linear) versions to understand the mechanisms involved. Comparative performance analysis for the PATVA is also presented. Finally, a summary of main findings, the conclusions and implications drawn, and avenues and recommendation for future research are discussed in Chapter 4.

CHAPTER II

PASSIVE-ADAPTIVE DIRECTIONAL WAVE GUIDE

2.1 Introduction

Acoustic metamaterials have the innate ability to display unique wave manipulation characteristics through use of the local engineered features as sub-system within a host structural or material system. This ability has been penned through use of the word meta-configured structures, or in the Greek language μετά, which literally means "to go beyond". Construction of the term meta-configuration is used to incorporate the multi-functionality and ability to go beyond normal wave guiding techniques. The meta-configuration capabilities allows for an incorporation of a micro-scale through use of the subsystems rather than just the material itself.

The ability to direct waves is a technique dating to the early 1900's, of which the most prominent is optical wave guiding. The ability to direct light and utilize a "cloaking" technique is one that is highly sought after, this is made possible by studying the deep subwavelength natures [7] and understanding the band gap capabilities. By identifying and understanding the ranges of the band gap, the varying constituents of the configuration can be designed and manipulated to create the desired effects. Giving a flush idea as to one of the most crucial details within the research of acoustic metamaterials.

The concept is expanded to better realize the capabilities of assembling structures into a continuous material with unusual wave properties. The concept kept building until in 2006, Fang et al. [47] created an array of Helmholtz resonators, which when changing the volume of the cavity would lead to a change in the natural frequency. Other such concepts have been identified through use of a labyrinthine structure such as a spider's web [48], which make for ideal candidates for subwavelength sound control. These techniques allow the capabilities to activate or eliminate band gaps by increasing or decreasing the cavities.

A more recent configuration presented by Sheehan et al. [49] presents the concept of using nonlinear metamaterials with passive, amplitude-activated directional band gaps to perceive the concept of wave guiding. A baseline study of the system using a simple plate with a single type of mass loaded domes gave light to the formation of a band gap under excitation conditions. The study was made possible by utilizing the equipment and apparatus as shown within figure 2.1, the same equipment is used in the more complex configuration as well.

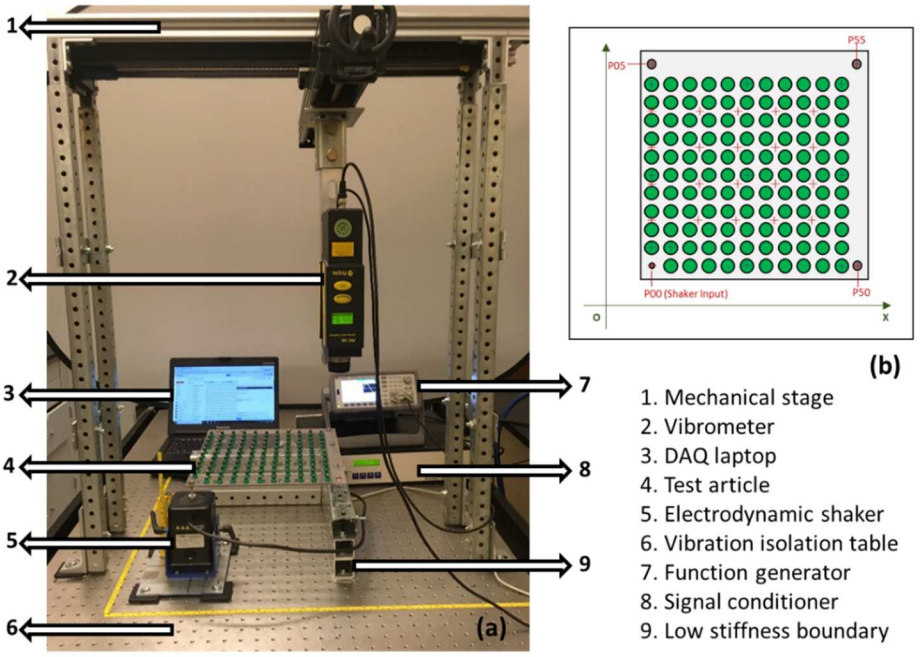

Figure 2.1: (a) Components of the experimental set-up and (b) schematic depiction of the wave rejection test article [49].

Upon investigation of the wave rejection test article shown in figure 2.1b a study of both the high and low amplitude cases the formation of a band gap is clearly seen. Taking a look into the low amplitude transmissibility plots given in figure 2.2 there is a clear representation of a band gap for the plate ranging from 130 to 225 Hz. Within the wave steering plate all of the resonators consist of the same properties so there will be an effect, as shown, where attenuation will occur within the band gap of the resonant structures. In the low amplitude band gap frequency range the data is normalized by utilizing the input displacement and finding the output in each corner of the plate, signified by D*.

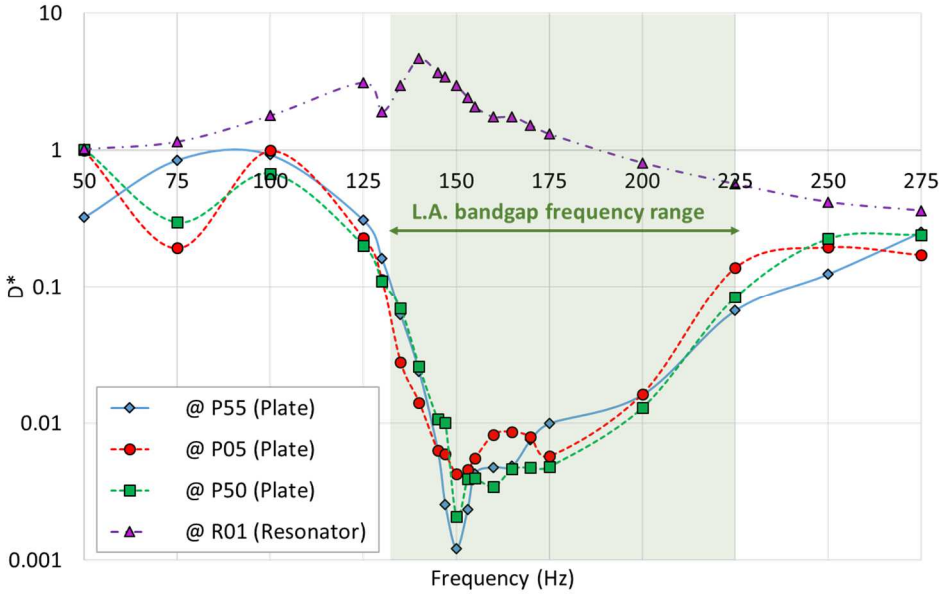

Figure 2.2: Displacement transmissibility versus excitation frequency at various monitoring locations on the wave rejection test article under low excitation amplitude conditions [49].

Figure 2.3 studies the high amplitude band gap ranging from 125 Hz to 225 Hz, which shows the same formation of the band gap as seen in the low amplitude cases. The high amplitude cases show that the band gap expands for the high amplitude case, but the D* values decrease. When analyzing the plate response, the same attenuating band gap is seen, however, not at the scale

of displacement that was previously seen. It is found that for both the high and low amplitude cases when engineered to be nonlinear and resonant dependent there is an ability to create a band gap that has both attenuating and propagating behaviors. When the frequency of interest falls within the resonators band gap it is attenuated and when the input frequency falls outside the band gap there should be propagation of that resonator.

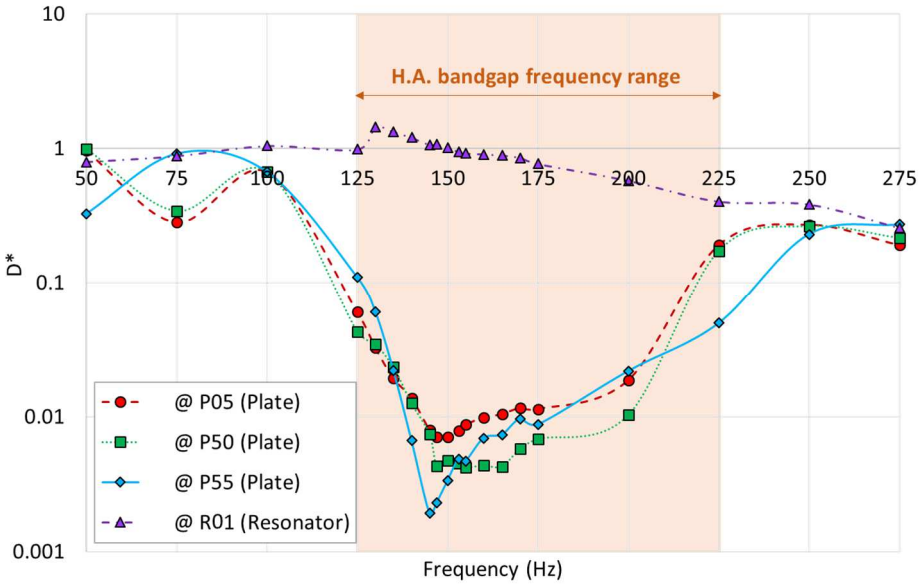

Figure 2.3: Displacement transmissibility versus excitation frequency at various monitoring locations on the wave rejection test article under high excitation amplitude conditions [49].

To expand on the ideas a new test article as shown in figure 2.4 is constructed by using periodic arrays of mass loaded domes laid on a polycarbonate substrate. So by incorporating a low stiffness boundary and inputting a mechanical displacement the band gap frequency ranges could be discovered. This configuration makes use of a linear symmetry with two different resonators in each direction and tested at the four corners.

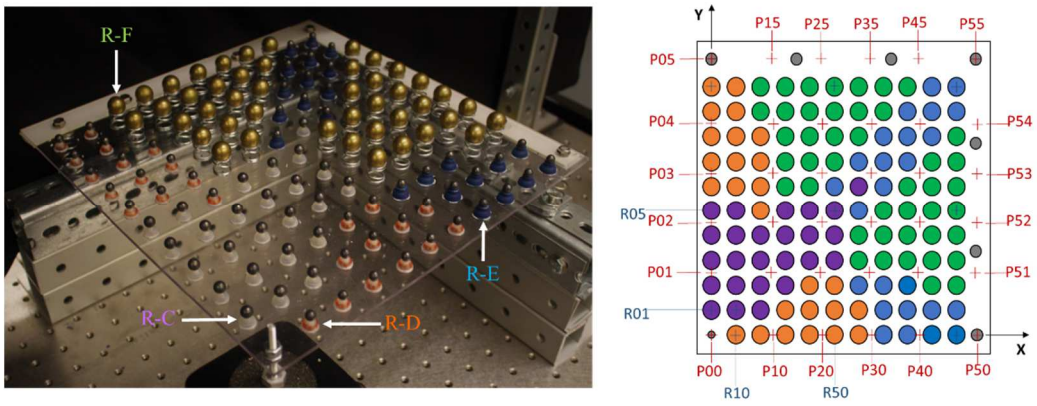

Figure 2.4: Photograph of the wave sorting test article (left) showing resonator types and its schematic depiction (right) showing monitoring locations [49].

Allowing an ability to tune the band gap by tailoring the periodic structures and arranging them in such a way that the frequencies shifted. An initial study of the low amplitude cases shown in figure 2.5, denotes the ability to produce propagation occurs when different input frequencies are observed while attenuating the other frequencies within that range. Showing the ability to focus or use a sense of selective beaming in order to manipulate waves when a low input amplitude is used.

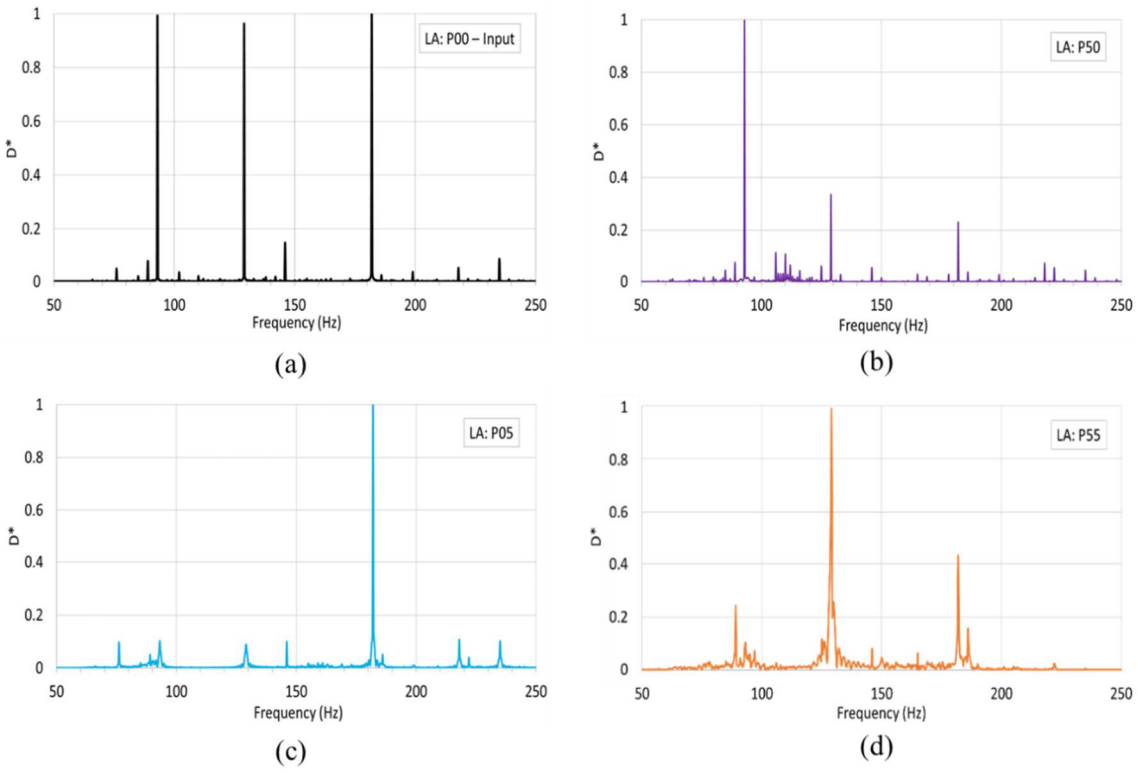

Figure 2.5: Normalized displacement transmissibility spectra for (a) the input monitored at location P00 and the outputs monitored at locations (b) P50, (c) P05 and (d) P55 for low amplitude input excitation [49].

The results of the low amplitude input excitation shows that specific frequency components are propagated along the pre-designed 'paths' depending on the resonator type that is missing along the path. This occurs because the band gap associated with the missing resonator is absent along a specific path and therefore a frequency component in the input corresponding to this band gap would propagate along this path. To better understand passive-adaptivity at higher amplitudes a second test using a larger input excitation was obtained shown in figure 2.6. At higher amplitudes, the nonlinear response of the resonators causing the band gap's lower bound to shift towards lower frequencies, thereby permitting lower frequency input components that previously propagated, to now be attenuated. This is evident for the tri-frequency input with slightly lower frequency components as shown in figure 2.6. These components are now attenuated along their designated

paths, although at the higher amplitudes the nonlinearities trigger additional frequency components to appear in some of the outputs, which is to be expected.

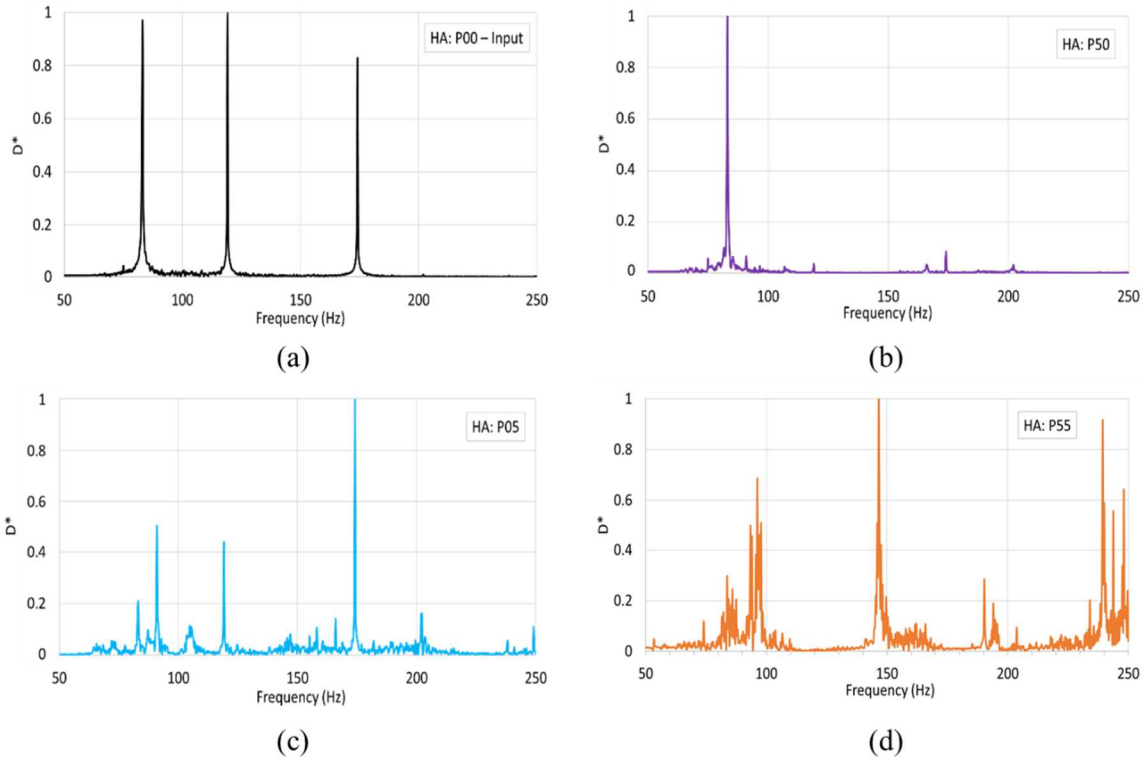

Figure 2.6: Normalized displacement transmissibility spectra for (a) the input monitored at location P00 and the outputs monitored at locations (b) P50, (c) P05 and (d) P55 for high amplitude input excitation [49].

It is this concept, which forms the basis for the directional wave beamer studied in this work, wherein this effect is reproduced for compact waveguide with integral resonators tuned for much higher frequency ranges. This leads to a micro-electromechanical system (MEMS) scale device whose resonator features range from a couple of millimeters to several micrometers. However, due to the complexity of designing a MEMS scale device without preliminary data, a structural scale test article was initially investigated to understand the mechanisms involved by incorporating the "meta-configured" design aspects sought into the MEMS scale test article.

After initial proof of concept is obtained using the structural scale test article the MEMS scale configuration is designed. This allows for the development of a compact waveguide to manipulate the passage of high frequency mechanical waves.

The conceptual schematic for the microscale directional wave beamer is shown in figure 2.7, it consists of five different types of integrally-fabricated cantilevered mass-type resonators. These resonators are designated R0 – R4. Figure 2.8 shows the relative band structure for the wave guide. R0 resonators, which are arrayed on the plate outside of the axial propagation paths forms the bulk of the resonators. These 'background' resonators create a band gap spanning the entire frequency range of interest precluding propagation in the regions where they are present. The other (axial) resonators (R1 – R4) have staggered band gaps as shown in figure 2.8. The colored contour lines depict the notional regions of propagation for frequency components that lie within the non-overlapping portions of band gap of the same color among the band gaps for R1 – R4. For instance, a frequency component at 17.5 kHz which falls within the band gap for the R3 (red) resonators but not within the band gap for any of other axial resonators (R1, R2 or R4), would propagate the '-y' axial path but not elsewhere. The input signal is applied at the center (origin) of the plate. This provides a means to selectively filter specific components of a signal along the predesignated axial paths. The arraying pattern on the waveguide plate could conceivably be tailored to suit specific applications.

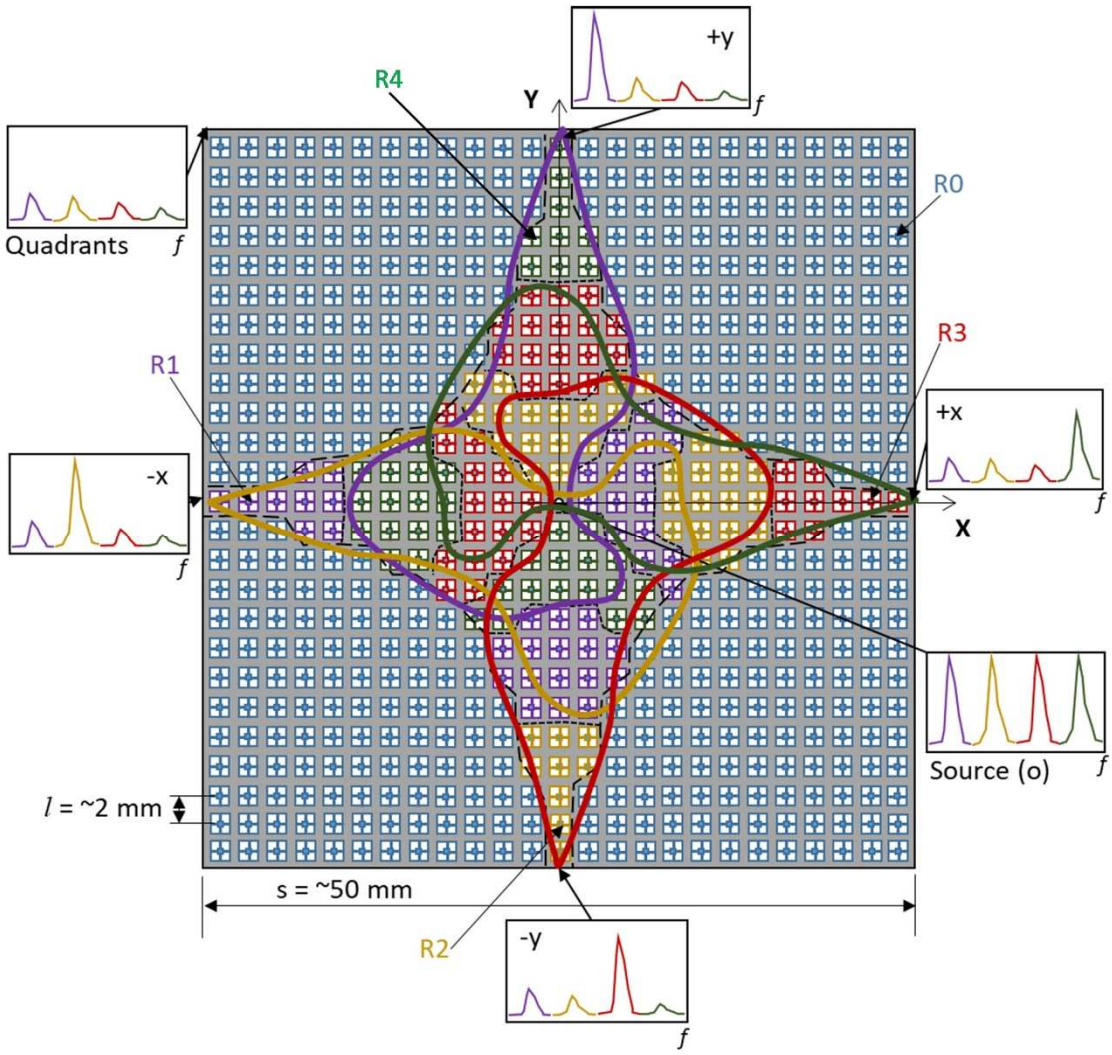

Figure 2.7: Band gap regions with spatial configuration of resonator units – the colored line contours correlate to the area where the resonator of the same color is missing.

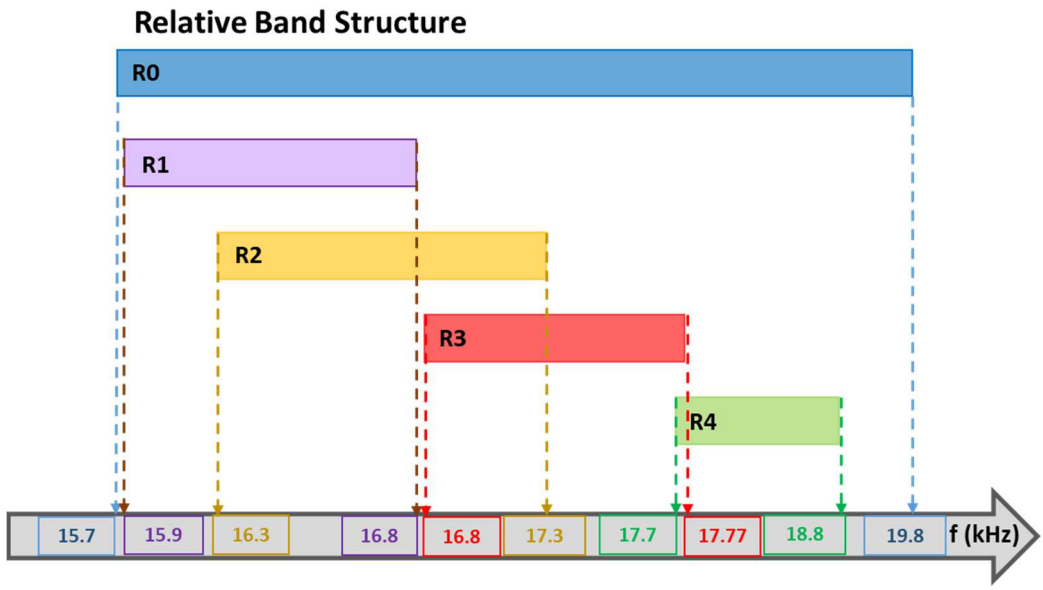

Figure 2.8: Relative band gap structures corresponding to the R0-R4 resonators of the passive-adaptive directional wave guide.

2.2 Materials and Methods

AMs exhibit the ability to direct a frequency by engineering the locally resonant features to have a specifically tuned value. Finding that the by incorporating a transverse wave into a plate with a free boundary and individual resonant features the manipulation of waves is available for techniques such as wave rejection, wave steering, and wave guiding. Expanding on the current work an experimental basis for wave guiding is presented through use of piezo actuation input at the center of the plate. The research introduces the wave guiding techniques and an understanding that the wave guiding techniques could be expanded to a wider array of directions if there is a feasible amount of varying resonators. Data is collected through using a laser vibrometer and output as a normalized displacement to understand if under a set frequency there is propagation outside the band gap and attenuation within the band gap. If the frequency of interest is within the resonators band gap then there will be attenuation and if it lies outside the band gap, there is

propagation. The work presented gives the techniques, findings, and limitations of the study on wave guiding.

2.2.1 Experimental Setup

The apparatus used to understand the wave guide included a 33500B series function generator, a PDV-100 laser vibrometer, a 482C series signal conditioner, piezo actuator, x-y stage, a 2100E21 power amplifier, and a National Instruments X series data acquisition (DAQ) system. Each piece of equipment is vital to the experimental dynamic characterization of the directional wave guide. The first of which is the function generator, the role of this item is to generate electrical waveforms over a wide range of frequencies. The waveform sought after in this case is that of a sine wave, the problem behind the generator used is that there is still noise within the system. In order to bypass the noise a LabVIEW program was created in order to vary the amount of samples and mitigate the noise levels by use of filters.

The LabVIEW program as shown in figure 2.9 was used in filtering the noise and obtaining the data sampled. The program created allowed the user to input the number of samples and the rate at which the systems response is tested. Both quantities are important as the sampling rate or the rate is used to determine the samples per second measured in Hertz (Hz). To avoid aliasing a sampling frequency that is 2.5 times the largest frequency of interest (50,000 sampling points) is used, satisfying the Nyquist Theorem. The data is then taken into the DAQ, processed as velocity data, and converted into displacement data using integration through Simpsons rule. After converting, the data into displacement data both the Fast Fourier transfer (FFT) spectrum of displacement and the displacement vs. time data can be collected and analyzed. The FFT is important, as it will help determine the levels of displacement at different frequency values.

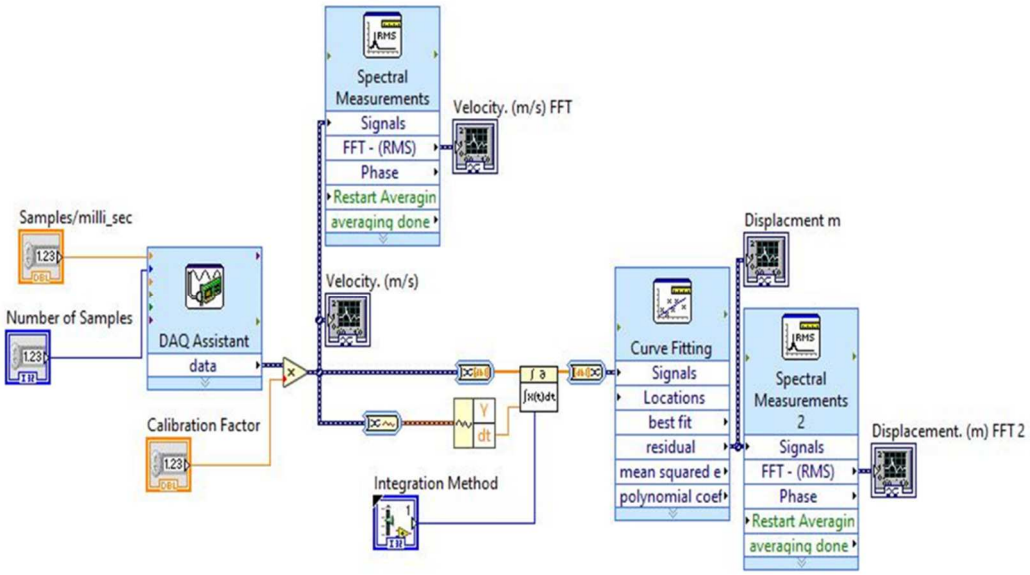

Figure 2.9: LabVIEW program for data analysis, illustrating the steps and integration process used to obtain the kinematic data.

The function generator is connected to the signal conditioner, whose use is to manipulate the analog signal and turn it into a digital signal to process. The processed data can be input into the DAQ, however, the signal needs to be first taken from the laser vibrometer. The laser vibrometer acts as an interferometer that measures the velocity at a reference point, and outputs the data into the DAQ and in turn connecting to the computer utilizing the LabVIEW program. In order to simulate displacement and vibrations a piezo actuator was used, the vibrations stimulated by the piezo could be picked up by the laser vibrometer. A piezo actuator is a type of ceramic, which expands and contracts upon generation of an electrical charge, in turn generating force and motion. This motion can cause the piezo to generate heat, the electric current also generates an amount of heat, in the experiment this became a problem since the frequencies of interest were so high. The high frequencies caused the heat generation to be greater than normal and in turn fried several piezo stacks. To mitigate this issue the testing was done in small intervals and the piezo stack was changed regularly. The piezo actuator is attached to an amplifier in order to increase the power of the signal. The equipment used is very similar to what is shown figure 2.1, however, the only difference that

is seen within the equipment is the modal shaker is no longer used. Instead of a modal shaker, a piezo actuator is used and a new testing set-up is configured.

In order to test the wave guide a testing apparatus was modeled and created to better understand the response of different points within the wave guide. The testing apparatus shown in figure 2.10 was configured by attaching four galvanized steel telescoping rods to both a top and bottom carbon steel plate with a thickness of half an inch. The testing apparatus was placed on an x-y stage to create the ability for precise movements when testing different points of interest. The next portion to the apparatus was creating a stand to house the piezo, so a single metal shaft was extruded on a central plate and attached to bolts so that the piezo's distance from the wave guide could be manipulated to create an artificial preload. At the center of the wave guide a piezo actuator was placed to simulate the dynamic response to the system. This allowed for the actuation to act at the center of the plate and the surrounding structures to be unaffected by the dynamic excitations.

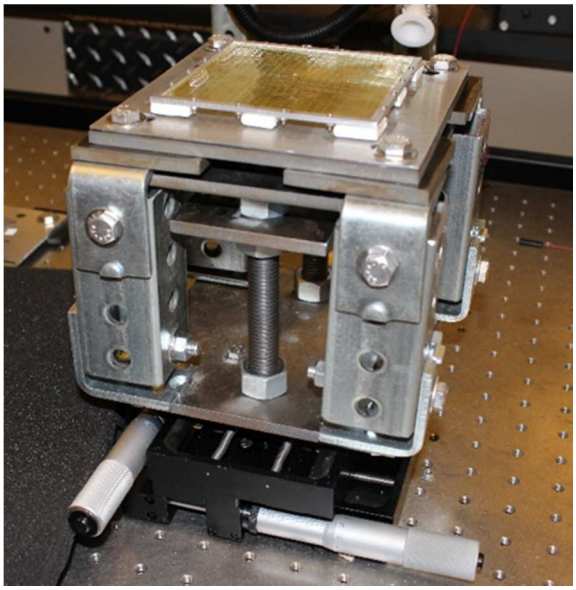

Figure 2.10: Passive-adaptive directional wave guide testing apparatus shown with test article mounted.

The final key aspect of the apparatus was to create a boundary, which would not be fully fixed when the system had an input vibration. If the boundary was fully fixed the wave simulated by the vibrations would reflect back and cause the response to be tainted, instead a more free end would need to be simulated. Since a free end is difficult to create on an article such as this, an elastic boundary shown in figure 2.11 was created using foam. Both a foam boundary and a spring boundary was tested to better understand the response of the boundary. The use of springs proved to be the more difficult task since the area of application was only 2 mm and attaching the springs to the boundary was more challenging than expected. The foam boundary was introduced and tested for the stiffness, the foam boundary proved to be more efficient in the sense that the foam was simpler to attach and the foams lengths could be manipulated to be the same length and the spacing between the foams could be measured and kept consistent throughout the boundary. It can also be noted that in order to accurately test and measure the wave guide's responses, a nominal tension would need to be applied, so before attaching the foam pieces to the boundary the wave guide was stretched in order to give it a sense of uniform tension across the plate.

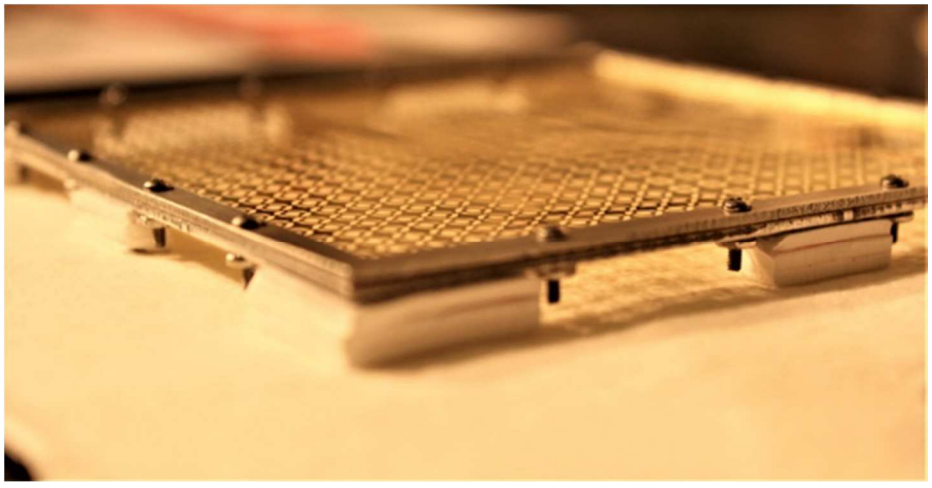

Figure 2.11: Wave guide test article mounted on foam boundary.

2.2.2 Resonator Design

The effect that was sought after within the wave guide was on the idea that frequencies could be manipulated by creating a series of resonators whose band gap covers a variety of frequencies. In this case, there will be five separate resonators; each resonator except the initial R0 resonator has a band gap range of around 1000 Hz. The difference between the initial R0 resonator and the resonators labeled R1-R4 is that the R0 resonator will cover the whole range of frequencies of the R1-R4 resonators. In theory if there is a patch of resonators there will also be a band gap range covering the resonators within this patch. Within a patch, there is at least one of the four resonators missing, so there will also be four different distinct series of resonators each with their own distinct frequency range.

In order to accomplish the sought-after phenomena both the resonators and the plate itself would need to be designed, the first of which is the resonators. As previously mentioned, there will need to be five different resonators, one resonator that will cover the whole band gap and four resonators that will cover the frequencies within the range of the single resonator. In order to accomplish the phenomenon the masses of each resonator would need to be manipulated; this could be accomplished by creating two different masses, an inner mass and an outer mass. The inner mass would have cantilever arms that would also have varying lengths, in turn changing the band gap of the resonator. The frequency of the cantilever arms could be calculated by

$$f_n = \sqrt{\frac{3EI}{m_{eqv}L^3}} \tag{2.1}$$

Where E is the Young's modulus, I is the area moment of inertia, L is the total length of the cantilever arms and as per [50], the equivalent mass (m_{eqv}) is found by

$$m_{eqv} = 0.23m_{beam} + m_{tip} \tag{2.2}$$

The resonator R0 that covers the total band gap of the remaining resonators was initially designed first since it would cover the total band gap of the resonators. To create the desired symmetry within the plate there would need to be uniform resonator dimensions, so the outer structure was determined to be 2 x 2 x 0.2 mm. However, after investigating the frequencies it was found that using a smaller thickness of 0.0508 mm and dimensions of 4 x 4 mm would better suit the needs of the wave guide, giving finalized dimensions of 4 x 4 x 0.0508 mm. It was decided to create a larger outer mass with an inner circular dimension of 3.6 mm; however, a secondary mass would need to be created in order to create the desired effects of covering the larger band gap. To make the second mass a smaller circle was created with the dimensions of 2.5 mm with an inner diameter of 1.5 mm. The last portion of the R0 design is the cantilever arms, the lengths of the arms would be the difference in circular diameters giving arms of 0.55 mm and arm diameters of 0.4 mm were used to give the desired effects. The finalized resonator labeled as R0 is shown in figure 2.12; the mass of the article could be calculated by finding the masses of the cantilever arms, the outer structure, and the inner structure multiplying by the volume of the structures. This gave the R0 resonator a total mass of 4.28 mg, when the material being used is brass.

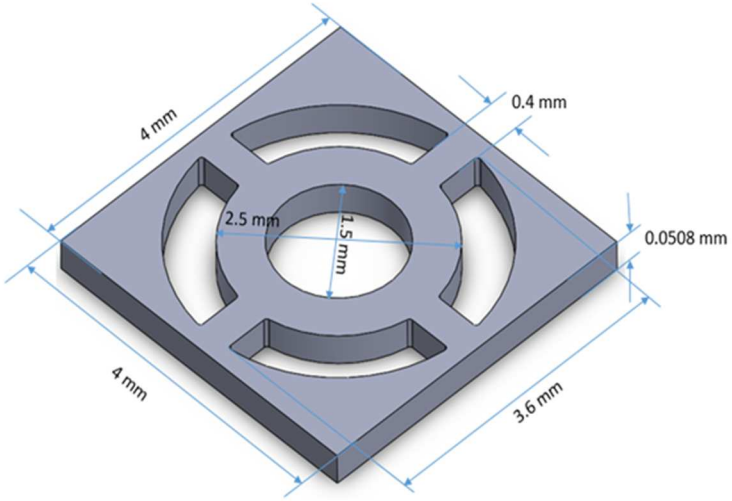

Figure 2.12: CAD model of the R0 resonator unit with dimensions.

Assuming that the dimensions of 4 x 4 x 0.0508 mm and the material of brass remained constant the remaining resonators would only vary in the larger outer circle, arm lengths, arm widths, and the inner circle diameter. The smaller inner circle would also remain as a complete structure in order to create a larger inner mass. By varying each structure to be different it would give a different mass variation which would also affect the frequencies when calculated.

The second unit that has the lowest frequency range of the R1-R4 resonators, effectively labeled R1 since its natural frequency was the lowest of the four resonators. As mentioned the smaller inner circle would remain a single structure so in order to keep the frequency range as low as possible the central mass needs to be smaller, an initial start of 1 mm was used. Also giving the outer structure a larger area with a diameter of 3.2 mm would allow for a smaller inner mass and so this left the arm length's to each be 1.1 mm each. The only remaining feature that could be manipulated was that of the arm thickness and in order to maintain a smaller mass the arm thickness was kept to a minimum of 0.32 mm. By changing each of these features it allows the moment of inertia to be changed and the mass to be increased or decreased in order to determine a different frequency. The finalized design as shown in figure 2.13 resulted in a smaller mass of 4.41 mg and at the same time giving a smaller frequency.

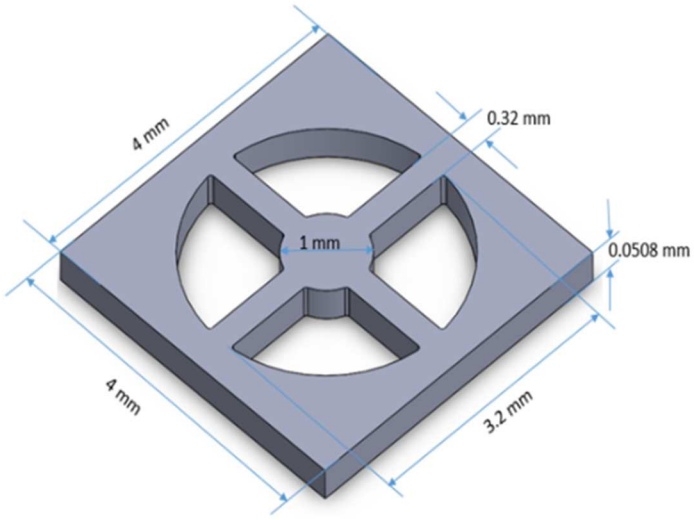

Figure 2.13: CAD model of the R1 resonator unit with dimensions.

The next resonator designed was the R2 resonator, to start out the outer structure was kept at 3.2 mm and the smaller inner structure remained at 1 mm. Since the outer and the inner diameter didn't change the length of the arms would remain the same and the only remaining structure that would allow any change would be that of the arm width. To increase the mass the arm width would also need to be enlarged and so a diameter of 0.4 mm was used. The change in diameter resulted in a mass of 4.56 mg with the structure's finalized result is shown in figure 2.14.

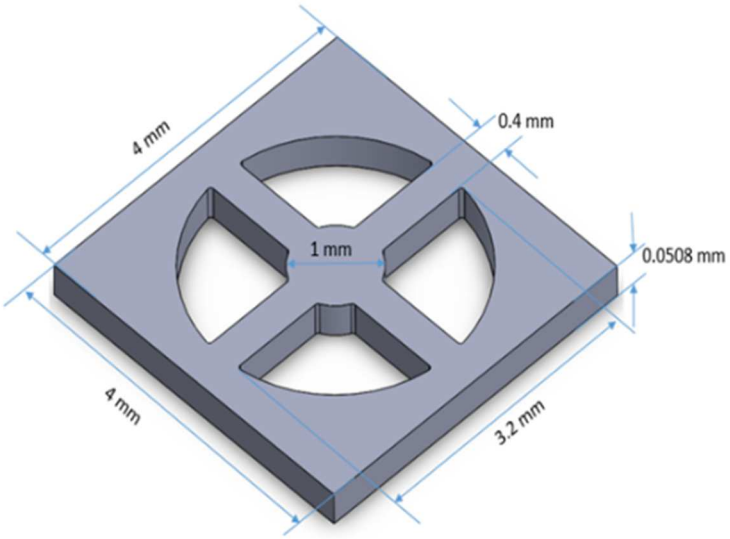

Figure 2.14: CAD model of the R2 resonator unit with dimensions.

The third resonator or the R3 resonator was designed with a smaller outer structure of 3.12 mm and a smaller inner structure of 0.9 mm diameter. By decreasing the outer and inner structures and increasing the arm lengths and diameters it can be noted that the volume can be increased since there are four cantilever arms meaning there is more volume within the cantilevers instead of the inner and outer structures. For the R3 resonator shown in figure 2.15 the arm width was kept constant with the R2 resonator at 0.4 mm and the length of the cantilever arms were changed to 1.11 mm. The change in the cantilever arms resulted in a mass of the R3 resonator being 4.68 mg.

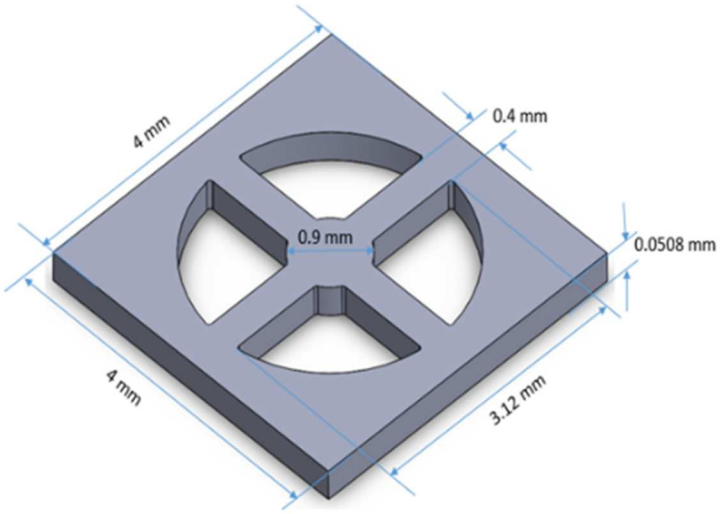

Figure 2.15: CAD model of the R3 resonator unit with dimensions.

The fourth and final resonator labeled the R4 resonator, which had the largest frequency, decreased both the inner and outer structures diameters to be 1.12 mm and 3 mm respectively. This gave the length of the cantilever arms to be 0.94 mm with a cantilever arm length of 0.48 mm. Even though the arm lengths may be smaller the increase in the width well enough makes up for it giving a larger mass of 5.09 mg. The R4 resonator with its finalized dimensions are shown in figure 2.16.

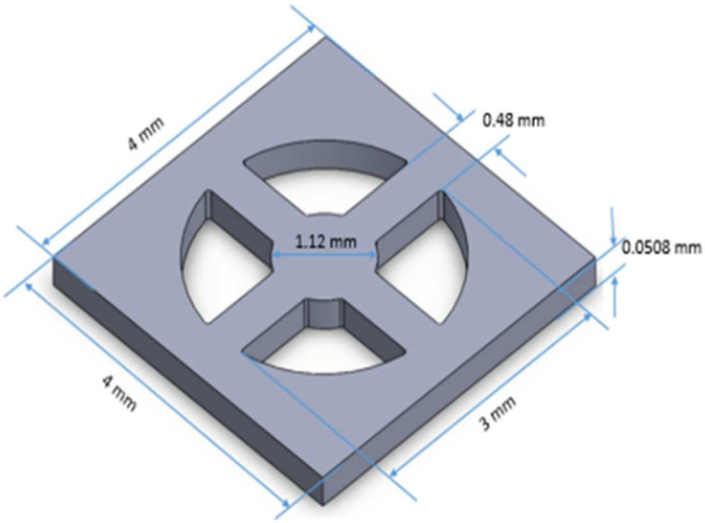

Figure 2.16: CAD model of the R4 resonator unit with dimensions.

In order to get a clearer picture of the varying differences with each of the resonator units table 2.1 was configured with the CAD modeled unit cell dimensions; it can be shown that no two resonators are alike completely. Each Resonator varies in way such that they should each have a different natural frequency when simulated. Upon designing the resonators in this way there should be enough evidence concluding if there is attenuation within the resonators band gaps.

Feature (Units)	***Resonator***				
	R0	**R1**	**R2**	**R3**	**R4**
	Dimensions				
Outer structure (mm)	4.00	4.00	4.00	4.00	4.00
Outer circle (mm)	3.60	3.20	3.20	3.12	3.00
Arm width (mm)	0.40	0.32	0.40	0.40	0.48
Arm length (mm)	0.55	1.10	1.10	1.11	0.94
Inner circle (mm)	2.50	1.00	1.00	0.90	1.12
Inner cavity (mm)	1.50	0.00	0.00	0.00	0.00
Height (mm)	0.0508	0.0508	0.0508	0.0508	0.0508

Table 2.1: Geometric details of built-in resonators in the passive-adaptive wave guide

After creating the resonators, the upper and lower frequencies would need to be obtained to effectively make sure that the design of the R0 resonator and its band gap effectively covers the band gaps of the four remaining resonators. The band gap range is found by

$$\omega_u = \omega_L \sqrt{1 + \frac{m_2}{m_1}} \tag{2.3}$$

The band gaps can be found by finding the boundary mass or the non-resonating mass, which is labeled m_1; this refers to the mass ranging from the outer 4 x 4 mm structure and the diameter of the outer circle structure. The inner resonating mass labeled as m_2, found by using equation 2.2 and m_{eqv}, also would need to be found, the resonating mass consists of the cantilever arms and the inner surface. The lower band gap frequency is labeled as ω_L with the upper band gap labeled as ω_u can be used to find the different band gap ranges of the R0-R4 resonator units.

2.2.3 Wave Guide Design

The wave guide itself was initially designed such that there would be 625 different resonators within the confines of a 50 x 50 mm plate; this gives 25 resonators in each row and 25 resonators in each column. A border of 2 mm on each side would be placed around the edge to give room for the foam boundary; this gave total dimensions of 54 x 54 mm for the outer boundary.

The design of the system was originated by trying to create an arrangement of resonators such that each cardinal direction will only experience a patch of resonators once, where a patch can be a series of 3, 4, or 5 resonators depending on the row and column location. Upon complete configuration of the resonators there should only be, at any time, a section of three different patches of resonators. It was also assumed that in the directions where there was not a main cardinal direction there would be a series of R0 units, mainly in instances such as the ordinal directions. Having the configuration to be such as this would allow for the attenuation of frequencies when it passes through the R0 band gap.

In total, there would be 12 different patches of the R1-R4 resonators and there would be 4 patches of the R0 resonators. Each patch of the R1-R4 resonators would have a configuration of 16 resonators of the same type, these resonators would be configured in such a way that the R0 units would be symmetric about the x and y axis. In each cardinal direction the layout would start with 3 resonators of the first type, suppose for this case the first resonator is R1. The next type of resonator in this direction would be the R2 resonator, however, the amount of units along the y-axis would be decreased so the amount in the x-axis would be increased to house 4 resonator units. There would be a third resonator type added with a length of 5 units in the x-axis and a smaller amount in the y-axis. In the ordinal directions, there will only be a patch of a resonator within the R1-R4 spectrum and also a patch of the R0 units in each of the secondary directions. The complete configuration of the design is shown in figure 2.17, noting the symmetry along the x and y

directions. The symmetry along the x and y directions allows for each of the different directions to have the ability to respond with the same effect. The different colors within the figure designate the different R0 to R4 resonators. Within the figure the color of the R0 resonator is that of the blue color, R1 is brown, R2 is yellow, R3 is red, and R4 is green. It can be noted that in any direction there are three resonators (not considering R0 resonator), and the fourth resonators frequency range should be propagated in the direction it is missing.

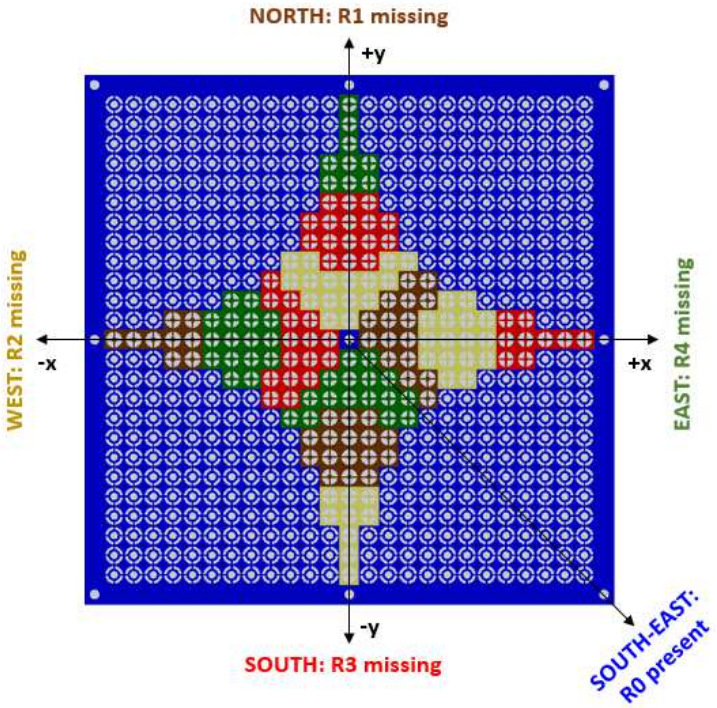

Figure 2.17: Resonator plate configuration illustrating the directional nomenclature and the resonator type missing along each axial direction.

The wave guide was designed to be made of resonators with dimensions of 2 x 2 x 0.2 mm, with 25 x 25 resonators giving dimensions of 50 x 50 x 0.2 mm. There were also 2 mm added to each side of the plate in order to create a uniform boundary for mounting purposes. In total, there would be 625 resonator units within the plate, giving an ample range of test positions that could be analyzed during the testing process. At the center of the plate a unique resonator with just an outer

mass and no central mass was added, this missing resonator unit is where the excitation of the system will take place.

The last aspect of this design was to successfully figure out the plate manufacturing. There were several ways that this could come about, whether it be 3D-printing, waterjet, silicon etching, or the use of metal etching. The initial article was attempted to be manufactured by utilizing the use of silicon etching, this process is very time consuming as there are many detailed steps within the process. The first of which is finding someone to manufacture the article with low scale quantity, after finding a manufacturer a DRIE mask or a deep reactive-ion etching mask needs to be made. A deep reactive-ion etching mask is an anisotropic etch process in which trenches are made in wafers, in this case silicon wafers. The DRIE-mask was created as seen in figure 2.18; however, this process took longer than originally expected so different processes were analyzed.

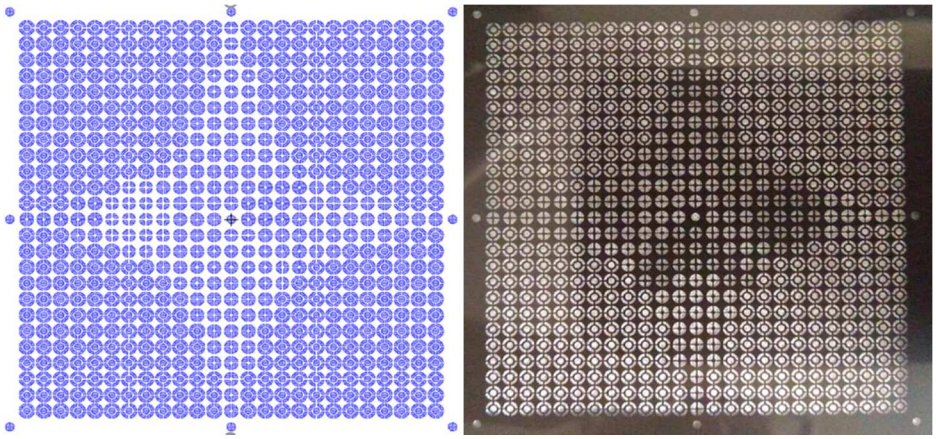

Figure 2.18: DRIE-mask created to manufacture a micro-scale wave guide test article using a silicon wafer.

The next process looked into was that of 3D printing, the capabilities could be done; however, the quality of the work would vary due to the resolution of the printer. The complexity of the wave guide were great and so the dimensions of the wave guide needed to be increased, mainly the side or the height dimensions. The height of the article was moved from 0.2 mm to 2 mm, and

an article of 54 x 54 x 2 mm was manufactured and a larger article, which was two times the original length and width, was manufactured. Upon initial glance the article looked to be a good print, however, upon looking under a microscope as shown in figure 2.19 it showed that the article was manufactured in such a way that the sidewalls had merged together in some places. This was due to the small void areas within the resonator designs. There were also complications with the interaction between the piezo and the 3D printed article, upon excitation of the system the heat resonating from the piezo melted the article. After witnessing this phenomenon, a layer of mica ceramic was used to create a heat resistant barrier between the piezo and future articles. The next process that was looked into was that of waterjet, however, due to the complexities of the system the process would not work.

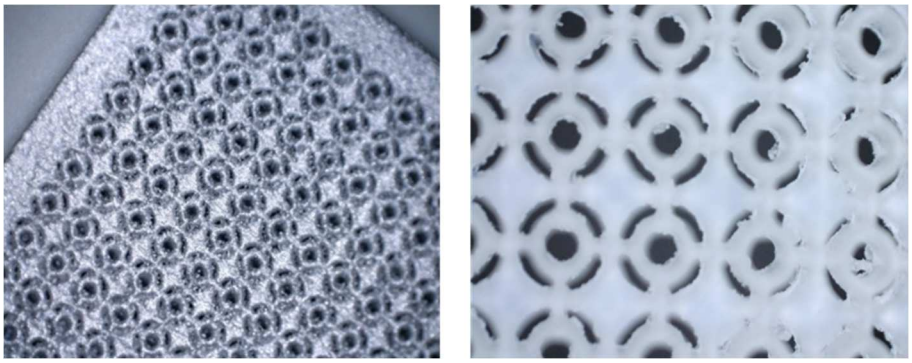

Figure 2.19: Images of 3-D printed test articles: Left – metal version, Right – polymer version. Both versions give an idea as to the lack of adequate precision in the resonator features required.

The last process and eventually the process that was sought after was that of metal etching, which was doable, however, the side lengths could be manipulated to better suit the needs of the experiment. This worked great in the circumstances since the original frequencies of interest were so high, instead by manipulating the dimensions of the plate the frequencies of interest could be reduced and made into a more reasonable testing range. The new dimensions of the plate were manipulated to be 108 x 108 x 0.0508 mm, this gave a boundary of 4 mm on each side, however the number of resonators within the plate remained the same. The only differences is that the

resonators now had dimensions of 4 x 4 mm and the height of the article was reduced to 0.0508 mm.

The only remaining issue was to decide which material to create the wave guide from, different material properties were analyzed and the frequencies were calculated to determine which would be the best fit and give the best frequency range. Materials of Brass, Aluminum, Steel, and copper were all looked into and it was found that even though the difference between brass and copper were miniscule, the use of brass was determined to go ahead and use for the wave guide. The finalized design is shown in figure 2.20, there is also a nickel shown in the picture in order to obtain a good concept of the size of the wave guide can be obtained.

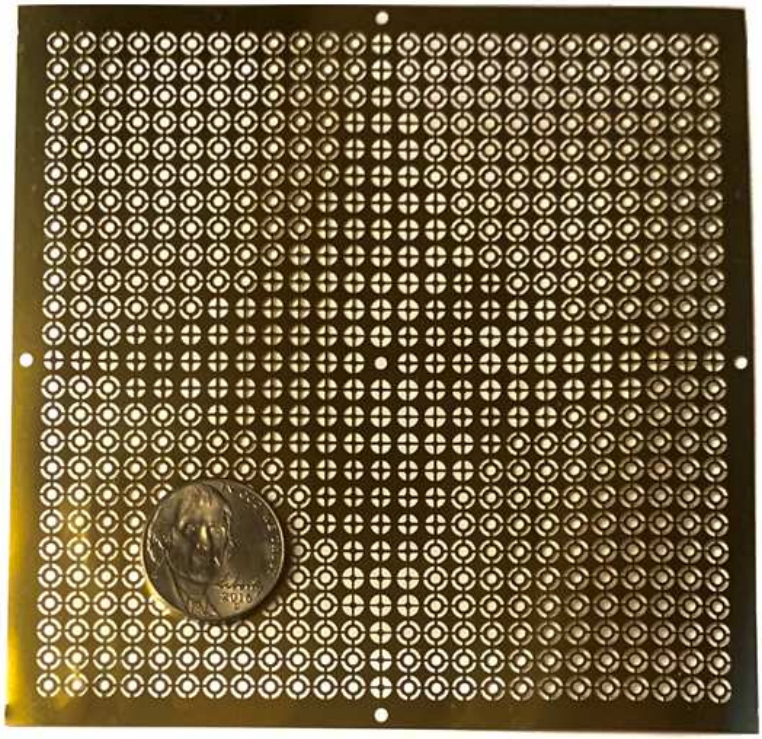

Figure 2.20: Manufactured passive-adaptive directional wave guide test article.

2.2.4 Test Cases

The tests could be categorized into two different configurations, one which the resonators act as single units (i.e. in order understand the response of individual resonators) and one where the resonators act as part of the waveguide plate (i.e. in order to understand the overall wave manipulation behavior.) Each of these categories could be summed up with their own respective tests summarizing different aspects of the wave guide's capabilities. The tests could therefore be split into the resonator and the wave guide tests. The resonators are characterized individually followed by the wave guide, which would be characterized for directional wave propagation.

Each resonator will have a corresponding band gap with equation 2.3 determining the upper limit of the band gap. The lower bound of the band gap is the natural frequency of the resonator. This band gap can be used to determine the range of frequencies that can be used to tailor the directional wave propagation. The lower limit of the resonators band gap would indicate a start point and the upper limit gives the frequency range of attenuation corresponding to each resonator. The band gap of the R0 unit is designed to cover the complete frequency range of interest while the band gaps for R1-R4 resonators are designed to cover smaller frequency bandwidths within the overall range covered by R0.

In order to ensure that the global modes of the waveguide do not overlap with the frequency range of interest corresponding to the local resonator band gaps, modal analysis was done for the waveguide using FEM. The boundary condition when the waveguide is installed in the test fixture is different for the full plate than what it is for the single resonators. The wave guide is mounted on a 'low-stiffness' boundary as shown in Figure 2.10. For the plate the boundary condition is no longer a fixed edge, instead the boundary is now a compliant boundary fashioned from foam strips. The boundary consisted of "N" number of foam spring elements with an averaged stiffness of 54

N/m put in series around the edge of the wave guide. In this case, the total number of foam articles comes out to be ten (N=10).

The second simulation that was run on the wave guide is that of the dynamic implicit analysis, this test is one which analyzes the transient response of the plate under different input excitations. The excitation was provided in the center of the plate on the inner edge of the central resonator unit. To simulate the excitation correctly, a harmonic amplitude applied in the U3 or z-direction is created by specifying a circular frequency through use of equation 2.4.

$$\omega = 2\pi f_n \tag{2.4}$$

The type of wave being simulated would also need to be specified, either a sine wave or a cosine wave. This is done by use of equation 2.5. A sine wave can be simulated by setting A=0 and B=1 or a cosine wave can be configured by setting B=0 and A=1. In the wave guide's case, a sine wave is created.

$$a = a_0 + \sum_{n=1}^{N} \left(A_n \cos\left(n\omega(t - t_0)\right) + B_n \sin\left(n\omega(t - t_0)\right)\right) \tag{2.5}$$

Where a_0 corresponds to the initial term of the Fourier series or the average value $f(t)$, A_n correlates to the odd terms in the Fourier coefficients and B_n corresponds to the even terms where n is the n^{th} term (n=1,2,3,…). The term ω refers to the fundamental frequency, t_0 is the initial time, and t is the time at which the integral is tested.

The plate's response could be simulated using different frequencies that lie within each of the band gaps corresponding to the resonators. Once all checks were completed, several 'pick-up' nodes were chosen to act as references to monitor the response. One node would be chosen in each of the cardinal directions. Further, one node along one of the diagonal directions is chosen to view how the wave behaves within the region of background resonators (R0).

The experimental testing consisted of first ascertaining the natural frequencies of the resonators and interrogating the wave guide for directional propagation and attenuation. The theoretical band structure of the wave guide have been determined from simulations, however, the experiments help verify how well the response of the test article matches the modeling.

Simulation or test	***Resonator frequency range***					
	R0	**R1**	**R2**	**R3**	**R4**	**Wave guide**
Natural frequency (Hz, Abaqus)	15739	15938	16321	16883	17702	94.1
Transient simulation (Abaqus)	16-19 kHz (1000 Hz increments)					
Steady state testing	15-20 kHz (500 Hz increments)					

Table 2.2: Wave guide and built-in resonator simulation and experimental test cases

2.2.5 Simulation Modeling

Numerical simulations using Abaqus were conducted to ascertain the performance of the resonators and the waveguide. The resonators were sketched in SolidWorks and a model of the sketch could be imported into Abaqus through as a 3-D planar shell. After importing the sketch, the material properties were specified. The wave guide was manufactured of brass and so parameters of E, ρ, and ν, were specified or Young's modulus (112.5×10^9 Pa), density (8553 kg/m^3), and Poison's ratio (0.357) respectively. Since the resonators are integrally built into the wave guide, these properties are the same for the resonators as well as the rest of the wave guide. The size of the mesh was tested and analyzed to find the value at which the natural frequency converges to within a 5% difference between successive values. Finding the 5% convergence differential will give a clear idea as to where the change in mesh size will no longer significantly influence the results of the natural frequency. A mesh size of 4×10^{-5} was used to have at least 10 elements within the central resonator units and to satisfy the 5% convergence constraint. A set of convergence simulations were ran and table 2.3 shows that at a larger mesh sizes, better convergence would be achieved, however, the smaller mesh size of 4×10^{-5} was chosen since it gave sufficient accuracy with better computational efficiency.

Mesh convergence study			
Mesh size (mm)	**Number of elements**	**Frequency (Hz)**	**% Difference**
0.0008	28306	103.01	0.029
0.0006	29306	102.96	0.049
0.0004	38612	100.69	0.641
0.0002	98443	97.42	1.560
0.0001	439819	94.09	3.420
0.00008	649407	93.81	0.297

Table 2.3: FEM mesh convergence study for the passive-adaptive wave guide's simulation model

An initial look into the convergence it is seen that at 0.0008 mm and 0.0006 mm the two frequency values are close in value, however, extending the mesh size to 0.0004 mm the frequency value decreases. To understand what is happening the mesh size was decreased even further until it once again converged to a smaller value. It was found that even though the mesh had converged it was not the correct natural frequency; this was primarily due to the complexity of the wave guide. A further convergence study was done to ensure convergence was obtained, noting that at a smaller mesh size the frequency converged at 93.8 Hz.

2.3 Discussion of Results

Presented in this section, is a summary discussion of the results for the numerical and experimental test cases.

2.3.1 Boundary Analysis

As previously mentioned, in order to effectively measured the desired effects from the wave guide, its edge boundary conditions have to be engineered to be sufficiently compliant so as to allow the output response signals to be picked up but at the same time providing sufficient support to the wave guide. The boundary is also designed so that the dominant global modes of the wave guide are sufficiently detuned so as not to overlap with the frequency range of interest that is being interrogated. However, these are not the only reasons behind the idea of having a boundary; the boundary will be raised giving the ability to access the piezo and control its interaction with the

wave guide. Knowing the distance between the piezo and wave guide will help to make sure that the article is centered and the piezo is also in enough tension. Therefore, a raised, low stiffness boundary fixture is developed to mount the wave guide.

After evaluating the type of boundary to be used, whether foam or spring, in this case a foam boundary was chosen for its ability to provide better dynamic stability. The foam material was tested under compression by using a Vernier Load Frame. The Load Frame allows one to measure an input displacement with a resolution of 0.1 mm versus a force load cell measuring up to 50 N.

Through the testing of the foam boundary, there were two things that needed to be ascertained; a) would the foam boundary revert to its original shape after being loaded and retain its stiffness over several cycles, and b) would the stiffness of the foam boundary be sufficient to detune the global modes of the waveguide while providing adequate vertical support. To check the first aspect, the compression test was repeated three times successively on a sample and the sample thickness is measured before the test began, after each test, and measured again after 2 minutes in order to see if the thickness reverted to its original thickness. Noting from the table that the foam was able to retain its thickness even after several tests were ran.

To check the second aspect, the foams stiffness response was recorded over three loading cycles. These tests were conducted by recording the incremental force it took to compress the foam by 0.2 mm. The slope of the force-displacement curve is extracted to determine the stiffness. While the dynamic stiffness of the foam can be significantly different (higher), estimating the natural frequency of the mounted test article using the static stiffness of the foam boundary provides a preliminary estimate about if it delivers a feasible solution. The natural frequency of the mounted test article is found by

$$f_n = \frac{1}{2\pi}\sqrt{\frac{kN}{m}} \tag{2.6}$$

Where *k* is the stiffness of the foam, N is the number of foam segments put in parallel, and the total stiffness is found by k times N. Shown in table 2.4 below, the averaged stiffness found between several cases, where the low and high frequency values of the foam boundary was obtained giving a stiffness of around 54 N/m and a frequency value of around 254 Hz. Since the frequency of the boundary is much lower than that of the wave guide so the global modes of the two will not interact allowing for more accurate measurements to be made and the ability to have a non-fixed boundary.

Foam boundary stiffness investigation						
Parameter	**k (N/m)**	**m (g)**	**N**	**Frequency (Hz)**	**Stiffness (N/m)**	**Remarks**
Test 1	14.19	0.021	41	261	56.76	
Test 2	7.10	0.021	41	185	28.38	Low stiffness
Test 3	18.92	0.021	41	302	75.67	High stiffness
Averaged	13.40	0.021	41	254	53.60	Average stiffness

Table 2.4: Summary of foam boundary stiffness checks

2.3.2 Transient Finite Element Analyses

Through finite element modeling (FEM) using Abaqus, the natural frequency values of the resonators were predicted. These frequencies could be used to understand the response of the wave guide under a steady state analysis. Simulating the plate under a steady state analysis allows the vibrations to be spread throughout the plate at a constant rate and be able to understand if the frequencies can be directed under different excitation frequencies.

The first case, where the natural frequencies were simulated, could be obtained through using a modal response and simulating the first 5-10 modes of the resonator. The first mode is known as the natural frequency. this is the mode that can be excited with the greatest amplitude at

resonance. The primary band gap's lower bound is defined by the natural frequency of the resonator.

Before running each simulation, an overall check is done making sure that the mesh, boundary conditions, material properties, and dimensional properties aligned up to the design and the parameters for the resonators. The first mode shape and the frequency from the simulation are recorded. As shown in figure 2.21, the response of the R0 unit lines up with the theoretical first mode shape of a plate. The FEM first mode frequency was obtained to be 15739 Hz.

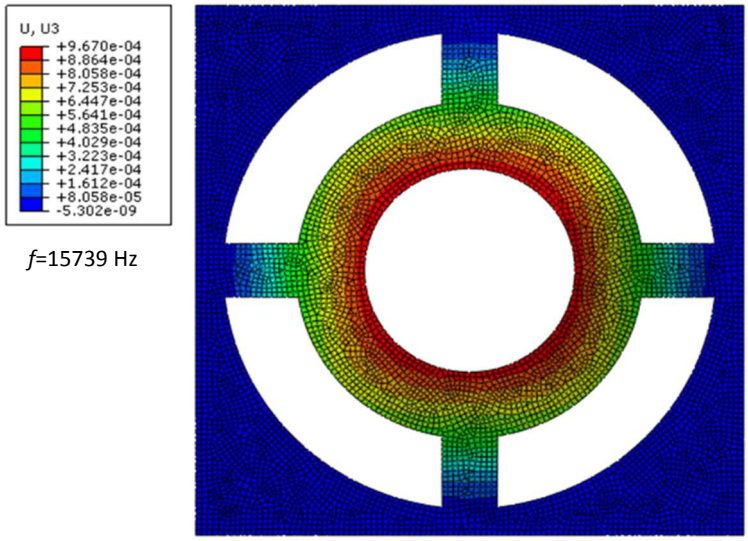

Figure 2.21: First mode shape of R0 resonator at 15739 Hz

The next resonator is that of the R1 resonator, the same edge fixity that is used for the R0 resonator is also used and the mesh is configured in the same manner. However, due to the different dimensions and design the resonator's natural frequency comes out to be 15938 Hz. The resonator's mode shape is shown in figure 2.22.

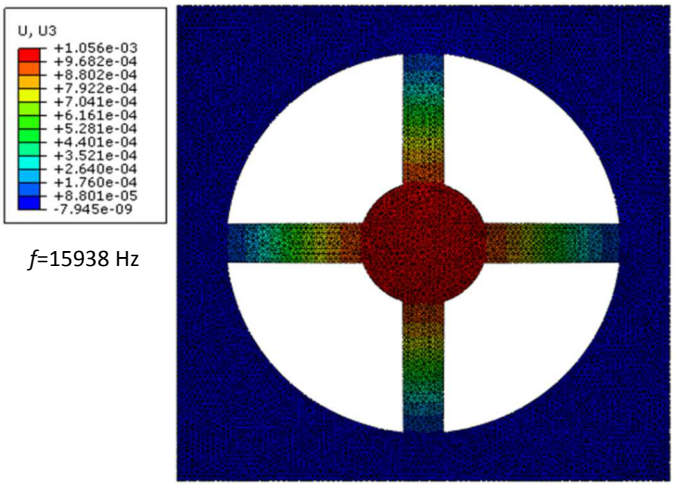

Figure 2.22: First mode shape of R1 resonator at 15938 Hz

The remaining resonators (R2-R4) are also simulated at the previously found converged mesh size to determine their natural frequencies. The parameter of the arm length varies as shown previously in table 2.1, however, the fixity and the mesh sizes are kept constant. The frequencies of each resonator is simulated to be 16321 Hz, 16883 Hz, and 17702 Hz respectively. The first modes of each of the different resonators are shown in figures 2.23-2.25 respectively.

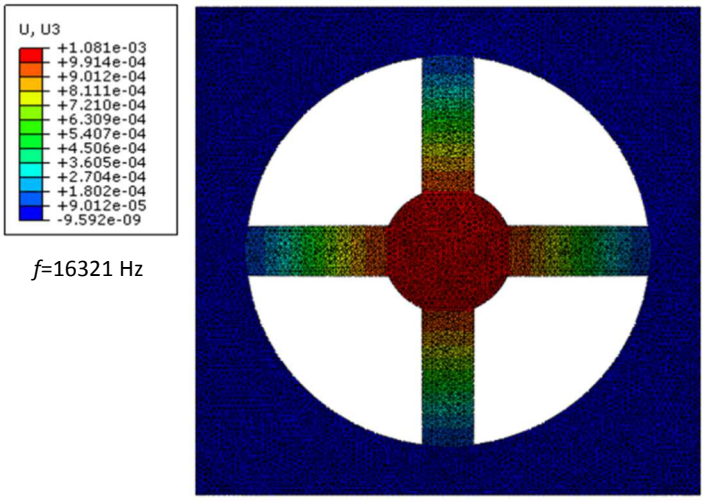

Figure 2.23: First mode shape of R2 resonator at 16321 Hz

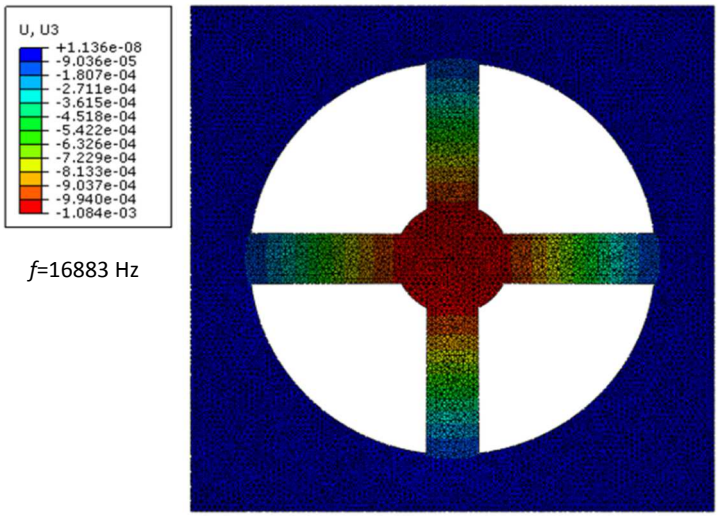

Figure 2.24: First mode shape of R3 resonator at 16883 Hz

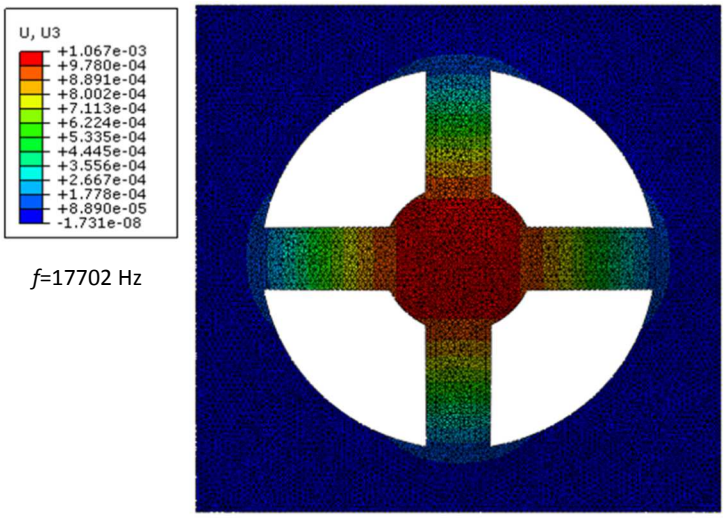

Figure 2.25: First mode shape of R4 resonator at 17702 Hz

The modal analysis was also done for the wave guide itself. This would determine if the fundamental mode of the plate would have any interference with the frequency range of interest for the resonators' band gaps. The mesh size and boundary conditions for the plate are different due to the difference in the dimensions and the low-stiffness boundary fixture along the edges. The simulated first mode shape is shown in figure 2.26 and the modal frequency that is simulated comes

out to be 94 Hz. This gives clarity that the first global mode of the wave guide is much lower than the band gap frequency ranges of interest.

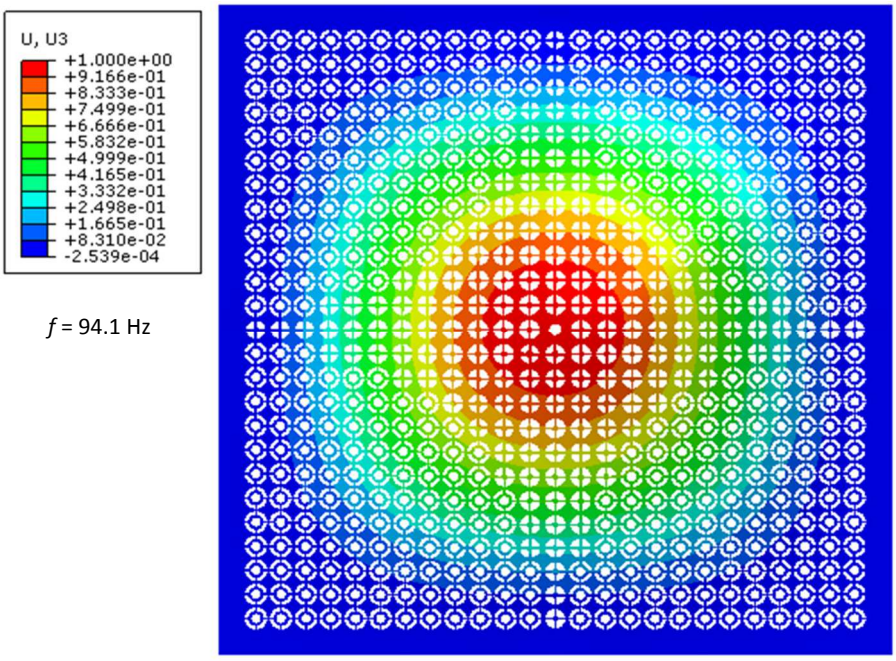

Figure 2.26: First (global) mode shape of the wave guide at 94.1 Hz obtained through Abaqus modal simulation.

The resonators' natural frequencies and the band gap frequency ranges associated with them are shown within table 2.5, where ω_U is found by utilizing equation 2.3. It is found that the resonators R1, R3 and R4 have non-overlapping band gap. However, the band gap associated with R2 resonator overlaps with the band gaps of both the R1 and R3 resonators. This will play a role in the results that are seen when experimentally testing the wave guide.

Resonator band gap ranges					
Parameter	**R0**	**R1**	**R2**	**R3**	**R4**
ω_L (Hz)	15739	15938	16321	16883	17702
ω_U (Hz)	19840	16887	17333	17767	18865
Frequency range (Hz)	4101	949	1012	884	1163

Table 2.5: Band gap frequency ranges for the built-in resonators in the passive-adaptive wave guide

Further, a transient steady state numerical analysis was done for the wave guide. in the transient simulation is done in the time domain to extract displacement vs time history . The frequency spectrum of the output response is obtained by taking the FFT of the time domain data. To correctly perform an FFT for the steady state response alone, the time domain data was snipped to obtain only the steady state response portion and padded the data with zeros to reach 4096 data points.

The wave guide's response was simulated at several discrete frequency points and analyzed to determine the regions of propagation and attenuation. The response was obtained from the lower ends of the frequency range of interest, around 16 kHz up to the upper frequency range of 19 kHz for the locations labeled North, South, East, West, and South-East in figure 2.17.

Starting with the lowest frequency and working the way up we see that at 16 kHz shown in figure 2.27, there is propagation in each of the axial or cardinal directions as well as in the South-East direction. The propagation along the cardinal directions can be explained due to this being at the lower frequency ranges where only the R1 resonator in the North is missing so the only area that should be attenuated is the North. However, looking into other frequencies it can be noted that the amplitude at 16 kHz for North direction is around half of what is seen at the higher frequencies, indicating attenuation.

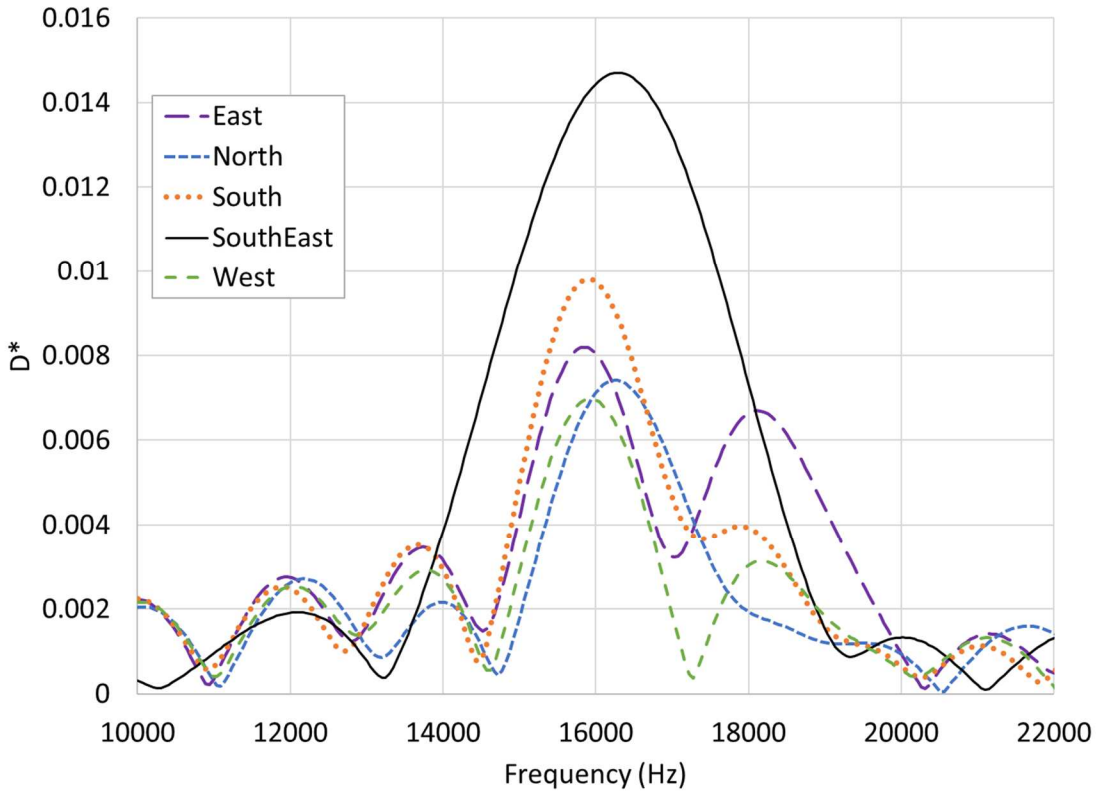

Figure 2.27: Frequency spectra of the output responses at the axial monitoring locations for a harmonic input of 16 kHz at the center.

When looking at an excitation frequency of 17 kHz as shown in figure 2.28, we see that there is a high degree of attenuation in the South and some attenuation in the West directions. This is somewhat distinct from what the theory would predict as from earlier findings we know that around 17 kHz there should be propagation in the regions where the band gaps of the R2 and R3 resonators are missing, so the results shown are not entirely conclusive. This could be a case where the higher global modes of the plate interact with the modes of the resonators. Further, the overlapping band gaps corresponding to R2 and R3 and any potential variations in actual resonator frequencies may have a role to play.

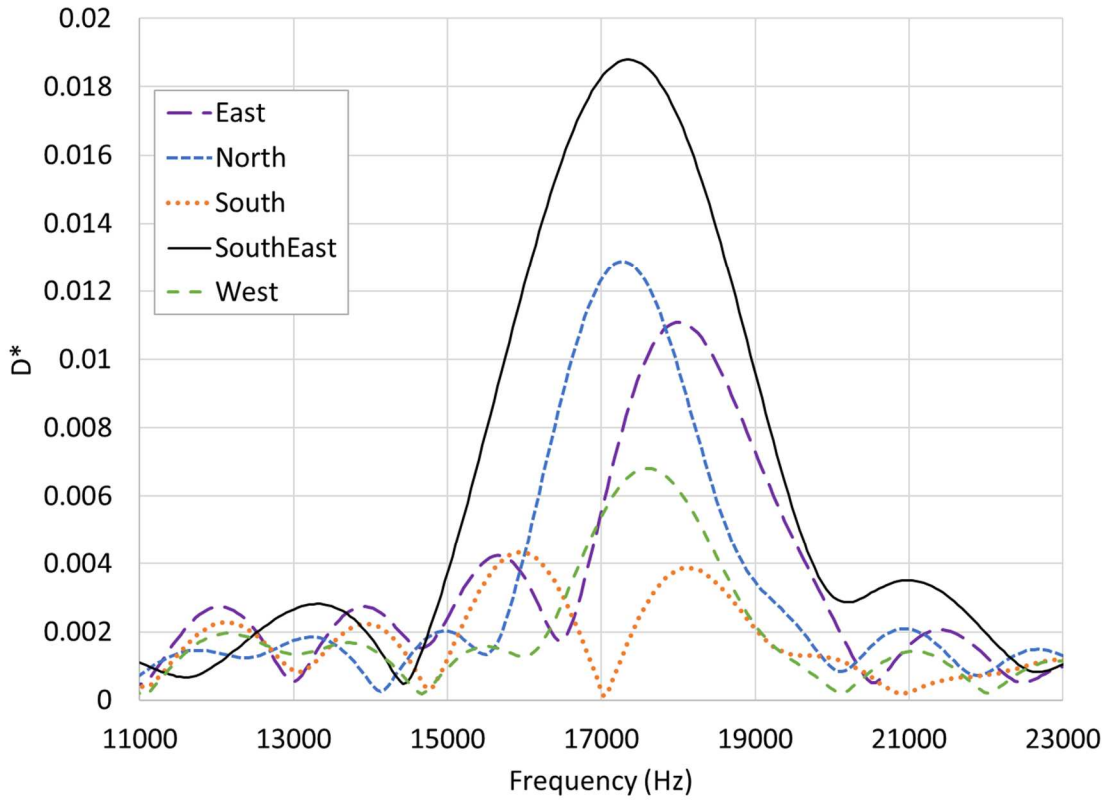

Figure 2.28: Frequency spectra of the output responses at the axial monitoring locations for a harmonic input of 17 kHz at the center.

For the 18 kHz test case shown in figure 2.29, there is attenuation along all axial directions except the East where the R4 resonator is missing. As theory-based band gap frequency ranges would suggest, this correlates well as there should be a range around 18 kHz where propagation should be seen where the R4 resonators are missing but the other resonators are present as is seen here.

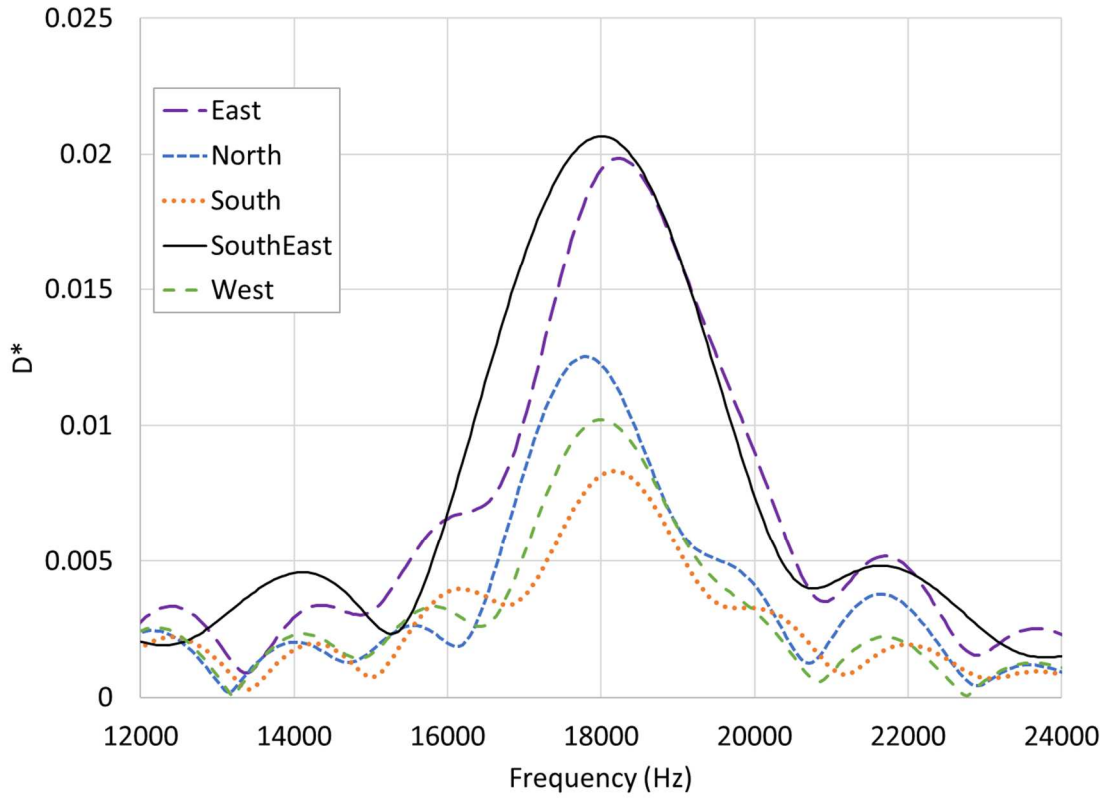

Figure 2.29: Frequency spectra of the output responses at the axial monitoring locations for a harmonic input of 18 kHz at the center.

The last test case that was simulated was that of the 19 kHz excitation frequency shown in figure 2.30. This shows the same phenomena that is seen with the 18 kHz frequency simulation, it is seen that the East direction is propagated and the remaining axial directions are attenuated. This once again matches with what theory would suggest. To better understand why the band gap for R4 resonators display the desired effect better than the others, further investigations are conducted. The directional cases need to be compared more closely for attenuation and propagation at a finer frequency resolution. This would give a better insight about the performance within the frequency range of interest. It is also noted that there may be higher global modes of the plate that may inhibit the attenuation behavior as designed for through the selection and patterning of the resonators in the wave guide.

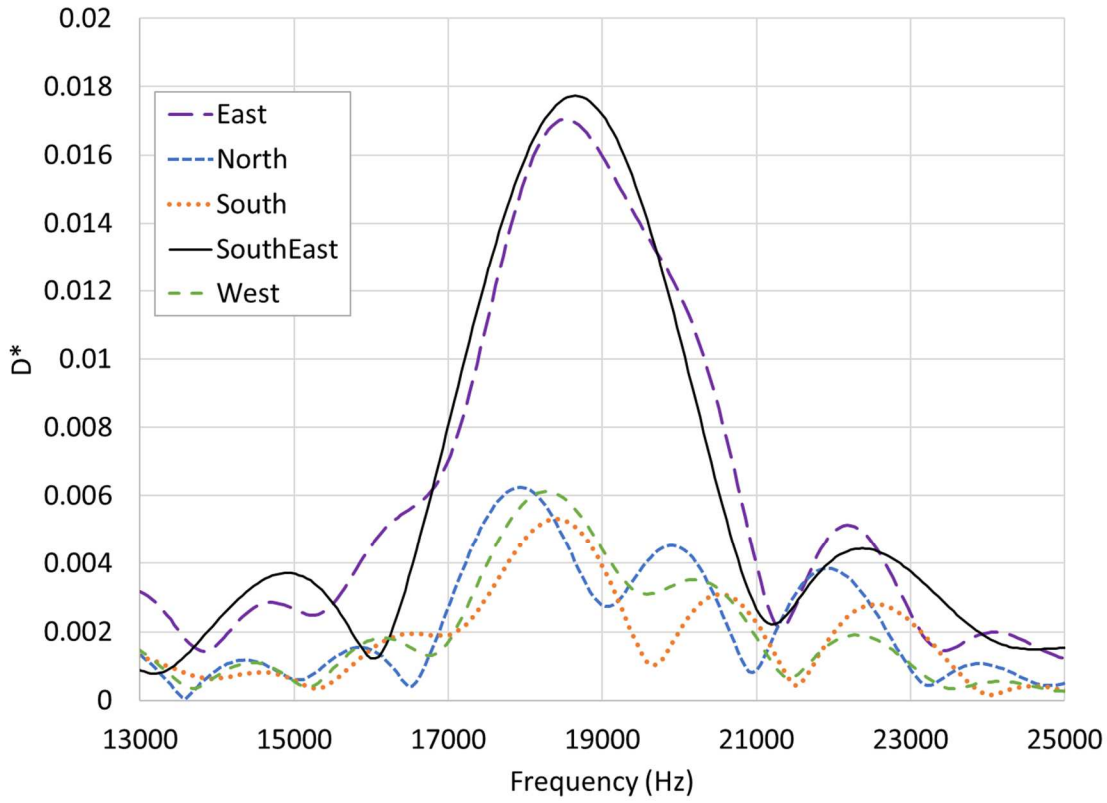

Figure 2.30: Frequency spectra of the output responses at the axial monitoring locations for a harmonic input of 19 kHz at the center.

Looking further into the comparison of the FFTs for different excitation frequency cases within the R1 resonator which is missing in the North direction, shown in figure 2.31, it is seen that there is attenuation at both the 16 and 19 kHz frequencies. However, there is also propagation that is seen within the 17 and 18 kHz frequencies. The 17 kHz frequency is understood as it should be propagated, or seen some propagation around that point. However, the 18 kHz frequency should be attenuated, so either the frequency is shifted higher than what was originally expected or there may be coupling between the plates global modes and the frequencies experienced by the resonators.

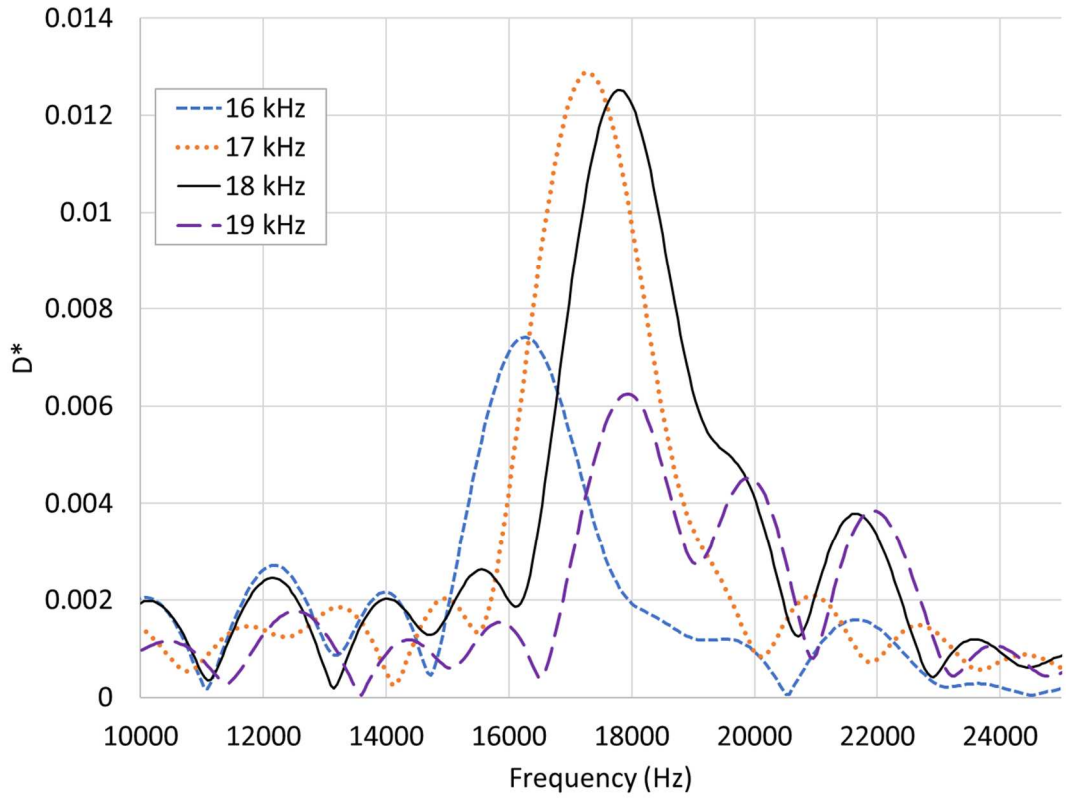

Figure 2.31: Frequency spectra of the output responses at the axial monitoring locations for a harmonic input in the North direction (R1 missing).

Within the west direction where R2 is missing, the data as shown in figure 2.32, concludes that there is propagation around 18 kHz and the other frequencies tend to see some form of attenuation. Which is expected, as the frequency range of the R2 resonator should propagate around 17-17.5 kHz, outside of this range we see a sense of attenuation. The frequency if tested closer around the range of 17.5 is believed to propagate more than what is shown here, which would suggest that what we are seeing is in line with what theory says also.

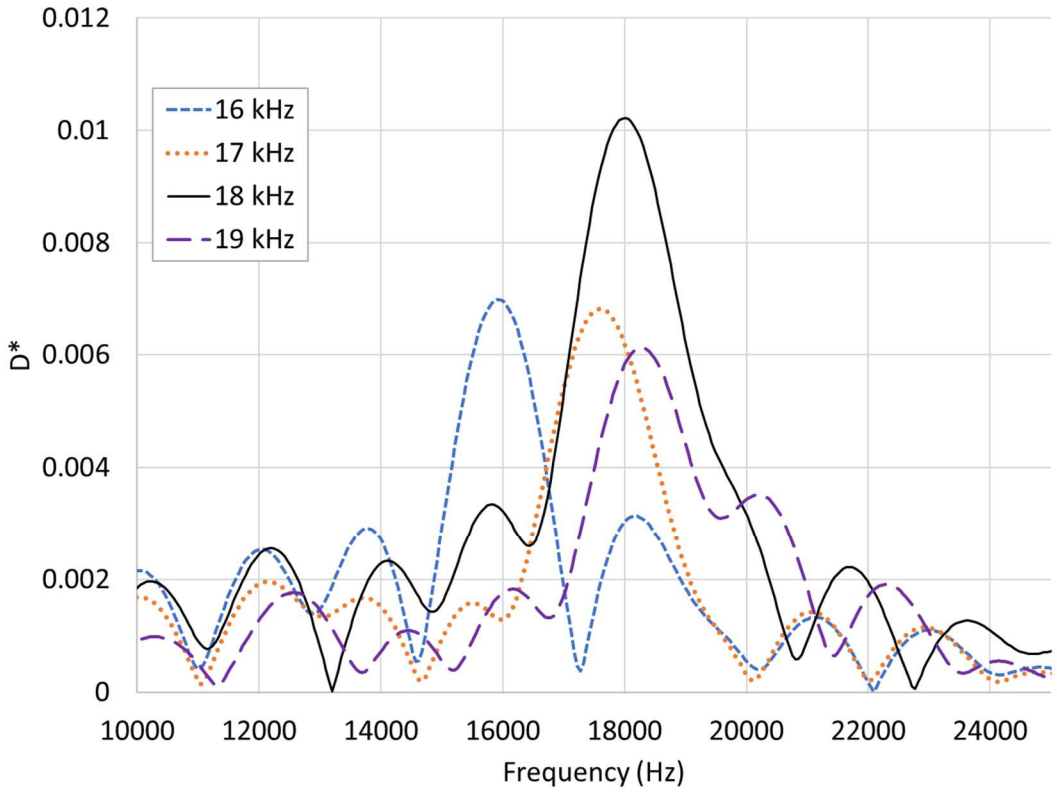

Figure 2.32: Frequency spectra of the output responses at the axial monitoring locations for a harmonic input in the West direction (R2 missing).

The R3 resonator data, shown in figure 2.33, occurs in the South direction of the wave guide. Upon closer inspection it is seen that there is propagation at the lower range and around 18 kHz frequencies. The 18 kHz frequency lies within the range of the resonator's band gap and so propagation is expected, however, the 16 kHz lies outside of the frequency range and should be attenuated by the previous resonators. This can be described by the frequency of 16 kHz lying outside of the range of interest so some of the frequencies may pass through and outside of the band gaps there should be propagation so this may be what is being seen by this frequency range.

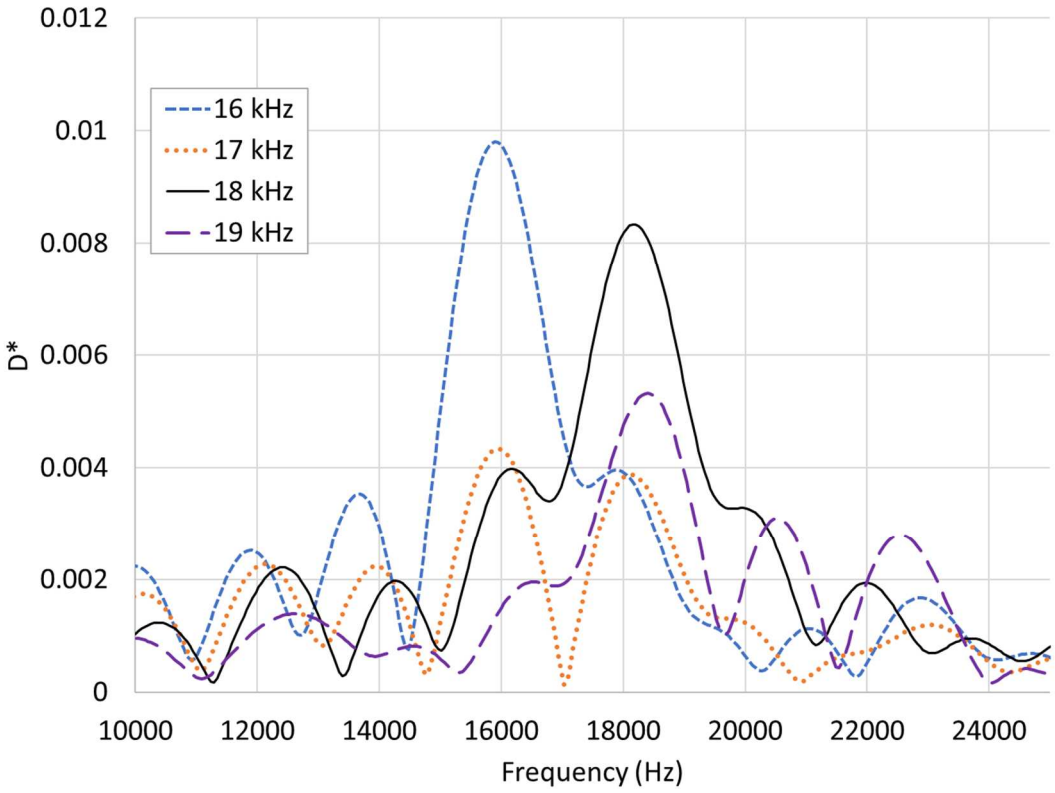

Figure 2.33: Frequency spectra of the output responses at the axial monitoring locations for a harmonic input in the South direction (R3 missing).

The last direction is the East where the R4 resonator is missing, the data is shown in figure 2.34, and is shown to have propagation around 18 and 19 kHz frequencies. This data is the most prevalent as it is what is expected. The propagation lies within the band gap of the R4 resonator and the remaining two frequencies show attenuation. This gives confidence as to the simulations and the phenomena that is expected.

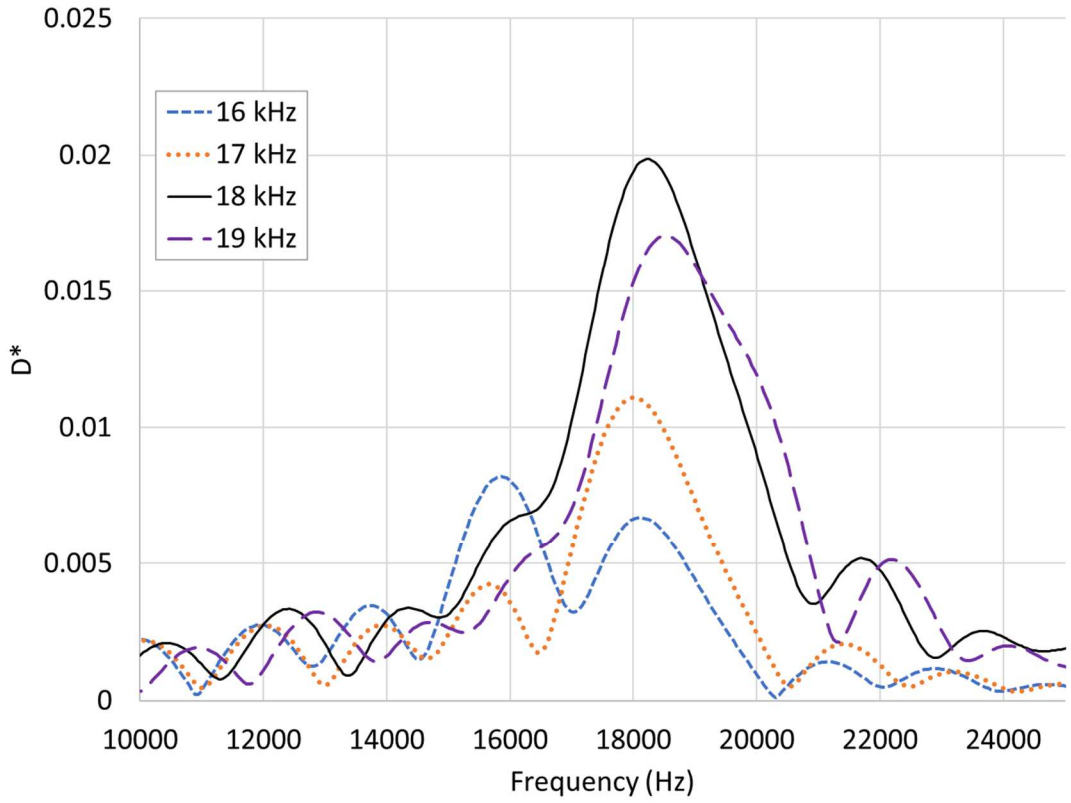

Figure 2.34: Frequency spectra of the output responses at the axial monitoring locations for a harmonic input in the East direction (R4 missing).

While the varying data simulations are not always showing what is expected there is still a glimmer of hope, as seen with the R4 resonator. To have any more decisive conclusions a more in depth study would need to be done characterizing the FEM data into more concise increments and running the test at more than a single point in each direction. By adding more pick-up locations it would also allow for the data to show the attenuation of the frequencies along a set path. This would give a confirmation as to if the attenuation is happening as it should and how much of the frequency response is still passing through at the specific location.

2.3.3 Steady-State Transmissibility Tests

The idea behind testing the wave guide's frequency response at different key points was that there should be key points of attenuation and propagation whether the frequency being tested falls in the band gap of the resonator. In theory, the wave guide should see attenuation within the band gap and propagation outside. The key area of interest being looked into with the wave guide is that if several different resonator are placed in series there should be a larger area of attenuation. Attenuation should occur within the band gap and outside of this band gap propagation should occur.

In order to see the attenuation of the band gap the plate was excited at the center with a piezo actuator, which simulated a wave that propagated throughout the system until reaching steady state. Before testing the wave guide the tension of the plate would need to be analyzed by increasing or decreasing the height. This tension would allow the plate to be vibrating in the proper manner acting like transverse waves, the tension is also considered as a preload condition for the piezo.

To test the wave guide an initial displacement reading of 3e-6 m would be taken at the center of the plate and a reading would be taken from a resonator in each of the different directions. The two points would be normalized together to get a clear picture of what happens when each of the resonators are excited at the same input displacement. The reading would be taken between the first and second to last resonator in each direction, this would give one resonator of each type and should give an idea as to what frequency ranges are attenuated and propagated. A test point would also be taken in the South-East direction corresponding to the R0 resonator where all frequencies should be attenuated. The testing was done in increments of 500 Hz, starting at 15 kHz and extending to 20 kHz, with a few outer lying frequencies checked to determine if there was propagation outside of the band gap as theory would suggest.

When looking into the directions of interest there are clear areas of propagation, however, there are also areas of attenuation within the frequency ranges of interest. In theory this is the result that is expected to see and in most cases this is what was seen within the experiments. There are however certain cases where this did not fully happen, there are several reasons as to why this may be the case. There is a possibility that the reflections will play an effect on the system, there are also instances where the frequencies of interest seem to be shifted. However, overall the system resembles what is theoretically predicted, each direction of interest has separate areas of attenuation and propagation.

Using table 2.5 as a guide to know where the band gap occurs it can be noted that in the North direction where R1 is missing there should be propagation around 16-17 kHz. From figure 2.35 it can be noted that at 16 kHz there is not complete attenuation yet, however, there is still a trend of attenuation in the direction beyond 16 kHz. The most propagation within the North direction comes from around 15-16 kHz, giving a shift in the frequency range that may be caused by interactions between the reflections and the boundary not being completely fixed. It can also be noted that there exists a sense of propagation outside of the band gap or a trend insinuating that there is possible propagation above and below the band gap.

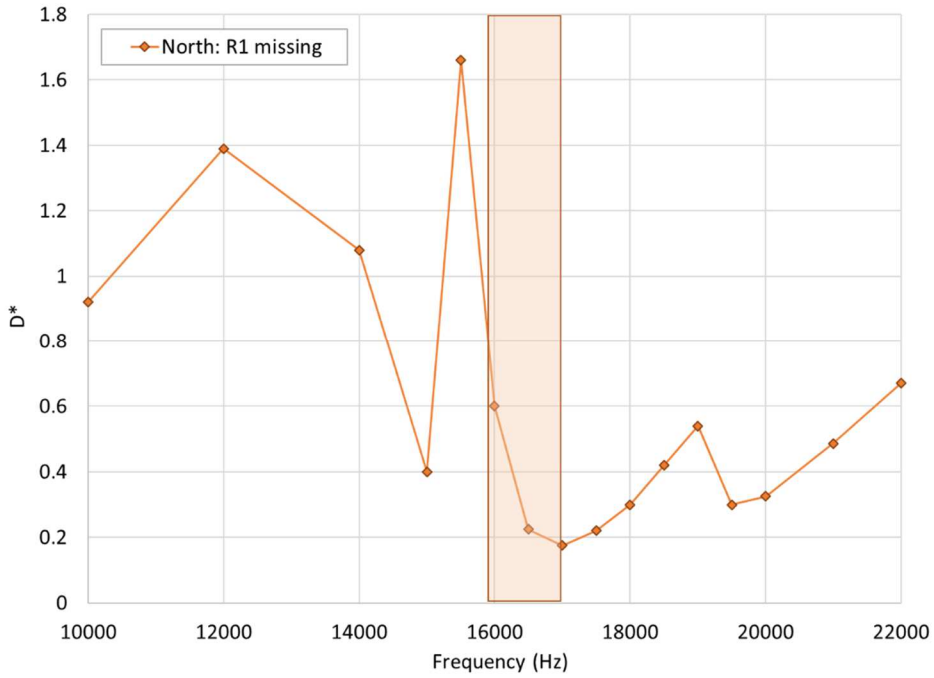

Figure 2.35: Displacement transmissibility versus excitation frequency for the passive-adaptive wave guide test article monitored at the North location under steady-state condition. The shaded portion represents the theoretical band gap frequency range.

Within the East direction, the resonator, which is missing, is the R4 resonator shows the most prominent feature of the attenuation phenomena. The band gap of the R4 resonator should lie within 17.7-18.9 kHz, and from figure 2.36, it can be shown that there is a sense of attenuation within this range of frequencies. However, both the lower and upper regions of the frequency range tend propagate outside of this attenuated area meaning that the frequency may be larger than what was originally simulated. On the upper region, the frequencies start to propagate around 19-19.5 kHz and on the lower end the frequencies seem to remain attenuated outside of the band gap until 17 kHz where there is a sole peak. This could very well be true as the frequency value used is a simulation value and assumptions were used within the simulation to insure that a good idea of where the frequencies lie could be obtained.

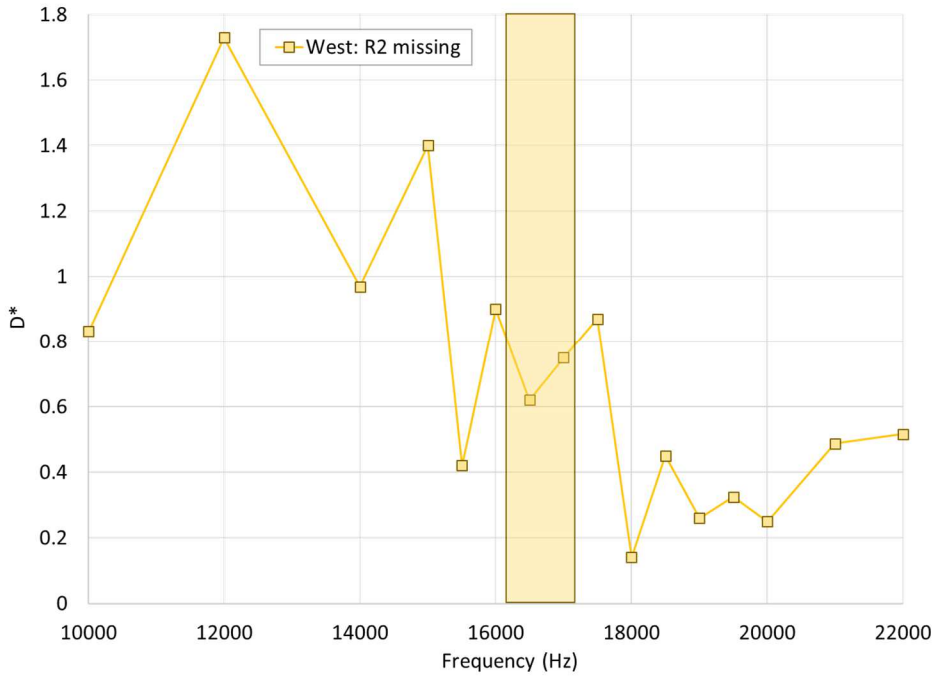

Figure 2.36: Displacement transmissibility versus excitation frequency for the passive-adaptive wave guide test article monitored at the East location under steady-state condition. The shaded portion represents the theoretical band gap frequency range.

In the south direction where R3 was missing, there should be attenuation in and around 16.8-17.7 kHz, however, from the results in figure 2.37 it is shown that there is an area of propagation around 17.5-18.5 kHz. The higher peak around 17.5 kHz could be due to each resonator, while initially designed to have its own band gap the band gaps do overlap and for the R3 resonator the only area where it is the sole frequency is from 17.3-17.7 kHz. From the figure it is seen that the attenuation occurs around 17 kHz and past 18.5 kHz insinuating that the frequencies outside of the R3 band gap are attenuated. The shifted frequency of the R3 band gap can also be noted as it has also been seen within the other resonator units also.

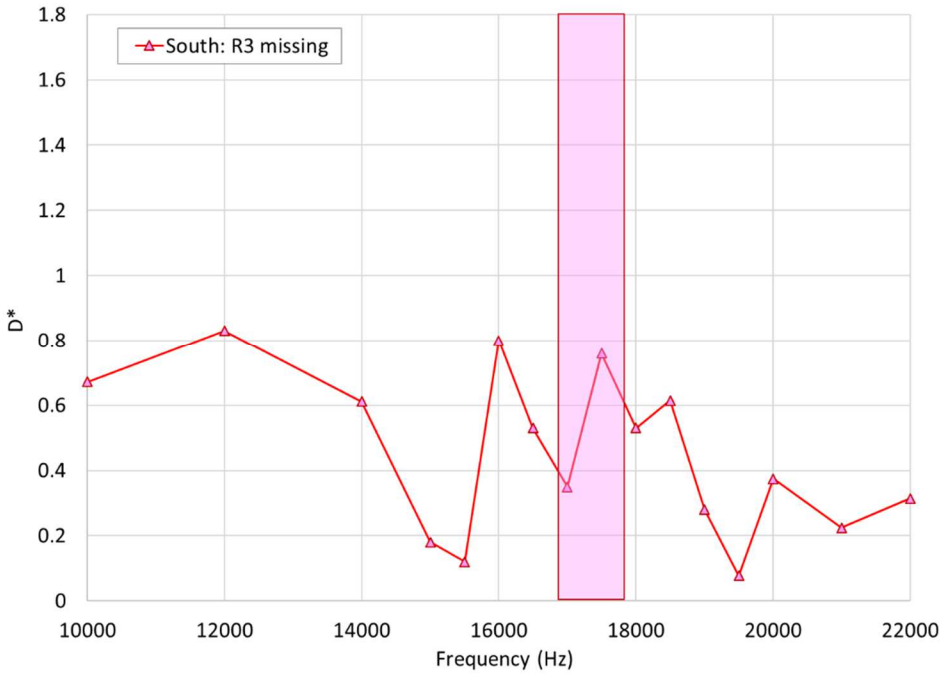

Figure 2.37: Displacement transmissibility versus excitation frequency for the passive-adaptive wave guide test article monitored at the South location under steady-state condition. The shaded portion represents the theoretical band gap frequency range.

The sole remaining main directional resonator located in the west is that of where the R2 resonator is missing. From figure 2.38 and table 2.5, it can be noted that around 16.3-17.3 kHz is the band gap where propagation should occur. It is shown that on the lower end (below 15 kHz) and on the upper range (above 20 kHz), there are signs that insinuate propagation. However, within the band gap there is no clear sign of attenuation, this is due to the R2 band gap not having a clear area where it is the sole frequency acting within that band gap. The R1 band gap extends to 16.9 kHz and the R3 band gap starts at 16.8 kHz, so in the west the frequencies experienced will be more of the vague frequencies experienced through reflections and what few frequencies that are not previously attenuated by the other resonators in the series. The area outside of the R2 band gap has shown signs of attenuation, and there are signs of propagation within and around the R2 band gap. This gives a clear and decisive picture as to what should happen when placing the different

resonators in series, there should be a region such as with the R2 resonator where there is a band of propagation and outside of this region, there should be attenuation.

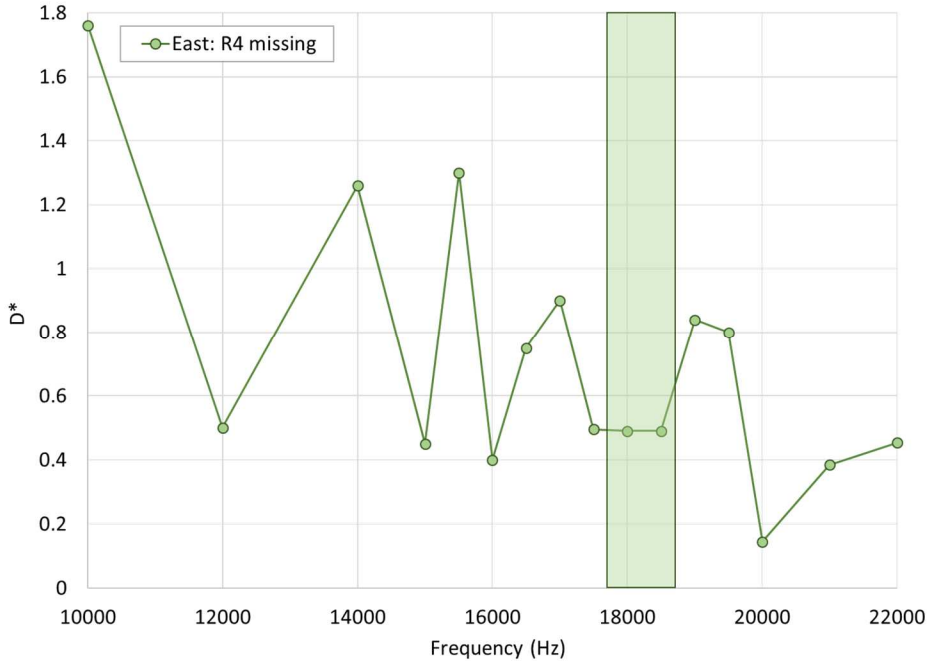

Figure 2.38: Displacement transmissibility versus excitation frequency for the passive-adaptive wave guide test article monitored at the West location under steady-state condition. The shaded portion represents the theoretical band gap frequency range.

The last area of interest is the South-East where the R0 resonators lie, the theory behind the R0 units is that there should really be no propagation at all. However, the results in figure 2.39 try to speak a different story, one where there seems to be much more propagation than what there really is. From the R0 resonator the initial band gap extended from 15.7-19.8 kHz, but the results show that from about 15-21 kHz there is a sense of attenuation. Outside of these ranges on both the upper and lower ends, there is a trend insinuating propagation. While within this band gap there still are peaks that may scream propagation it also says that while these peaks may be a bit larger than the areas of attenuation when compared with the other resonator peaks this lines up with many of the other areas of attenuation. These larger peaks may however be the result of reflections and

nonlinearities throughout the diagonal of the plate since the diagonal has a different wavelength than the rest of the plate.

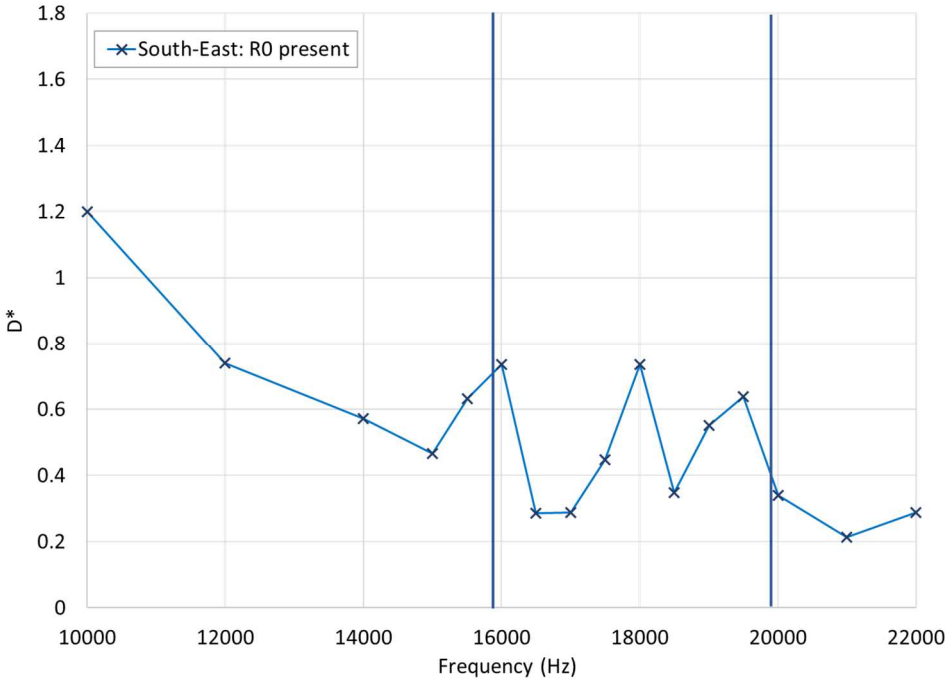

Figure 2.39: Displacement transmissibility versus excitation frequency for the passive-adaptive wave guide test article monitored at the South-East location under steady-state condition. The shaded portion represents the theoretical band gap frequency range.

While the results give the idea of propagation in the frequency range of the resonator that is missing there are some discrepancies within the data due to dispersion and global modes of the plate disrupting the sought after effects. Dispersion within the plate happens when waves are travelling at different speeds, this is seen in the South-East direction where the wavelengths differ from the wavelengths in the cardinal directions. The second discrepancy, the global modes, is due to the small sizes of the plate and the different resonators acting around each other. This limits the amount of propagation and attenuation that can is seen, the different frequencies that are shown

also give an idea as to why there are other frequencies propagated where the frequencies should be attenuated.

2.4 Summary

The effect that has been sought after within the wave guide is that of attenuation within the band gap when there are a series of resonators whose band gaps cover different frequency ranges and a "missing resonator" where propagation should occur. It is shown that there are key areas that show a trend of propagation and an area outside where attenuation occurs. When the R0 resonators are looked into there is a clear definition of attenuation in this area, however, there are also areas that propagation occurs. These areas of propagation are explained as being caused by the global modes due to the small scale dimensions of the plate and the differences in the wavelengths in the ordinal direction. Overall, the summary can be concluded by saying that there is attenuation within the band gaps of the resonators making up the cardinal directions and there is propagation in the band gap of the missing resonator unit.

While some frequencies may see discrepancies due to global modes interacting and others may see results caused by dispersion, there are still key points as to where the propagation of the frequencies is experienced. It is this concept that allows the use of the word "meta-configured", it's the ability to go beyond the capabilities of the normal wave guiding structures and enhance them to a smaller scale by focusing on the abilities of the resonators themselves which are configured together to increase the functionality of the plate as a whole.

CHAPTER III

PASSIVE-ADAPTIVE TUNED VIBRATION ABSORBERS

3.1 Introduction

Since its conception in the early 1900's, the idea of a tuned vibration absorber (TVA) has been studied to find a passive-adaptive mode of vibration suppression. Throughout the history of TVAs many designs have been studied and analyzed in order to find more optimal tuning methods. One of the early works was by Ormondroyd and Hartog [51], in which dynamic vibration absorbers were studied. The work done by Hartog formed the basis for the many TVA designs and has been furthered in several directions. The original TVA was a single degree-of-freedom design and was later extended to multiple degree-of-freedom designs [52-53] to further enhance the optimal vibration isolation of systems employing them. These studies showed that by monitoring and changing the location of the absorbers, even when not specifically tuned to a particular mode the absorber can help attenuate the system's response.

Plate-like vibration absorbers originally introduced by Snowdon [54] were shown to act as either springs or dampers. These inner resonators are attached to the vibrating structures and are found to be highly effective with suppressing vibrations. The study in this area was furthered by Kerlin [55] to understand the optimal tuning of a dynamic absorber. This motivates the idea of utilizing an adaptive resonator with a second mass that can be configured based on the input as one possible solution for passive-adaptive vibration suppression.

A more recent solution to the problem is to use a plate with multiple vibration absorbers [56] giving a narrow band control with respect to its damping and frequency range. Further, enlarging the bandwidth allows for a control of the optimal location for the absorbers, which can be tuned by the plate's mode. This study gives a basis of how vibration is suppressed in a plate and gives possibilities for future applications in band control. Ryaboy [57] shows a further confirmation of the idea noting that different criteria such as the splitting of stiffness and placing the absorbers in key locations allows for more desirable results.

Vibration reduction has also been demonstrated using magnetorheological elastomers vibration absorbers (MRE's) [58] where a semi-active control method is used to attenuate nonlinear vibrations using a flexible arm. Normal elastomers focus on the viscoelasticity properties of the materials; while the MRE's additionally use their magnetic field to reduce vibrations via the internal resonance of the materials flexible arms. The MRE in study was able to transfer and dissipate the energy by acting as a variable magnetic spring, which controlled the coil current in the materials flexible arm. Other MRE studies [59] have introduced the use of silicone gels and iron micro particles to implement a squeeze mode in the tunable springs shifting the frequencies used for vibration absorption within a fuselage. However, the problem within the MRE's is that the vibration absorbers lose their functionality after a number of cycles.

Adaptive TVAs can be classified into two subcategories – passive-adaptive and active TVAs. An adaptive TVA is able to favorably alter its response based on the dynamic input provided to it. For a passive-adaptive system, the propensity for this alteration is built-in to the design of the TVA without the need for any additional inputs, whereas an active system utilizes additional input such as those via feedback control signals through transducers, typically delivering better tunability. However, active systems usually result in more complexity and penalties in terms of weight, volume and overall cost so as not to be practical in many cases. It is in this context that passive-adaptive design innovations become desirable. An early approach to improve passive-

adaptivity for vibration absorbers is by the use of a two-mass oscillator [60]. The two-mass oscillator provides some passive tunability that enhances its performance beyond its single mass counterpart. However, this is just one early instance towards achieving more efficient passive adaptivity for dynamical systems such as TVAs.

The use of passive-adaptive TVAs is also seen in the context of flutter [61-62], it is shown in these studies that flutter is effectively reduced through means of torque hardening of the pitch and linear restoring torque in the flap when using linearly tuned vibration absorbers. By changing the mechanical properties of the wings pitch and/or flap, namely the stiffness, the TVAs experience the detuning effect at a much smaller rate. So, while the effect of the TVA are noted regarding vibration mitigation there is also an aspect in which the opposite is seen and the TVAs are detuned. Overall, the passive-adaptive TVAs allow the ability to manipulate the mechanical properties and keep the TVAs at a smaller scale; however, the detuning effect is still an underlying issue.

One solution to the concept of active TVAs is via the use of shape-memory alloys (SMAs) [63], which proposes using the low complexity and stability of the passive tuned absorbers utilizing no moving parts or complex mechanisms, while also using the robust performance of active controls. It was found that by manually tuning the SMA through means of heating the TVA and by manipulating the elastic modulus the tonal vibrations across a range of frequencies could be attenuated. Allowing for mitigation of aero elastic phenomena using SMAs without the normal high complexity aspect. While SMAs exhibit a larger reduction in vibration mitigation, there is also a high system complexity and the need for a constant energy source.

Within both the passive-adaptive and the SMAs it is seen that there exists a possibility to tune the vibration absorber to a frequency, however, there is a detuning effect of the TVA as well. A study by Abhishek and Manobala [64], in which a more basic version of a TVA consisting of only a tip mass on each cantilever arm is studied and modified to suppress the vibrations in a

washing machine. In this study a vibration absorber, in the form of a dumbbell-shaped device is hung from transmission lines to mitigate fatigue effects. Expansion of the original vibration absorber through the addition of a TVA attached to the tips of each cantilever arm and studying the addition of heat for retuning capabilities took the concept a step further. Through expanding, the original capabilities of the TVA two things were found: the extra mass gave an ability to finely tune the TVA and by applying heat the ability to increase and decrease the amount of dissipated energy was found.

These studies motivate investigating the concept of achieving a passive-adaptive TVA using meta-configuration. Specifically, can meta-configuration be used to enhance passive-adaptivity for TVAs for aerospace applications. Such a TVA is intended as a structural device that enhances mitigation of flutter and vibrations for aerospace structures. The basic (or conventional) passive TVA currently employed has a resonator that is usually realized using a tip-loaded cantilever beam. It is desirable that this enhancement of performance through passive-adaptivity be realized without incurring any impractically high penalties in terms of weight, complexity or cost of the solution. Therefore, the potential to redistribute the resonating mass so as to enhance tunability through meta-configuration is worth investigating. If a part of the total resonating mass is apportioned to a 'riding' mass that is retained to move axially along the cantilever beam under spring tension or compression. This riding mass is able to self-position itself along the cantilever beam depending on the dynamic tuning parameters in relation to the input excitation. In very rudimentary terms (omitting interactive effects), one might imagine the riding mass self-tuning the resonator to match the input frequency depending on the amplitude of the input excitation due to its ability to move along the axis of the beam.

The question remains as to how this concept works, i.e. how does the passive-adaptive TVA suppress vibrations over a broader bandwidth? While the nonlinear dynamics of the riding-mass-based passive-adaptive TVA concept is complex and requires detailed analytical and

numerical studies to characterize in its entirety, this study aims to probe proof-of-concept for this approach using experimental test cases. By changing the damping characteristics of a TVA it is also possible to change the resonant characteristics creating a broadband vibrations problem [65]. Expanding the idea of a riding-mass by incorporating meta-configuration and adding damping capabilities, then the concept of expanding the bandwidth is also viable.

While the concepts of this ilk are known from before [51, 54] there remains opportunities to investigate innovative configurations, design optimization, and proof-of-concept to enable practical solutions. First, preliminary designs is set forth within this chapter supported by simple FEM analyses, followed by experiments on a few fundamental variants and discussion of results thereof. Finally a summary of the results found throughout this study is given.

3.2 Materials and Methods

The wave problem, or in better terms the steady state vibrations problem that is introduced through the TVAs, can be understood through using a modal shaker to simulate the dynamic responses. An initial study was configured using a baseline TVA to understand the dynamic characteristics and later expanded to incorporate a study on the effects of adding a tip-attached mass or a base attached mass. The experiments were used to see if there is the possibility of increasing a TVAs natural bandwidth through passive-adaptive techniques while keeping the lower band structure. To give an understanding of the frequencies of interest, FEM simulations were used to understand the resonance of the structures and calculate the TVA configurations varying bandwidths. Further experiments to simulate the dynamic responses were captured with a laser vibrometer and using a high-speed camera to confirm the results by calculating the captured cycles over a period. The work presented gives the techniques, findings, and limitations of the study on expanding the bandwidth of isolation for a TVA.

3.2.1 Experimental Setup

Many of the same apparatus that was used to understand the vibrations of the wave guide were also used in the testing of the TVA. However, at the same time there were other unique apparatus used that was not previously seen. The same function generator, signal conditioner, laser vibrometer, and DAQ were used, however, a new LabVIEW program was created to analyze the data, and a different shaker was used. As in the previous experiment, the function generator was used in order to create a sine wave, this sine wave will generate a single output as to where a specific frequency of interest will be higher than the other frequencies.

The LabVIEW Program that was used within the previous experiment was reconfigured to better analyze the results, but the same techniques and processes were used to do so. The only change was the new program extended the capabilities to analyze the samples for energy harvesting capabilities. In order to obtain the results a function generator is used to generate a sine wave signal.

The function generator is connected to the signal conditioner, in order to convert the analog signal into the sought after digital signal. The first step into doing this is understanding sampling rate or the sampling frequency. Put more simply it is the amount of samples or data points taken within a second, in order to avoid aliasing the Nyquist theorem is used. The second concept that needs to be understood is the resolution or the precision of the signal. The resolution is the accuracy at which the system is understood or the amount of data points picked up in the system.

The processed data can be input into the DAQ through use of the LabVIEW program, however, the signal first needs to be obtained from the laser vibrometer. The laser vibrometer utilizes the same technique as previously seen where it takes the data from different reference points throughout the system and outputs the signal as a velocity, which the LabVIEW program converts, to the displacement spectrum. However, there is a downfall with the vibrometer, the vibrometer can only pick up the velocity to a certain range (125 mm/s/V) and beyond this point the data cannot

be obtained. This phenomena is seen throughout several of the test points where the velocity of the cantilever arms are beyond the capabilities of the vibrometer. To understand the frequencies and the displacements at these instances the use of a high-speed camera was added to pick up the simulated displacement. From the captured video, the natural frequency could be found through counting the cycles experienced over a period. Additionally checks to verify the vibrometer data were made through the manufacturer calibration and the use of transducers.

In order to insinuate vibrations a modal shaker was used, the purpose of the shaker is to identify the natural frequencies, mode shapes, stiffness, and damping capabilities. The modal shaker takes an amplified input frequency from the waveform generator and excites the specified object. In this case, a base structure was modeled in SolidWorks and shown in figure 3.1; the purpose of this article is to create a solid and leveled surface, which the actual setup can be placed with the least amount of errant disarray. This article also created a secure base connecting the shaker and the test article. The shaker is attached to an amplifier that increases the power of the signal.

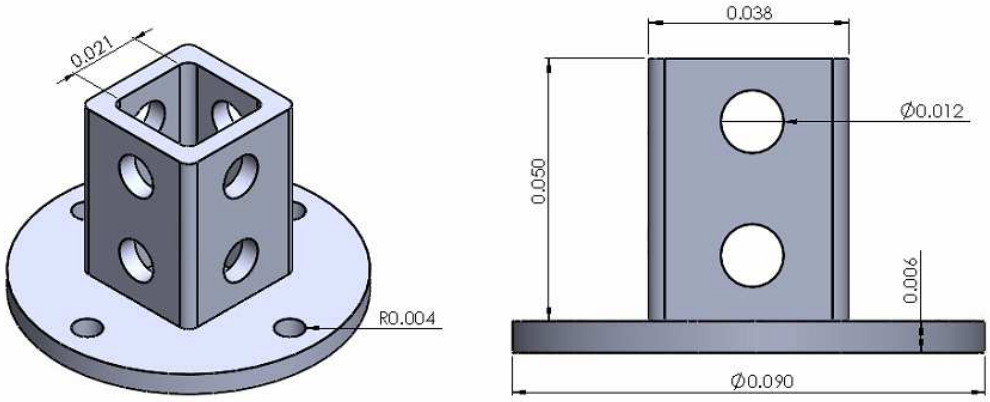

Figure 3.1: SolidWorks model of the base attachment fixture for the TVA test articles.

To create the testing apparatus shown in figure 3.2, a galvanized steel beam extending upwards for four inches was used. From this beam the use of aluminum, bolts were used to secure the beam to the base structure, in the top slot a steel cantilever was extruded from either side of the

apparatus. The cantilevers produce desired effect from either cantilever, however, the use of a dual cantilever system gives the ability to a) see if the two sides will coincide to around the same results and b) give a form of symmetry about the axis.

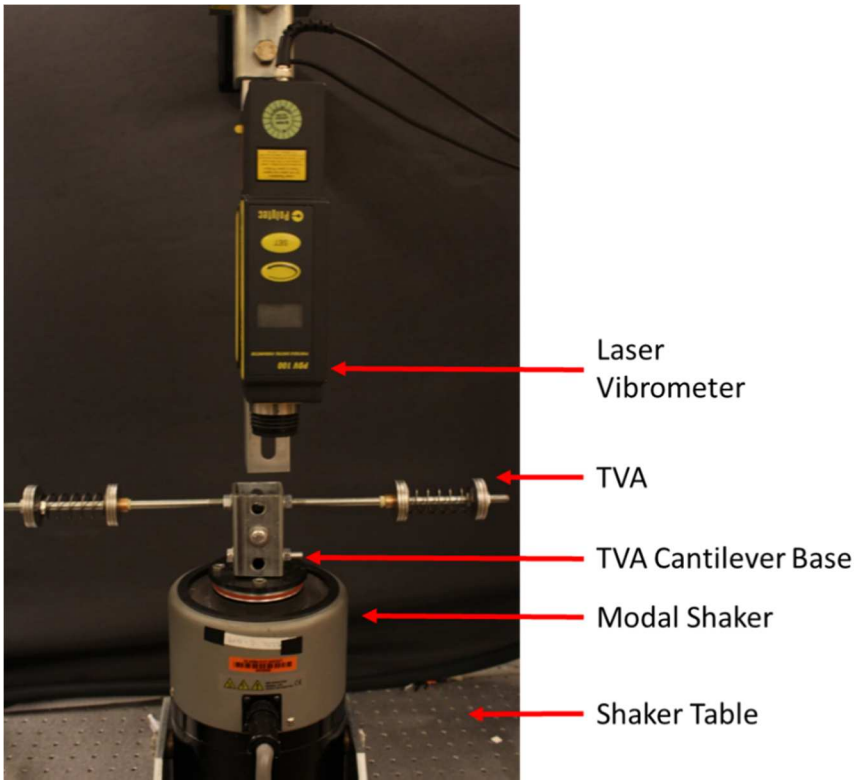

Figure 3.2: TVA experimental set-up showing various components involved.

In order to give the system a boundary that was fixed the two cantilevers were joined at the middle through a series of nuts. To fasten the nuts a series of torqueing procedures were undergone, a value of 13 lbf-ft was used since this is the standard for a grade 5 nut with 5/16 in standard diameter, as shown in table 3.1. The torqueing creates a fixed end cantilever with the opposite ends being free ends and prevents the vibrations from causing the nuts to come loose.

Torqueing guidelines		
Diameter (in)	**Standard hex-bolt (lbf-ft)**	**Flange-head bolt (lbf-ft)**
0.25	6.3	7.3
0.3125	13	14
0.375	23	26
0.5	57	64

Table 3.1: Torqueing guidelines chart [66]

3.2.1.1 *Baseline TVA*

The initial TVA can be modeled by assuming the system to be that of a cantilever loaded with a tip mass. The calculation for a cantilever with a tip mass was derived to be [67]:

$$f = \frac{1}{2\pi}\sqrt{\frac{3EI}{mL^3}} \tag{3.1}$$

Where E is the Young's modulus, I is the area moment of inertia, m is 0.23 times the mass of the cantilever plus the tip mass, and L is the length of the cantilever. However, since the total mass is not responding to the forces acting on the cantilever an effective mass is used. The equation for the effective mass is found by using equation 2.2, it is seen that the complete tip mass is taken and only a portion of the cantilevers mass is taken into effect.

To simulate a tip mass a series of washers were used at the end of the cantilever, the mass of the washers were analyzed and came out to be 73.97 g. The baseline TVA as shown in figure 3.3, can be noted to have a length of the cantilever beyond the tip mass. In order to determine correct length used in equation 3.1 the centroid is calculated and found to be at a point of 0.011 m, giving a length of 0.164 m from the base. The Young's modulus was taken to be $2.1\text{x}10^{11}$ Pascal's and the area moment of inertia taken from SolidWorks was taken to be $1.32\text{x}10^{-10}$ m^4. The remaining dimensions are given in the SolidWorks drawing shown in figure 3.4.

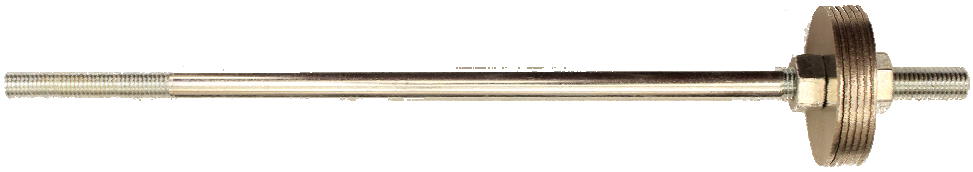

Figure 3.3: Constructed baseline TVA using washers to act as the tip mass.

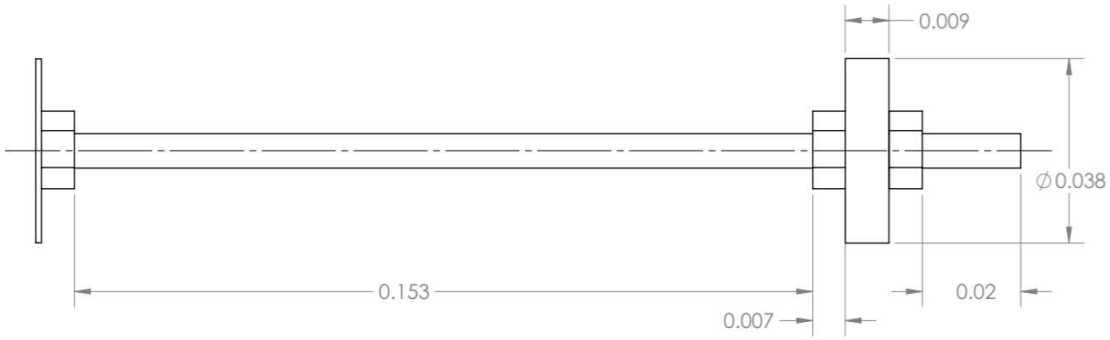

Figure 3.4: CAD model of the baseline TVA with dimensions in m.

3.2.1.2 *Passive-Adaptive TVA*

The second version of the TVA is that of the Passive-adaptive TVA (PATVA), the configuration starts with the baseline TVAs tip mass and incorporates the use of a riding mass to tune the TVAs frequency. From equation 3.1 the frequency of the cantilever with a tip mass is known, however, this will not work for the nonlinear TVA as there is also a riding mass with this configuration.

The cantilever will make use of a spring to allow movement of the riding mass, with the tip mass at the end. The tip mass will once again be configured through the use of washers, a total of 6 washers are used giving the same tip mass as was with the baseline TVA. The spring used is composed of music wire steel with a length of 2.5 inches and a stiffness of 10 lbs./in. At the base,

the spring is connected to a washer and on the other end the spring is connected to a bearing that houses the riding mass, as shown in figure 3.5.

Figure 3.5: PATVA riding mass installation.

The bearing used in the configuration is an ultra-low-friction oil-embedded sleeve bearing that slides along the cantilever. This bearing is slightly larger than the cantilevers diameter giving the ability to slide along the beam. However, the diameter of the sleeve is bigger than that of the cantilever so a layer of tape was used to give a more snug fit. While this may cause damping or friction, it will prevent the riding mass from oscillating in the y or z directions.

In order to keep a sense of symmetry and unity a second cantilever was attached at the other side of the base as in the baseline TVA. The same techniques of checking the torque of the bolts was maintained and the configuration of the PATVA is shown in figure 3.6. A second configuration was also manufactured, one where the riding mass is now attached towards the tip of the beam. The materials, springs, and the use of tape between the bearing and the cantilever all remained constant; the only difference was the location of the riding mass.

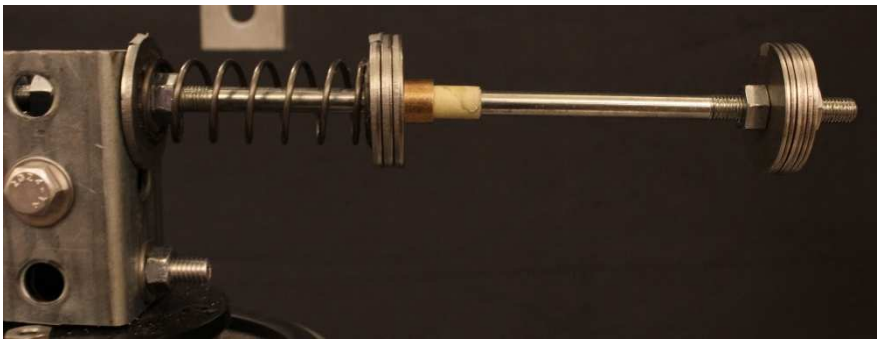

Figure 3.6: Base-attached PATVA configuration showing the riding mass configuration.

The idea behind the TVA is that it will utilize the abilities of the spring riding mass to increase the band gap and forms a vibration isolation within this frequency range. The concept of a meta-configured structure is brought into light again as the TVA focuses on the spring and riding mass to enhance attenuation of the vibrating structure. While the baseline TVA will vibrate on its own the riding mass will tune the band gap to a larger range of frequencies and will also be able to tune the frequency itself.

3.2.2 Test Cases

To avoid the undesirable effects of damping configurations of the TVA utilize passive-adaptive techniques such as the addition of the riding mass and a spring. In normal passive structures, frequencies are tuned to absorb the vibration of a single frequency and not tuned to encompass a range of frequencies. In response the ability to encompass a broader range of frequencies or shift the frequencies isolated by the vibration absorber. The study and the configurations of the TVA produce the ability to increase the bandwidth to encompass a broader range of frequencies by using the riding mass to attenuate the vibrations at the cantilevers tip. Figures 3.3-3.4 show the concepts of passive-adaptivity and the ability to utilize the riding mass to expand the bandwidth of interest.

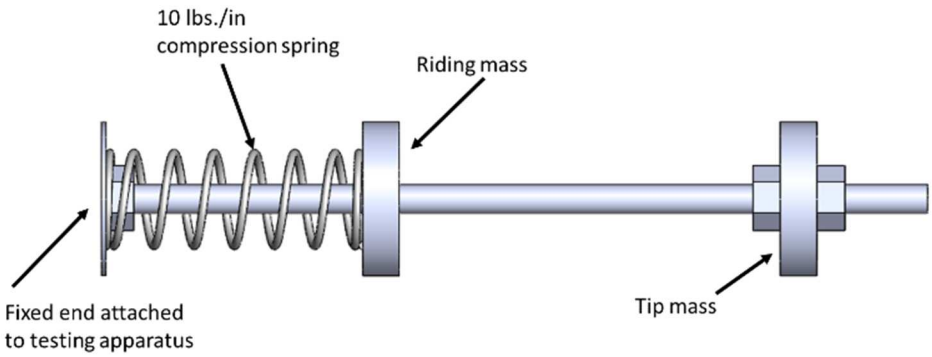

Figure 3.7: CAD modeled base-attached PATVA showing locations of the parts.

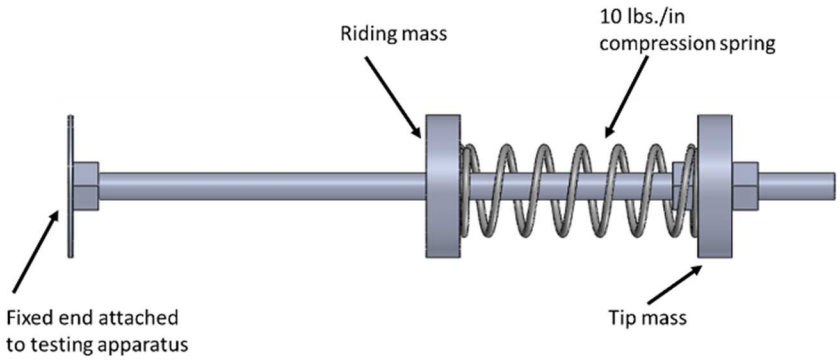

Figure 3.8: CAD model of tip-attached PATVA showing its components.

To test the different versions of the TVA than a more simple nomenclature was configured for the three different concepts. By using the three different configurations, it would allow a baseline to compare the base-attached and tip-attached cantilevers. Using the base-attached and tip-attached would give a more in depth study to determine if the TVA could be optimized and if the optimization of the cantilever would prove to be more tip biased or base biased. Additionally to understand the masses used on the TVA, it needs to be known that there are two types of washers used in the configurations. There are smaller washers at the tip and larger washers on the riding mass, the mass of one larger washer equals that of two smaller washers.

The first configuration is that of the baseline TVA shown in figures 3.3-3.4, this test will stand as a base for understanding the other two configurations. The baseline TVA will have 6 of

the smaller washers at the end, however, for simplicity the nomenclature will focus on the amount of larger washers in the system. Therefore, in the baseline case, there are 3 larger washers and so the test was labeled BL_3T0R where BL signifies which type of TVA, in this case baseline, T stands for the number of tip washers, and R stands for the number of riding washers. In this case, there are three tip washers with no riding washers.

The second configuration is that of the nonlinear configuration where there is both a riding mass and a tip mass. The first of the two nonlinear configuration is where the riding mass is attached to the base or the BA (base-attached). The second nonlinear configuration will be where the riding mass is attached to the tip or the TA (tip-attached).

Regarding the masses of the two configurations, there will be two separate cases tested, one where the mass remains constant with the baseline and the second where an additional mass is added. In the baseline there are 3 washers and so these washers will be shared between both the tip and the riding mass for the case where the mass remains the same. When the mass is varying there will always be three washers at the tip and the amount of washers for the riding mass starts with one and progresses towards three washers.

The nomenclature for the two cases starts with the varying masses and slowly progresses towards the constant mass cases. The initial test has three tip and one riding masses, it is labeled as PA_BA_3T1R, the second varying mass test is with three tip and two riding or PA_BA_3T2R. The last varying mass case was the where both the tip and the riding masses have three washers attached to each, labeled as PA_BA_3T3R. The cases where the mass remains constant is labeled as PA_BA_2T1R and PA_BA_1T2R, where T stands for tip and the R is the riding masses.

The second configuration uses the same cases that was previously seen with the base-attached riding mass, except this configuration will be attached at the tip. The nomenclature remains the same for T being tip and R being riding attached with the cases being: PA_TA_3T1R,

PA_TA_3T2R, PA_TA_3T3R for the varying mass cases and PA_TA_2T1R, PA_TA_1T2R for the constant mass cases. In total eleven different cases are studied with 3 different configurations as shown in table 3.2.

D_5^* *frequency bandwidth for the tip-attached test cases*					
Case #	D_5^* **(Left) lower bound (Hz)**	D_5^* **(Left) upper bound (Hz)**	D_5^* **(Right) lower bound (Hz)**	D_5^* **(Right) upper bound (Hz)**	D_5^* **bandwidth (Hz)**
PA_TA_3T1R	43	53	43	53	10
PA_TA_3T2R	41	52	41	52	11
PA_TA_3T3R	41	54	41	54	13
PA_TA_2T1R	48	62	48	62	14
PA_TA_1T2R	52	69	52	69	17

Table 3.2: Summary of tip-attached PATVA test cases

Each configuration shown in figures 3.7-3.8 will undergo several different tests, both experimental and simulations will be done with the different configurations. An initial simulation will be ran to understand the natural frequencies of the different TVAs and a simulation will be ran on the nonlinear TVA to understand what happens over a period of time. Experiments will also be ran on each of the different test cases to check and see what the actual natural frequencies of the different TVAs turn out to be.

3.2.3 Simulation Modeling

To effectively analyze the TVAs both numerical simulations and experimental testing using a modal shaker were simulated. The cantilevers were CAD modeled through SolidWorks and FEM studies were ran through Abaqus. As with the wave guide the material properties need to be specified and in this case low carbon steel is used with parameters of E, ρ, and ν, had to be specified or young's modulus ($200x10^9$ Pa), density (7850 kg/m^3), and poisons ratio (0.305) respectively. These values would remain constant through the varying simulations of the TVA, however, parameters such as the mesh sizing would need to be studied to understand the full effect of the

frequencies. The mesh would need a study to find what size of mesh the frequencies converge within 5%; table 3.3 shows the convergence of the mesh and figure 3.9 shows the finalized mesh size of 0.01 mm.

Mesh convergence study			
Mesh size (mm)	**Number of elements**	**Frequency (Hz)**	**% difference**
0.1	536	84.72	-
0.05	544	62.46	26.27
0.01	876	53.99	2.00
0.005	2131	53.80	0.35
0.004	3903	53.70	0.13

Table 3.3 FEM mesh convergence study for the TVAs simulation model

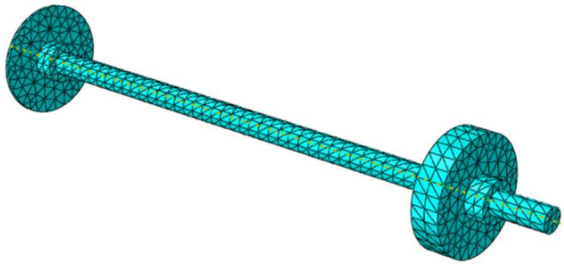

Figure 3.9: TVA finalized mesh obtained through Abaqus.

An initial simulation to understand where the natural frequencies occur at would be ran on each of the different TVAs, however, the assumption of small displacements is brought into play and the riding mass is assumed to be fixed. This will not give a complete validation as to where the frequencies of the different TVAs lie, however, it will give a rough estimate as to where they should be. To simulate the frequency response a modal analysis is configured to determine the first five to ten modes of the varying configurations. The first mode shape is the mode of interest, a cantilever is known to oscillate up and down (assume this as the y-axis). The mode shapes shown in figure 3.10 is known as mode shapes of a cantilever, the first mode is the natural frequency of the cantilever.

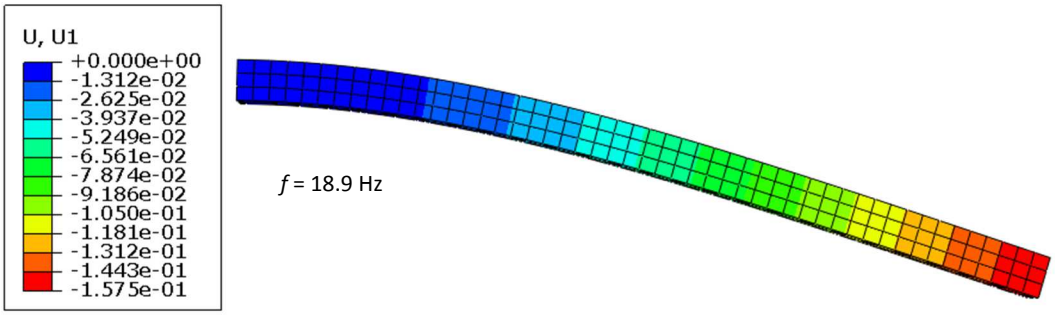

Figure 3.10: Cantilever first mode shape at 18.9 Hz from FEM.

Analyzing the found first mode frequency of a cantilever beam found through FEM modeling with that of the theoretical calculation [50], using equation 2.1 and where m_{eqv} utilizes equation 2.2, it can be noted that the calculated frequency is 20 Hz.

A second simulation would be entertained to understand the behavior of the cantilevers when under loaded conditions at or around the natural frequencies. In order to simulate the cantilever a steady state dynamic modal response is considered, this will take the frequency response of the system and take an input amplitude and excite the system until it reaches a steady state. This input amplitude once a steady state has been reached will give an idea as to the output natural frequency. This graph of this output frequency can then be taken and overlaid on the results found by the experiment to give a correlation between experimental and simulation results.

A third simulation would be taken into consideration to understand the behavior of the cantilevers when under loaded conditions at or around the natural frequencies. The simulation sounds like what was ran within the second simulation, however, this simulation would correlate more towards the actual results and take away several of the assumptions. The simulation would be changed by undoing the assumption of small displacements, springs would be added at the base and connected to the riding mass. By simulating, a test in which the riding mass moves with be more on scale as to what is seen by the TVAs in general and give an idea as to what magnitude of

movement will be experienced. This test will also give an idea as to what the actual natural frequency should coincide with.

3.3 Discussion of results

In this section an analysis of the FEM simulations, the frequency analysis results, and the summary of what happened when the riding mass was placed at different locations. The baseline was analyzed and compared with that of the nonlinear versions of the TVA to effectively understand and characterize the differences between configurations. The results will give an idea of what happens and if vibration isolation is seen or if the vibration isolation bandwidth is expanded.

3.3.1 Baseline TVA

A finite element analysis through the use of Abaqus was used to understand varying aspects of the baseline TVA. The baseline TVA is investigated to determine its modal frequencies, bandwidth of appreciable isolation, and transient characteristics. Once the baseline TVA is analyzed using simulations, the next step would be to obtain the actual response through use of experiments. After completion of the simulation and experimental testing the data can be reduced and compared to ascertain agreement between the two data sets.

An initial simulation was investigated to determine the natural frequency of the cantilever, to do so a modal analysis was configured and the first 5 modes of the cantilever were simulated. The cantilever arm's experience the same responses as the wave guide, when the cantilever reaches resonance the displacement reaches much higher values than that of other frequencies. Since the first mode shape of a cantilever with a fixed end is known the first mode shape of the baseline TVA shown in figure 3.11 can be compared as well. Since the cantilever's mode, shape is comparable with that of a longitudinal mode the first mode can be assumed also.

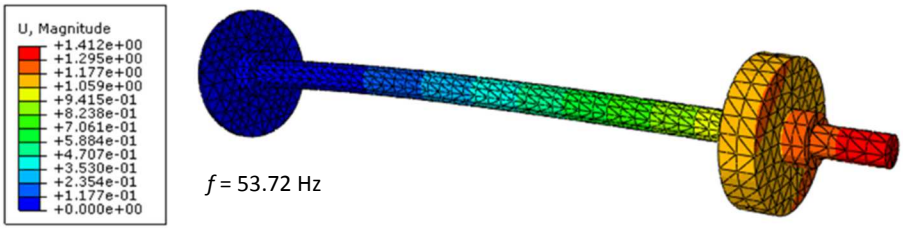

Figure 3.11: First mode shape of the Baseline TVA which is the first mode shape of a cantilever with a frequency of 53.72 Hz.

The TVA assumes a fixed end for the base, however, in the actual model the fixity isn't as rigid, instead the base of the actual TVA is connected to a beam which is more flexural. The cantilever is meshed, and a frequency response is simulated. For the baseline case a frequency of 53.72 Hz is found, this initial value will stand as a reference to determine if the frequencies of the other cases are at, above, or around the baseline case. A tradeoff study can be analyzed to determine if the bandwidth was able to be tuned and if so at what cost was it available.

A second simulation was simulated to determine what happens when the TVA reaches steady state, once as the TVA reaches steady state it will act as a vibration problem and no longer as a wave. To simulate this response a static perturbation is created and analyzed over a range of frequencies. Since the natural frequency of the baseline TVA is known from the first simulation so the range of interest can be assumed to reach from 10 Hz to 90 Hz since the natural frequency is well within this range. This data can be overlain with the experimental data to correlate between the two results. To check and make sure that the date is showing what is expected a much larger frequency range of up to 500 Hz is simulated to check and see if other frequency responses are simulated as well. A second frequency was found to be around 400 Hz and the steady analysis picked up this case, so a sense of validity is given.

The final analysis that was done regarding the baseline TVA is that of the experimental analysis, the TVA was configured and connected to a modal shaker as shown in figure 3.2. It is

seen that the system has dual arms instead of the single arm that is modeled through Abaqus, this is for symmetry purposes. The excitation is taken at the base of the apparatus and the input displacement is also measured at the base. The output is measured at both the left and right tip masses and the left and right riding masses. Once as the data is obtained the data can be normalized with the base value by taking the output over the input and graphed to see where the system response is.

The baseline TVA was given an initial displacement of $3x10^{-5}$ m measured at point 1 in figure 3.12, and the corresponding outputs were taken. The frequency response of the baseline TVA shows that the natural frequency lies around 51.5 Hz, and if the a normalized amplitude (D*) value is taken at 5 (D_5^*) the bandwidth of the baseline TVA comes to be a range of 11 Hz spanning from 48 to 59 Hz.

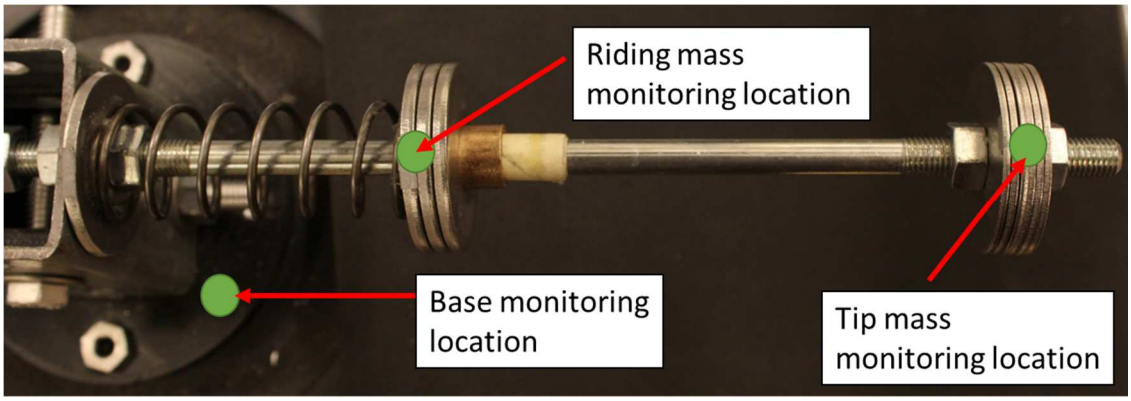

Figure 3.12: TVA vibration testing monitoring locations.

The data compiled for the baseline TVA will give an initial position to determine if a sense of validity for the hypothesis set forth. The theory behind the TVA is that the riding masses will be able to tune the bandwidth of the cantilevers through passive-adaptive means. This comes at a cost though so several means will be investigated to determine the strength and validity of the varying concepts. It is known that the baseline TVAs natural frequency is at roughly 51.5 Hz and that its bandwidth spans a range of 11 Hz, however, a bandwidth that can be increased is sought after.

3.3.2 Passive-Adaptive TVA

The passive-adaptive TVA or PATVA is a more complex article and so the system response will also be more complex. The PATVA is configured by attaching a spring with a riding mass to either the base or the tip; this will give a more broad range of possibilities to increase the bandwidth. For simplicity, notations were given for the tip-attached (TA) and the base-attached (BA) TVAs.

The TVA and the PATVA will both have a right cantilever and a left cantilever due to symmetry. Data for both of the cantilever arms are collected, however, for simplicity and a better understanding the right cantilever data was used and the data corresponding to the left cantilever is shown within the appendix B. The data within this section has been given a notation for the riding mass as RR or right riding and the RT for the tip mass or right tip, while the data within the appendix has been notated as LR for left riding and LT for the left tip mass.

3.3.2.1 Base-Attached TVA

The first configuration introduced shown in figure 3.7 was that of the BA configuration, the tests would be consist of the simulation modeling and the experimental results, in which the simulation modeling consisted of a frequency analysis and a steady state analysis. The first test that would need to be simulated was that of the frequency analysis where the first mode shape is sought after in order to find the natural frequency. Since the mode shape of a cantilever is known it is also possible to get an idea of the mode shape of the BA PATVA. The frequencies of the BA PATVA along with the test cases is shown within table 3.4, taking the normalized amplitude value D_5^* at a displacement of five and by taking the central input, normalizing it with the output displacements. Both the left and the right cantilever arms were monitored and data was captured at each monitoring location. It is possible that slight variations in the frequencies exist due to the difference in when the data is collected. To reduce the time variance the two cantilevers were monitored one after

another. Despite the differences in synchronized measurements, the left and right cantilever results matched closely so the left cantilever results are shown in appendix B.

D_5^* *frequency bandwidth for the base-attached test cases*					
Case #	D_5^* **(Left) lower bound (Hz)**	D_5^* **(Left) upper bound (Hz)**	D_5^* **(Right) lower bound (Hz)**	D_5^* **(Right) upper bound (Hz)**	D_5^* **bandwidth (Hz)**
PA_BA_3T1R	46	59	46	59	13
PA_BA_3T2R	43	58	43	58	15
PA_BA_3T3R	42	55	42	55	13
PA_BA_2T1R	54	68	54	68	14
PA_BA_1T2R	65	80	65	80	15

Table 3.4: Summary of base-attached TVA test cases

It can be noted that for the varying mass cases the frequencies remain close in proximity while the constant mass cases the resonance frequencies are much larger than the baseline, both of which can be understood with ease. For the varying mass cases when more mass is added the initial thought is that the frequency should be decreased, however, the added mass towards the base also gives a stiffening effect to the cantilever. It is also known from equation 3.1, that the length plays a role into the frequency of the cantilever due to the L^3 term within the denominator. This same phenomena extends into the constant mass cases as well, it is seen that when the tip mass is smaller the frequency is larger. Again, the riding mass, the tip mass, and the length comes into play in determining the natural frequencies of the cantilever. When the riding mass has a greater mass than the tip mass, the length will play a larger role in the frequency giving a greater stiffness and a higher frequency will be simulated. However, when there is more mass towards the tip the length and the mass of the tip play a greater role in its frequency, giving more mass rather than added stiffness resulting in a smaller frequency than that of the PA_BA_1T2R's frequency.

The second simulation was that of the steady state analysis, used to determine what would happen when the BA PATVA reaches a steady state and what would happen over a range of frequencies. The simulation in theory would experience a larger displacement at any of the

frequency modes, however, within the 100 Hz range there would only be the natural frequency since the next frequency of interest would happen at around 400 Hz. This data was imported into excel and saved for later use to compare with the experimental results.

The last set of testing that was simulated was that of the experimental results where an input excitation was input at the base of the cantilever over a range of frequencies to determine the output displacement. The output displacement was taken at the base, on the tip masses, and on the riding masses of both cantilever arms. By taking a measurement on both cantilever arms a sense of symmetry would be given and a determination as to if the cantilevers responses remained the same as they should. Due to small differences in lengths at some points the displacements of one cantilever is slightly larger by only a few microns, however, all of the frequencies that were tested approximately lined up with where simulations suggested they would be at.

The first case was that of the PA_BA_3T1R, as shown in figure 3.13, the first point of interest is that of the right riding displacement compared with the right tip displacements. It is seen that the paths of both locations have a similar path just at a varying magnitude, while there are some variations this is to be expected due to the nonlinearities of the cantilever. The second point is that of the bandwidth, taking a normalized displacement, D_5^*, it can be seen that on the lower end the bandwidth is expanded by 2 Hz, now ranging from 46 to 59 Hz with a bandwidth of 13 Hz. The third aspect seen is that on both the high and low ends the displacement trends to one. This is as theory would suggest, when the cantilever experiences both high and low frequencies the displacement should tend to the input amplitude, in this case that would be 1 since the data is normalized. The last point of interest is the natural frequency; simulations gave a frequency of 53.9 Hz, while the experiment gives a frequency of 52 Hz. The difference is that the simulation is assuming small displacements and so the effects given by the displacements aren't playing a role, however, the frequencies are close giving validity to what is being seen.

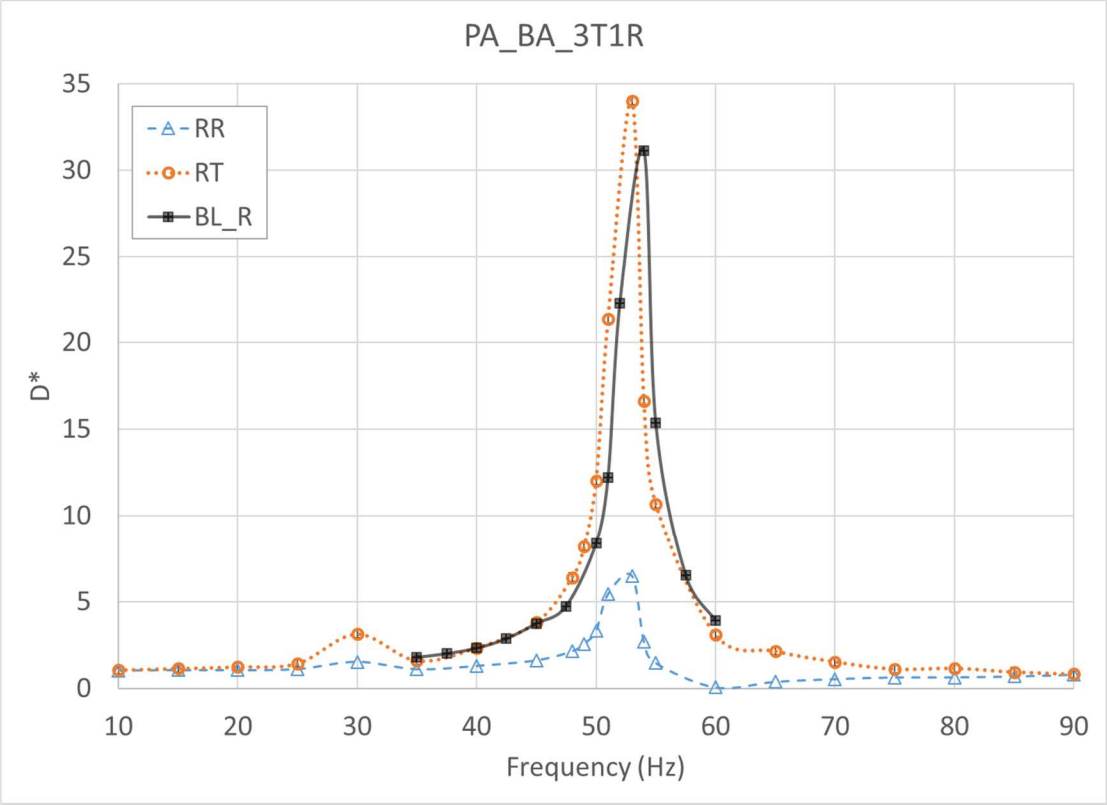

Figure 3.13: Normalized displacement transmissibility results for the passive-adaptive base-attached TVA with 3 tip and 1 riding masses.

The second case shown in figure 3.14 was that of the PA_BA_3T2R, the simulations suggested that the frequency should lie around 54 Hz and the experiments had it at 52 Hz. Once again, the simulations make an assumption of a small displacement, while the actual experiment gives a closer representation as to where the frequency lies. Despite the assumptions made there is a correlation between the results being within close proximity. The other phenomena experienced by the BA PATVA is that of the bandwidth, when D_5^* is used the bandwidth extends to encompass from 43 to 58 Hz. By losing a small bit of the frequency range on the upper end the BA TVA is able to increase the bandwidth on the lower frequency range by 5 Hz when compared with the baseline TVA, this gives a bandwidth of 15 Hz. The other phenomena that is experienced by the PA_BA_3T1R regarding the magnitudes and outside the frequencies of interest tending to one is also seen within the PA_BA_3T2R case.

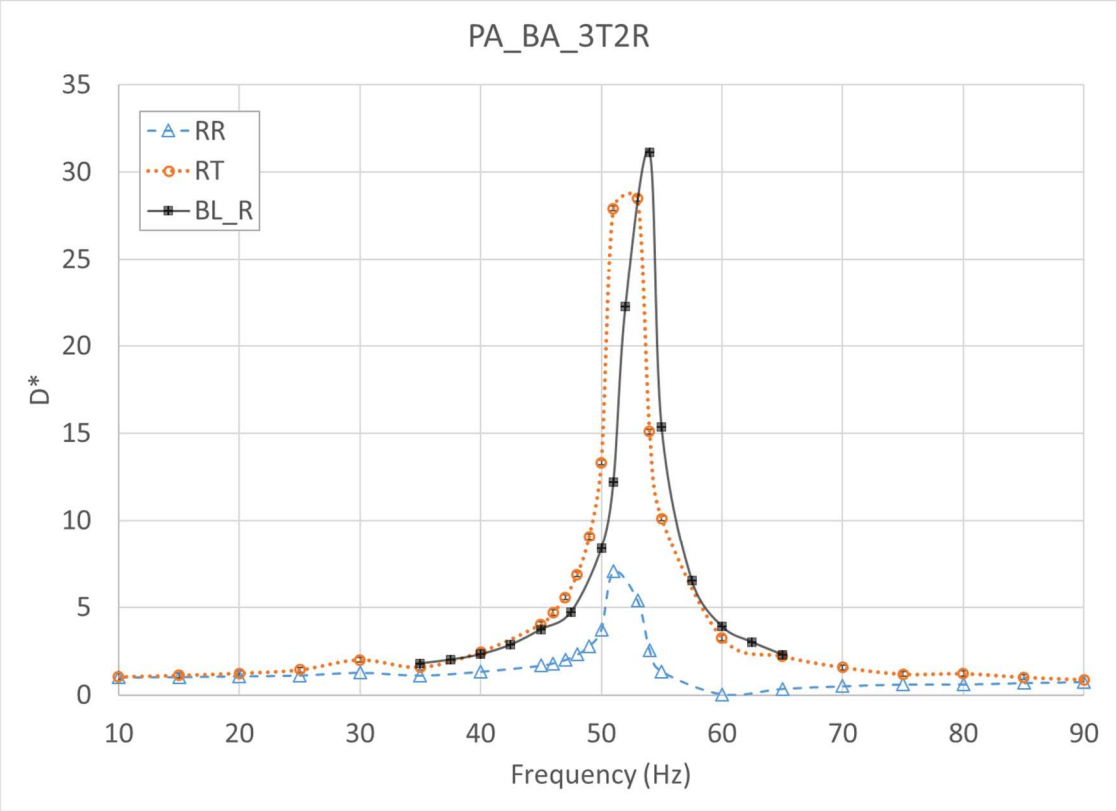

Figure 3.14: Normalized displacement transmissibility results for the passive-adaptive base-attached TVA with 3 tip and 2 riding masses.

The last of the base-attached varying mass cases is that of the PA_BA_3T3R shown in figure 3.15. Compared to the baseline TVA the frequency of the PA_BA_3T3R case is lower with a natural frequency of 49 Hz, however, the simulation gave a frequency of around 54.3 Hz. Comparing the two results, the conclusion is reached that even though the simulation gives a good estimate as to where the frequency lies the displacement will still play a role in determining the frequencies of interest. Analyzing the PATVAs bandwidth shows that the frequency range shifts down a bit and at the same time the bandwidth is decreased by 1 Hz, giving a range of 42 to 55 Hz.

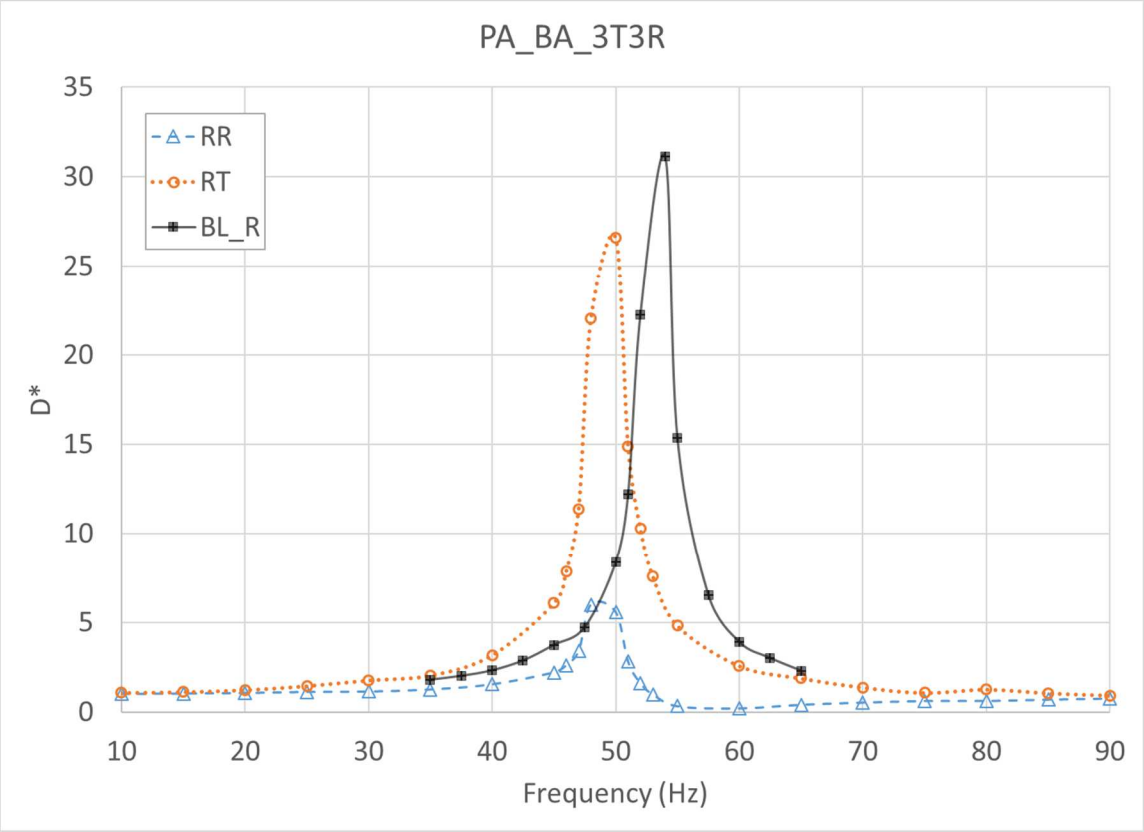

Figure 3.15: Normalized displacement transmissibility results for the passive-adaptive base-attached TVA with 3 tip and 3 riding masses.

For the BA PATVA where the mass is varying between both the simulations and the experiments there seems to be a close correlation, however, there are the difference due to the riding mass having small displacements assumption. Other points of validity regarding the change in the bandwidth is that of the displacements trending to one and the paths of displacement for the varying cases sharing the same path just scaled. However, the largest takeaway is that if the bandwidth, while all three cases see an increase in the bandwidth the most prominent case is that of the PA_BA_3T2R, where the bandwidth is increased from 11 Hz to 15 Hz.

The second BA PATVA configuration is that where the total mass shared between the riding mass and tip mass remains constant with the baseline TVAs mass. The first constant mass case is the PA_BA_2T1R shown in figure 3.16, the data shows that the natural frequency is at 60

Hz, however, the simulations say that the frequency should be at 61.5 Hz which is a close correlation to the experiments. At the same time when analyzing the data, it can be seen that the paths do not match up, the right riding shows no specific peak. This can be explained though since the mass of the cantilever is more uniquely distributed, so the magnitude of the displacement is also less than that of the baseline. The last point of interest for the case is the bandwidth, since the frequency has been shifted upwards than it makes sense that the bandwidth also moves upwards. The baseline TVA gave a range of 48 to 59 Hz while it is seen in the PA_BA_2T1R's case that the bandwidth is ranging from 54 to 68 Hz with a bandwidth of 14 Hz, which is larger than the baseline.

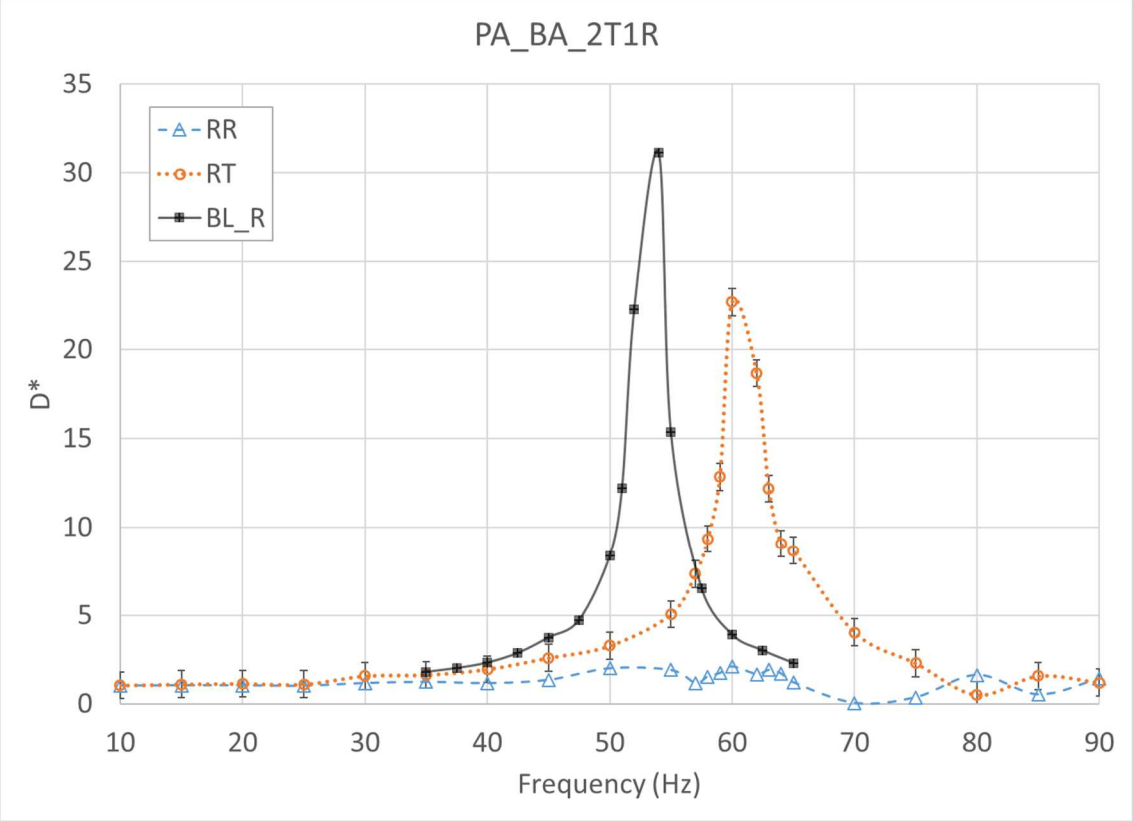

Figure 3.16: Normalized displacement transmissibility results for the passive-adaptive base-attached TVA with 2 tip and 1 riding masses.

The final BA PATVA configuration is that of the PA_BA_1T2R, the data shown in figure 3.17 says many of the same concepts that the PA_BA_2T1R showed. The same level of difference

with the paths are seen with the right riding data not being as well defined as the right tip displacement path. Upon looking at the simulation data's natural frequency it is seen to be at 72.85 Hz, and the experimental natural frequency is seen to be at 72.5 Hz. The two frequencies being higher than that of the baseline makes sense since there is less mass and a greater stiffness overall. Since the natural frequency is at a higher range than the bandwidth will also be around this range also. The bandwidth shifts from the baseline case of 48 to 59 Hz to the PA_BA_2T1R ranging from 65 to 80 Hz, with a bandwidth of 15 Hz.

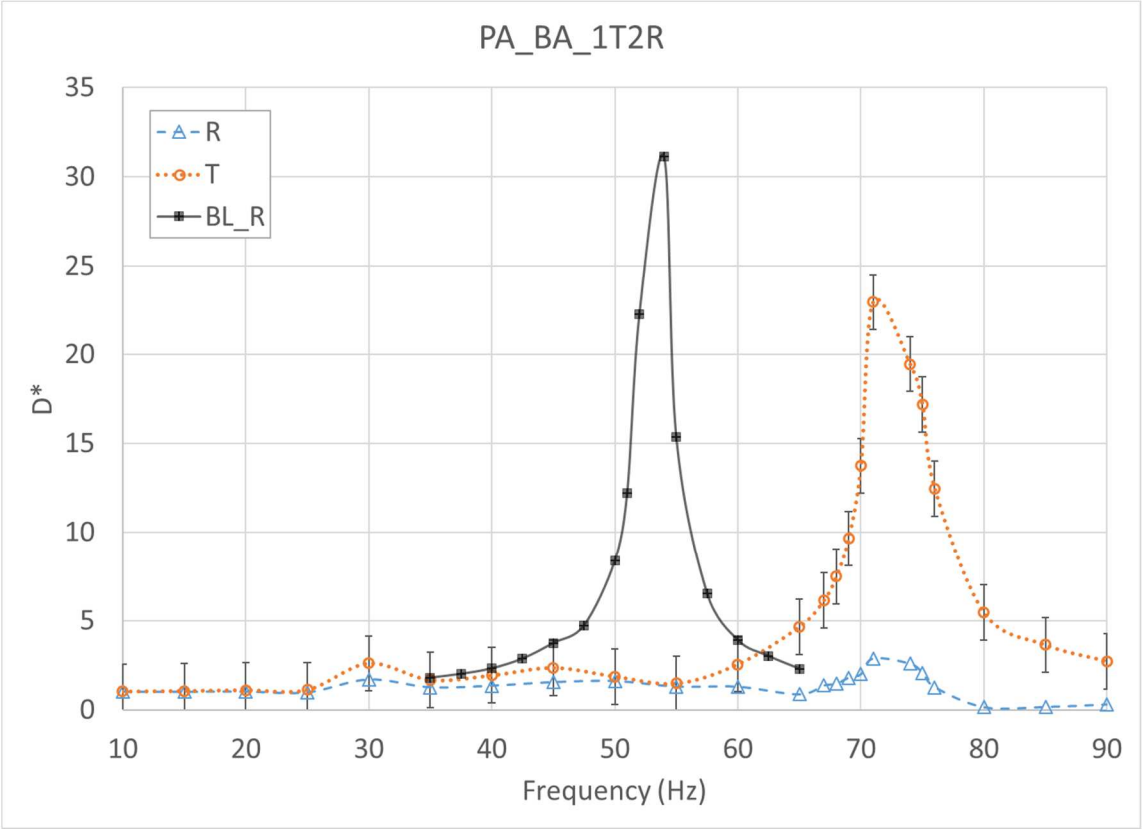

Figure 3.17: Normalized displacement transmissibility results for the passive-adaptive base-attached TVA with 1 tip and 2 riding masses.

For the BA PATVA configuration it is seen that the frequencies of the varying mass cases are around the baseline's natural frequency, however, the bandwidth remains around the same range. For the case where the mass remains constant, the frequencies are shifted upwards; however,

the bandwidth range is also increased by this effect. So, for the BA PATVA it can be said that there is a trade-off between the two, while the varying mass cases remain around the baseline frequency the bandwidth doesn't see much benefit. However, by keeping a constant mass and shifting the mass to a different area, the bandwidth is able to increase, but the frequencies also increase. In both cases the initial question is solved, however, a tradeoff is given and the solution to which is better is in question.

3.3.2.2 *Tip-Attached TVA*

The second PATVA configuration introduced shown in figure 3.8, is that of the TA configuration. The thought is that by changing the location of the riding mass there is a possibility that the bandwidth can be further increased. The same simulations that were ran on the baseline TVA and the BA PATVA using Abaqus were simulated on the TA PATVA also. The first of which being that of the frequencies that have been compiled and compared between the simulations and experiments which are shown in table 3.2.

The frequencies note that for the varying mass cases the frequencies are reduced more than that of the baseline TVA. This makes sense since the frequency depends on both the mass and the L^3 components of the TA PATVA, with a smaller length but larger mass the frequency will also decrease. With the constant mass cases of the TA PATVA the frequencies are increased by a small amount due to a decrease in mass coupled with a greater stiffness than the baseline TVA. A steady state analysis was simulated on each of the TA PATVAs cases giving an idea of the response over a range of frequencies.

As with the BA PATVA configuration the experimental results of the TA PATVA were tested by taking the output displacement and normalizing the data with the input. The same key points were also used with the input being at the base and the output being at the riding mass and tip mass of both cantilever arms. Both sets of data for the left cantilever and right cantilever arms

matched within a certain degree, however, differences can be explained by inability to completely match the lengths and mass of the cantilevers. Despite the minor differences the natural frequencies align, but the magnitudes do not, giving an idea that the mass plays a larger role than the lengths.

The first case of the TA PATVA was that of the PA_TA_3T1R, the data seen in figure 3.18 gives several ideas as to what is being seen. The first of which is the natural frequency, which the experiments show being 52.8 Hz and the experiments give a frequency of 48 Hz. Similar to the BA PATVA it can be seen that the small displacements assumption also plays a role in the TA PATVA. The second aspect is that of the displacement's magnitudes, the RR displacement is larger than that of the BA PATVA cases. On the other hand, the paths of both the RR and RT show a relationship with the RR having a smaller magnitude. The last aspect is that of the bandwidth, as in previous a D_5^* is used and compared with the baseline TVAs bandwidth. The bandwidth of the baseline TVA ranged from 48 to 59 Hz, but with the PA_TA_3T1R the bandwidth ranges from 43 to 53 Hz and a bandwidth of only 10 Hz. Comparing the bandwidth of the PA_TA_3T1R and the PA_BA_3T1R it can be seen that at the higher frequency of the BA case gives a larger bandwidth than the TA case.

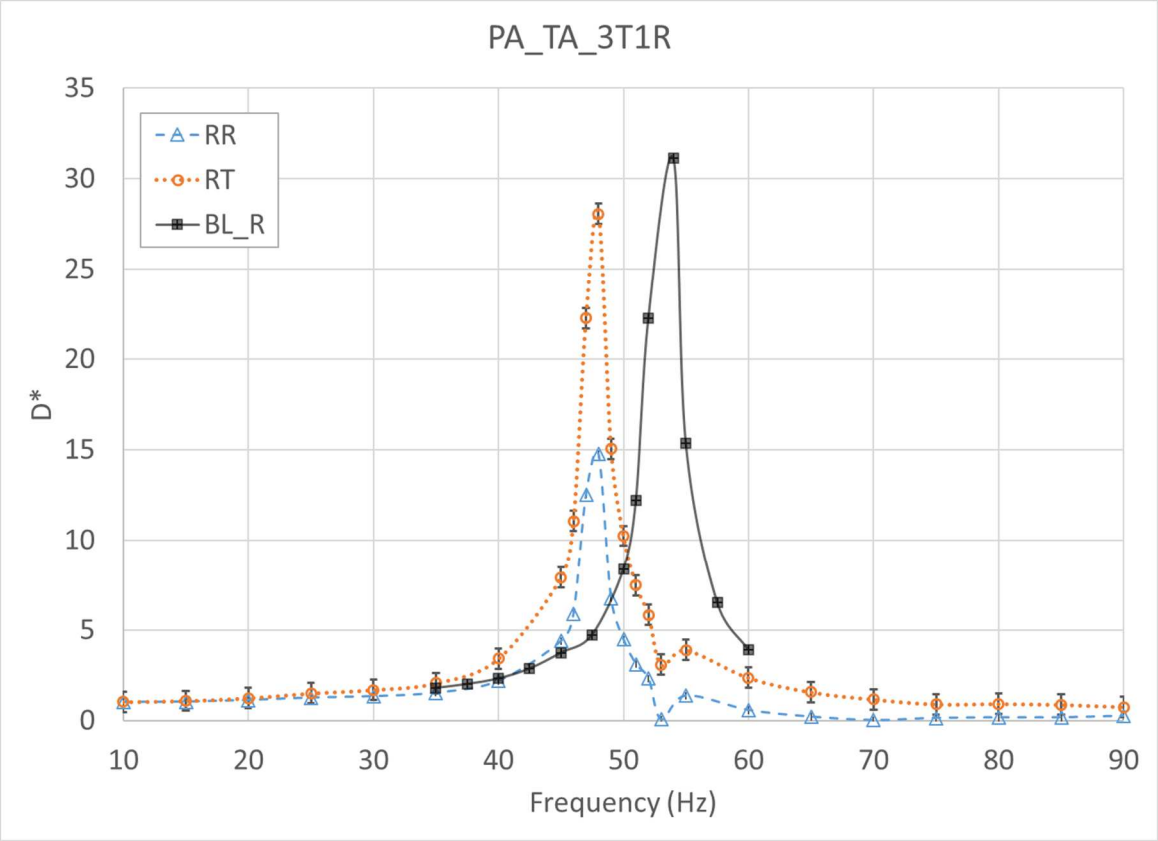

Figure 3.18: Normalized displacement transmissibility results for the passive-adaptive tip-attached TVA with 3 tip and 1 riding masses.

The second case of the TA PATVA shown in figure 3.19, was the PA_TA_3T2R, in which is seen that the frequency remains close to what is seen in the previous TA PATVA. The frequency of interest for the simulations is at 52.1 Hz while the experimental frequency is at 48 Hz. When comparing the bandwidth with the baseline the TA case shows a frequency ranging from 41 to 52 Hz giving a bandwidth of 11 Hz. This shows that as seen in the previous case the bandwidth of the TA varying mass shows little to no effect on increasing the bandwidth.

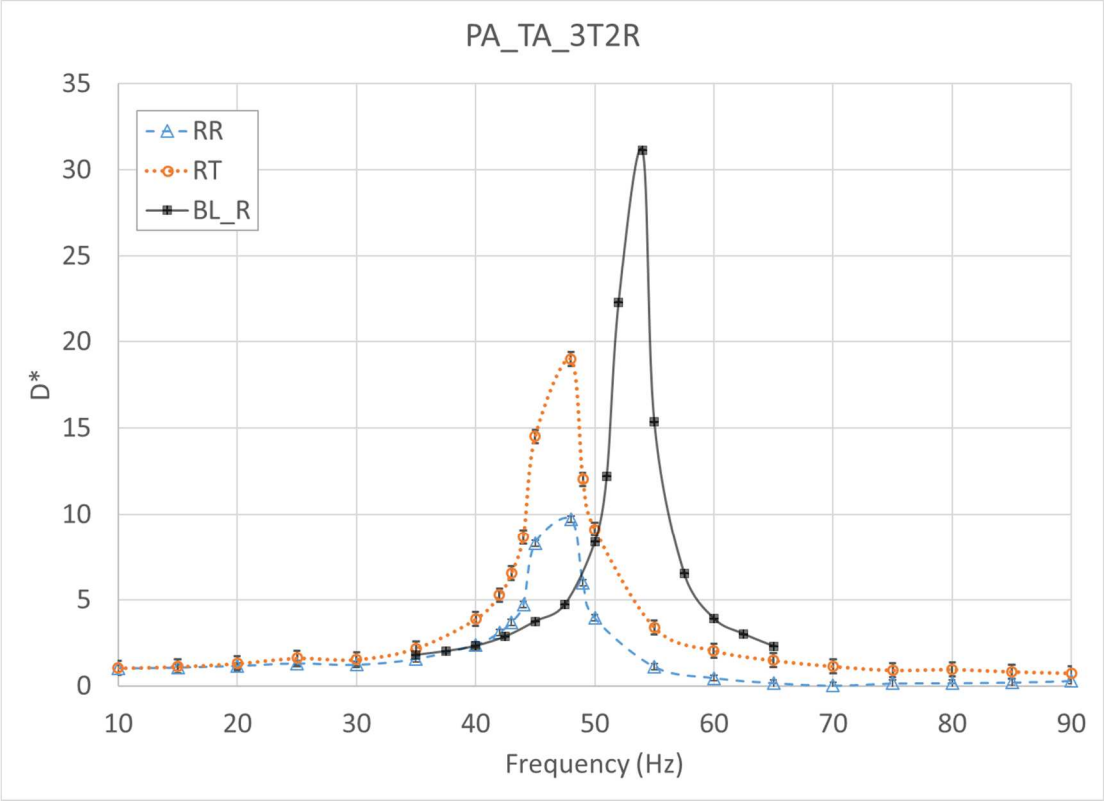

Figure 3.19: Normalized displacement transmissibility results for the passive-adaptive tip-attached TVA with 3 tip and 2 riding masses.

The remaining TA PATVA varying mass case shown in figure 3.20, was that of the PA_TA_3T3R and as with the other TA varying mass cases the frequency remained close to that of the previous cases. The simulation places the frequency to be at 54.25 Hz, and when analyzing the experiment under a given displacement it was shown to be at 49 Hz. The second aspect of the TA case is that of the bandwidth, it can be seen that it now increases from 41 to 54 Hz, giving a range of 13 Hz.

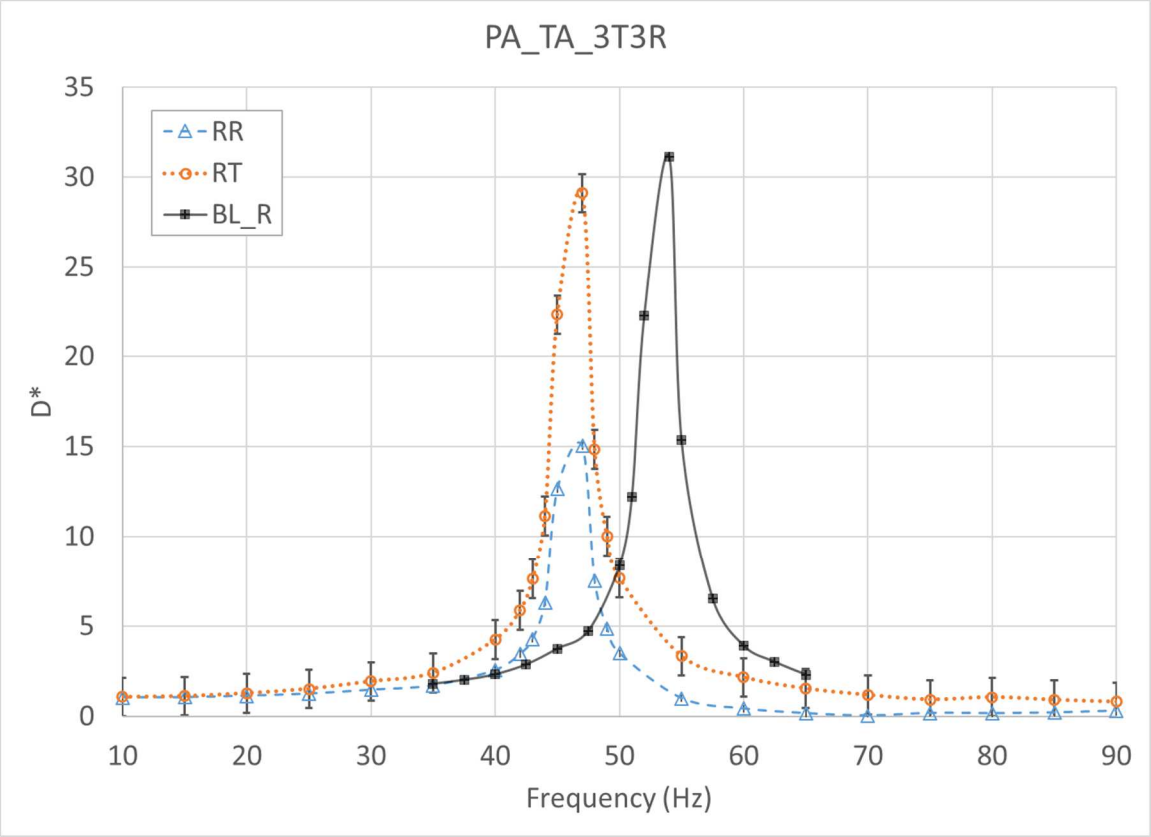

Figure 3.20: Normalized displacement transmissibility results for the passive-adaptive tip-attached TVA with 3 tip and 3 riding masses.

From the varying mass cases where the mass was consistently increasing with the more mass that was added. The original bandwidth of the baseline TVA was from 48 to 59 Hz and with the tip-attached simulations it is seen that the frequency is moved to 41 to 54 Hz at the cost of adding weight to the structure. The only problem with this is that the upper end of the bandwidth is sacrificed in order to increase the bandwidth altogether.

The second configuration is that of the tip-attached constant mass case where the mass of the tip and the riding mass are equal to that of the baseline TVAs tip mass. Despite the obvious differences there should still be a bandwidth that covers a varying range of frequencies. Outside of the baseline case there are only two possible combinations that give both a tip and a riding mass.

The first case of the constant mass is the PA_TA_2T1R, it can be seen from figure 3.21 that the frequency increases to 60 Hz with the small displacements assumption and the experiments give a frequency of 54 Hz. This change in frequency can be explained by the inability of the TA PATVAs riding mass, giving an idea that for this case the riding mass plays more of an effect than in other cases. The second point of interest is the bandwidth, since the natural frequency has increased it is assumed that the bandwidth will also be increased around this range. The original bandwidth was ranging from 48 to 59 Hz and when D_5^* is used, it shows the new bandwidth to be from 48 to 62 Hz with a bandwidth range of 14 Hz. This bandwidth gives an increased bandwidth while maintaining the original frequency range as well.

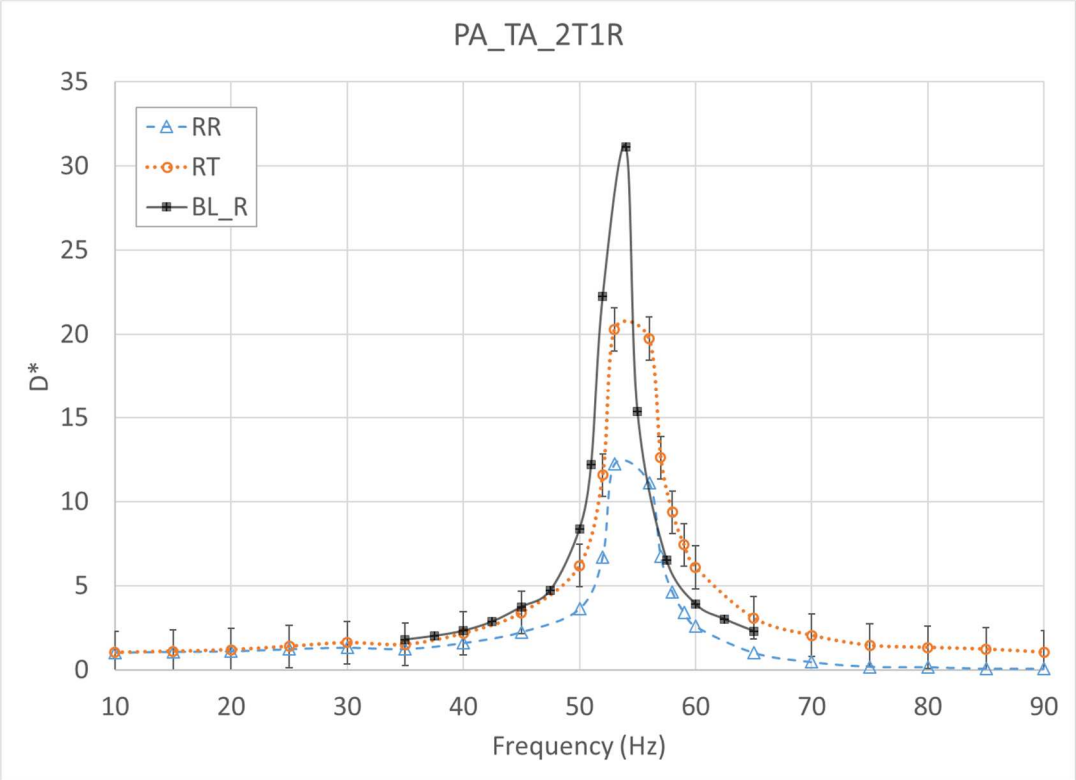

Figure 3.21: Normalized displacement transmissibility results for the passive-adaptive tip-attached TVA with 2 tip and 1 riding masses.

The final case for the TA PATVA was that of the PA_TA_1T2R shown in figure 3.22, as with the previous case it is seen that the frequency increases as seen in the afore mentioned case.

The simulations place the natural frequency to be at 68.6 Hz with the experimental frequency to be at 60 Hz. As with the previous case it is seen that the small displacement assumption plays a larger role in determining what the natural frequency will be. It is also seen that the bandwidth of the final case is increased, extending from 52 to 69 Hz and a bandwidth of 17 Hz.

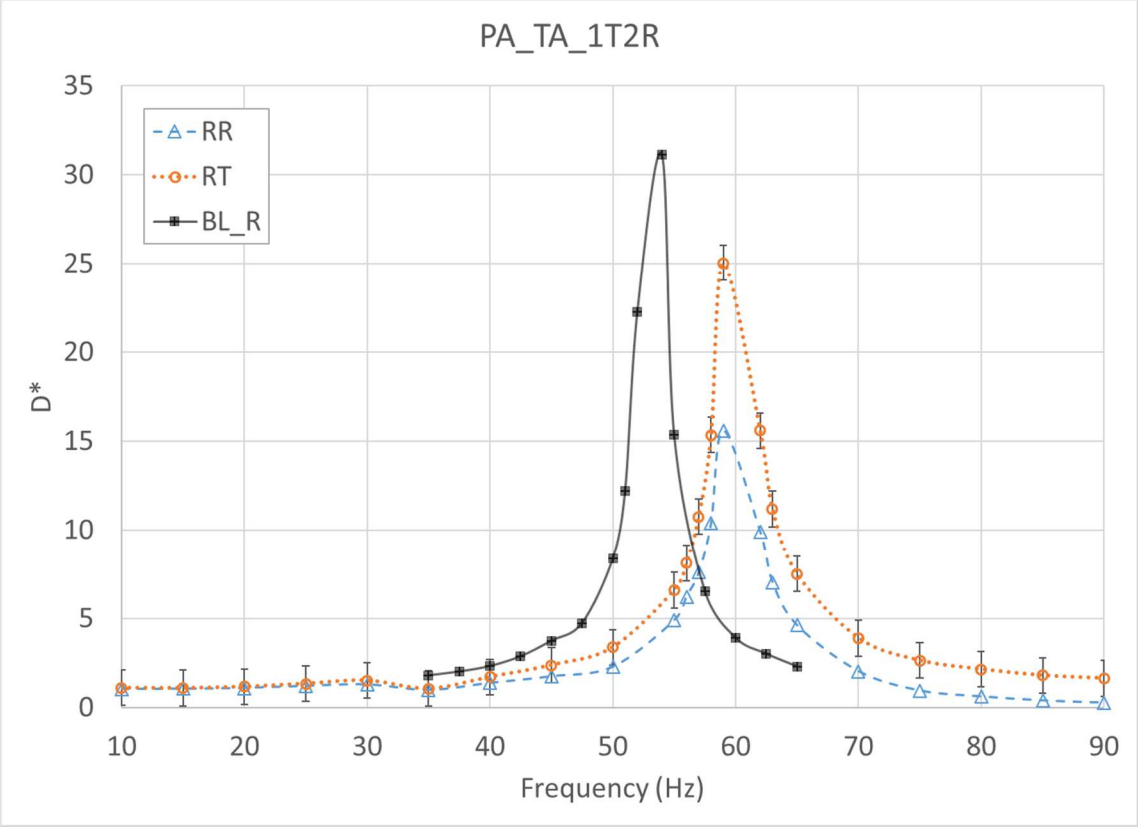

Figure 3.22: Normalized displacement transmissibility results for the passive-adaptive tip-attached TVA with 1 tip and 2 riding masses.

The results were compiled showing the different cases into a bar chart shown in figure 3.23. The data gives an idea as to which cases see the most or least amount of change in the bandwidth. For both the BA and TA cases of the varying masses the D_5^* values of the different cases show an increase in the bandwidth, however, the base-attached shows more prominence. For the BA cases, the bandwidths range from 13 to 15 Hz with the PA_BA_3T2R case gives the best results

with a 15 Hz bandwidth. The TA varying mass case bandwidth's range from 10 to 13 Hz showing less prominence than the BA case for the varying mass cases.

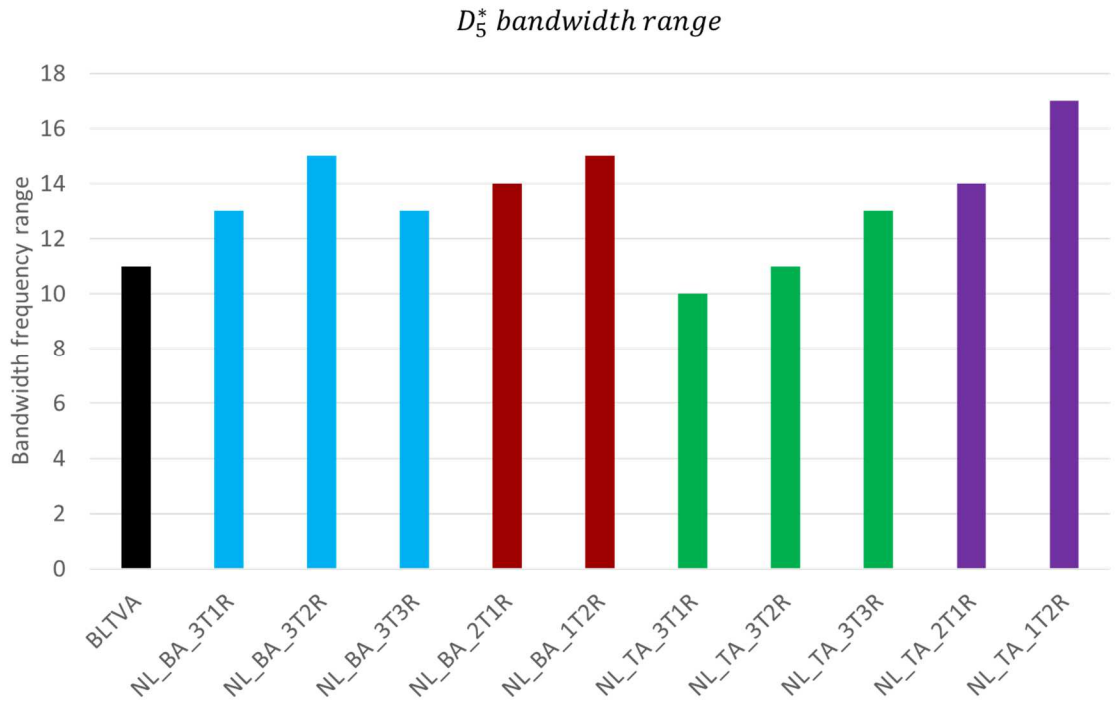

Figure 3.23: D_5^* bandwidths of the different TVA cases.

Looking into the constant mass cases, both of the BA and TA show a more prominent bandwidth expansion, however, the TA is greater than that of the BA cases. For the TA cases it is seen that the bandwidths are 14 and 17 Hz, while the BA cases the bandwidths are 14 and 15 Hz. Overall, the bandwidth of the PA_TA_1T2R shows the most bandwidth expansion with a range of 17 Hz compared to the baseline bandwidth of 11 Hz. This gives an idea that while the bandwidth increases for both the varying mass and constant mass cases the most prominent is that of the constant mass TA case. However, at the same time the TA case shows a smaller bandwidth with the varying mass cases.

A second bar chart was configured shown in figure 3.24, explaining where the bandwidths of the TA and BA configurations lie with respect to that of the baseline case. The chart gives several

insights as to what is going on in each of the different cases. The first point that is drawn is that all of the varying mass cases remain around the lower bounds of the baseline's bandwidth. In many of the cases the upper bounds of the bandwidth is sacrificed in order to achieve the more desired tunable bandwidth. However, in the case of the PA_BA_3T1R it is seen that the baseline's complete bandwidth is within the PA_BA_3T1R case.

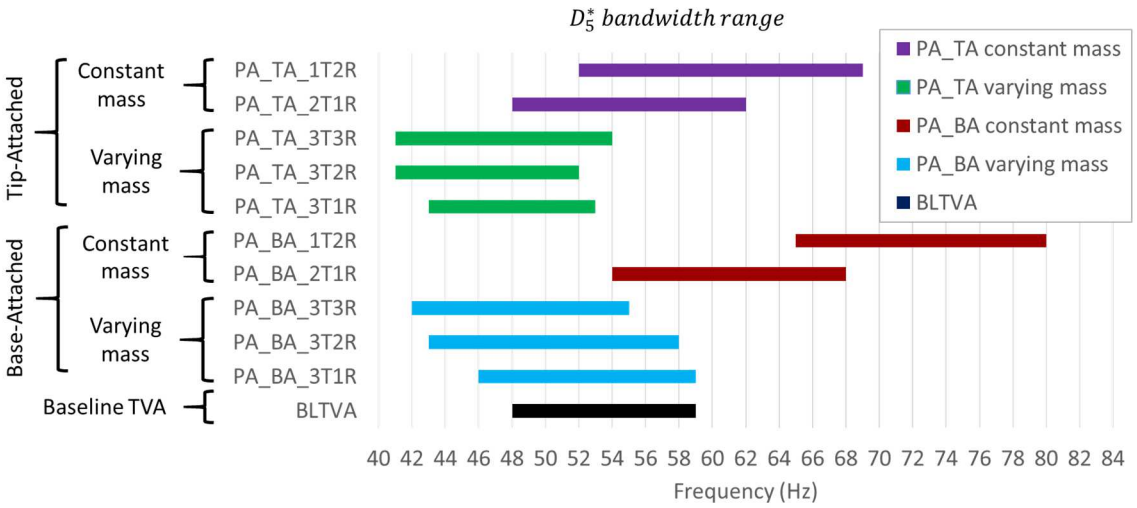

Figure 3.24: D_5^* bandwidths of the different TVA cases compared to the Baseline TVA.

For the constant mass cases it is shown that the frequencies are increased while also increasing the bandwidth. There is one case that stands out though, the PA_TA_2T1R band with encompasses the complete bandwidth of the baseline TVA while also expanding it to 14 Hz as well. This gives several conclusions for the TVA configurations, and an idea of how the subsystem interacts with the main system to tune the bandwidth.

3.4 Summary

In summary the TVAs show that by adding mass the bandwidth is increased, however, at the same time more mass in aero systems has to have a reason and here the added mass outweighs the slight bandwidth increase. The second synopsis is that for the constant mass the weight remains the same while increasing the bandwidth, but at the same time the lower bandwidth is sacrificed.

The third phenomena understood is that the bandwidth is able to keep its frequency range and increase it by either redistributing the mass or adding a slight mass. The study also shows that by adding the effects of the riding mass the subsystem can be effectively used to increase the frequency range of the bandwidth. Overall, the more desirable case is where the bandwidth is expanded the most while keeping the mass constant.

CHAPTER IV

CONCLUSIONS AND RECCOMMENDATIONS

4.1 Summary and Conclusions

The concept of meta-configured structures is a unique idea in which one could say that the synergistic integration of materials and/or structures via innovative configurations result in coactive mechanisms that deliver performance that exceeds what can be achieved using conventional approaches. This study considers two prototypical meta-configured structures – the directional wave guide (DWG) and the passive-adaptive tuned vibration absorber (PATVA). The first example is that of the directional wave guide through its innate ability engineered through meta-configuration to make an input excitation frequency and direct it in such a way that attenuation is seen in every which way except in a single designated direction. It is seen that the meta-configured structures can improve overall mechanical wave manipulation or vibration performance within structures through utilization of constituent subsystem's ability to enhance coactive mechanisms.

Using the band gap behavior displayed by acoustic metamaterials, a plate-type directional wave guide was designed and fabricated. This wave guide consists of a patterned array of cantilever beam-type resonators chemically etched into a 50-micron thick brass sheet. The relative band structure for the five different types of resonator in the DWG were designed such that frequency components within successive bandwidths within the 16-20 kHz range can selectively propagate along designated paths in the in-plane axially directions. Outside of these paths, in the 'quadrant' regions, the band gap exists for the entire frequency range of interest and hence none of the

frequency components propagate. Finite element analysis was done to ascertain the resonators' natural frequencies and the location and extent of their corresponding band gaps. A customized experimental rig consisting of a low-stiffness boundary fixture, piezo-actuator, and a mechanically-staged overhead laser vibrometer was set up for the dynamic characterization of the DWG test article. The experimental results indicate that the frequency component corresponding to the band gap associated with the missing resonator along each designated path tends to propagate the most, however due to potential interaction with higher global modes and variabilities in the resonator frequencies and boundary conditions some discrepancies in correlation with theory were observed. Overall, the potential to selectively beam specific frequency components along designed paths with a wave guide using meta-configurations originating from patterned arrays of resonating sub-structures was demonstrated experimentally.

A passive-adaptive tuned vibration absorber (PATVA) that incorporates a meta-configuration-based design approach was also dynamically characterized. In contrast to a conventional (passive) TVA that provides vibration isolation within a preset frequency bandwidth, the passive-adaptive TVA would be able to deliver appreciable isolation within an enhanced bandwidth through 'self-tuning' based solely on the input excitation. An approach based on a riding mass retained under spring force and free to traverse along a tip-loaded cantilever beam was used to realize the prototypical test article for the PATVA. Two different riding mass attachment configurations – base and tip attached PATVA with multiple mass distribution cases. Finite element simulations were performed on the mass-equivalent conventional (baseline) TVA and fixed mass approximations for the PATVA. Experiments were conducted using an electrodynamic shaker with a pair of symmetrically positioned test articles mounted using a custom fixture. The tip and riding mass responses were recorded using a laser vibrometer (a few were also recorded using a high-speed camera) with harmonic base excitation under steady-state conditions. It is found that up to 55 % increase in the bandwidth of vibration isolation could be obtained for the PATVA without

compromising the lower bound of the bandwidth or significantly increasing the overall mass in comparison to the conventional (baseline) TVA. This portends well for applications such as in aerospace vehicles where weight is a primary concern.

In summary, proof-of-concept demonstrations were accomplished for two prototypical meta-configured structures that indicate that meta-configuration as a design approach could offer potential solutions enhancements for dynamic load manipulation or mitigation. Potential applications include isolation of sensitive payloads in aerospace vehicles from structure-borne vibrations, transduction of narrow banded mechanical signals that have close spectral proximity to noise components, reduction of structural vibrations arising from sources such as propellers or rotary machinery that have a narrow banded dominant frequency content that can meander with settings during different flight regimes.

4.2 Recommendations for Future Research

AM's have been researched over the past series of years and in turn have grown into a vast area of interest and has gained support from both industry and government entities. However the concept of a meta-configured structure is an emerging idea that gives the capability to enhance both functionality and performance of structures. Noting the uniqueness of the configurations and ideas behind the study the lessons learned from the research will give ample ideas on how to further expand the concepts developed.

4.2.1 Wave Guide

The wave guide showed potential with the ability to direct frequencies and the capabilities of the sub systems to enhance the functionality. The following avenues are areas in which future research should be able to further benefit the ideas and concept set forward by the current research.

1) **New Microstructure Design:** AM's have been used rigorously to investigate the microstructures and MEMS scale designs set forward by different researchers. The study of microstructures gives a more advanced approach to the ideas and concepts set forward. By scaling down the articles and resonators the mass is decreased while keeping the same enhanced capabilities. For areas such as the aerospace industry this effect is more desirable since every gram of mass must be accounted for in some unique capability. In previous the MEMS scale articles have been used to investigate the terahertz (THz) frequencies [68]. However, the MEMS are not limited to THz frequencies, but they also expand to electromagnetic responses, in which there is an ability to tune the "meta-lattice structures" to control electromagnetic metamaterials.

2) **Symmetric Wavelength:** The wave guides design was initially designed to have a symmetric nature about the x-axis and y-axis, however, this doesn't account for the diagonal axis. The wavelength of the diagonal is larger in respect to the prime axis, this means that the wave speed will be different. This poses nonlinearities within the wave guide leading to reflections and undesirable phenomena. So in order to counteract the phenomena the idea of a circular plate is considered, this allows for all of the axis to remain symmetric and maintain the same wave speeds. This allows for the concept of energy harvesting to come into play and maintain the ability of the meta-configured multi-functionality.

3) **Manufacturing and Material Enhancements:** Within the wave guide the matter of manufacturing arose and the inability to do so effectively. One process that may be of some use to this concept is additive manufacturing [69], this makes an ability to manufacture small details with high accuracy. It also allows for the decoupling of mass density and the elastic properties offering additional flexibility in design. This also allows the unique designs utilized by the wave guide to be manufactured more readily.

However, a more feasible method of manufacturing or printing may need to be found in order to experience the phenomena more effectively.

4) **Numerical and Analytical studies:** While there were numerical studies ran on the wave guide there is an ability to further refine the assumptions through a study of 1D resonator units. There is also an ability to further the work done through the dynamic implicit analysis to understand the variations between the frequencies and refine the frequencies into smaller increments. There is an ability to further understand the models and the wave guide by creating an analytical model that effectively summarizes the wave propagation and modal interactions experienced by the varying resonator units.

4.2.2 Tuned Vibration Absorbers

The TVA has shown that there is an ability to tune the bandwidth of the structure, however, it has also shown that there is a large area of unknowns. The sub systems once again shows the ability for multi-functionality and at the same time an increase in the isolation of vibrations. The following areas of interest have been presented in order to further understand the capabilities of the TVA.

1) **Specialized Manufacturing:** A more modified version of the PATVA would benefit by the ability to have a more unique fit. One area being of the riding mass, in the study tape was used to give the ability to only move in the longitudinal axis. While there is fluctuation in the remaining axis, the desired effect is seen mostly within the longitudinal axis. A more specialized bearing would need to be manufactured and incorporated in the future endeavors. Another concept is a more constant mass, while the washers give the desired ability the use of a more constant mass would help control the deviation between the two cantilever arms.

2) **Material Study:** While the current materials give a good representation as to what is most readily used in industry there is still the ability to replicate the concepts in other materials. One idea is to look into a more elastic material, this gives a less rigid effect and possibly further enhances the bandwidth. Other options within the material study that may be able to change include the springs, the ability to have a less stiff spring should give the ability to obtain a more tunable bandwidth. One option is to increase or decrease the length of the spring to determine the new bandwidth of the structure. It was shown that when the riding mass was closer to the tip mass the bandwidth was increased as well. Another option is to further expand the amount of riding masses, however, the concept of keeping the same mass should also be considered.

3) **Numerical and Analytical Study:** While there were numerical studies ran a further understanding of the ones that were made and how to expand on those by using a model that allows the riding mass to move more freely. On the other hand an increased understanding of the equations describing the system could be utilized to further correlate the results. This would also provide the ability to further understand and manipulate the phenomena to further increase the structures bandwidth.

REFERENCES

[1] Cvek, M., Mrlik, M., Sevcik, J., & Sedlacik, M. (2018). Tailoring performance, damping, and surface properties of magnetorheological elastomers via particle-grafting technology. *Polymers*, *10*(12), 1411.
doi: 10.3390/polym10121411

[2] Li, Q., Jin, W., Chu, M., Zhang, W., Gu, J., Shahid, B., Zhao, Y. S. (2018). Tailoring the structures and photonic properties of low-dimensional organic materials by crystal engineering. *Nanoscale*, *10*(10), 4680–4685.
doi: 10.1039/c7nr08228b

[3] Shah, M. W., Zhu, Y., Fan, X., Zhao, J., Li, Y., Asim, S., & Wang, C. (2015). Facile synthesis of defective TiO2−x nanocrystals with high surface area and tailoring band gap for visible-light photocatalysis. *Scientific Reports*, *5*(1).
doi: 10.1038/srep15804

[4] Kasai, K., Fu, Y., & Watanabe, A. (1998). Passive control systems for seismic damage mitigation. *Journal of Structural Engineering*, *124*(5), 501–512.
doi: 10.1061/(asce)0733-9445(1998)124:5(501)

[5] Guo, X., Ma, Y., Wang, Y., & Tong, L. (2013). Nanowire plasmonic waveguides, circuits and devices. *Laser & Photonics Reviews*, *7*(6), 855–881.
doi: 10.1002/lpor.201200067

[6] Chronopoulos, D., Antoniadis, I., Collet, M., Ichchou, M. (2015). Enhancement of wave damping within metamaterials having embedded negative stiffness inclusions. *Wave Motion, 58*, 165-179.
doi: https://doi.org/10.1016/j.wavemoti.2015.05.005

[7] Lu, M., Feng, L., Chen Y. (2009). Phononic crystals and acoustic metamaterials. *Materials Today, 12*(12). 34-42.
doi: https://doi.org/10.1016/S1369-7021(09)70315-3

[8] Zhu, R., Huang, G., Huang, H., & Sun, C. (2011). Experimental and numerical study of guided wave propagation in a thin metamaterial plate. *Physics Letters A*, *375*(30-31), 2863–2867.
doi: 10.1016/j.physleta.2011.06.006

[9] Huang, H., Sun, C., & Huang, G. (2009). On the negative effective mass density in acoustic metamaterials. *International Journal of Engineering Science*, 47(4), 610–617.
doi: 10.1016/j.ijengsci.2008.12.007

[10] Huang, H. H., & Sun, C. T. (2009). Wave attenuation mechanism in an acoustic metamaterial with negative effective mass density. *New Journal of Physics*, *11*(1), 013003.
doi: 10.1088/1367-2630/11/1/013003

[11] Huang, G. L., & Sun, C. T. (2010). Band gaps in a multiresonator acoustic metamaterial. *Journal of Vibration and Acoustics*, *132*(3).
doi: 10.1115/1.4000784

[12] Norris, A. N., Acoustic cloaking theory, *Proceedings of the Royal Society A: Mathematical, Physical and Engineering Sciences*, 464, 2411-2434.
doi:10.1098/rspa.2008.0076

[13] Zhao, J., Chen, Z. N., Li, B., & Qiu, C.-W. (2015). Acoustic cloaking by extraordinary sound transmission. *Journal of Applied Physics*, *117*(21), 214507.
doi: 10.1063/1.4922120

[14] Grimberg, R., (2013). Electromagnetic metamaterials, *Materials Science and Engineering: B*, *178*(19), 1285-1295.
doi: https://doi.org/10.1016/j.mseb.2013.03.022

[15] Jiménez, N., Mehrem, A., Picó, R., García-Raffi, L. M., Sánchez-Morcillo, V. J., (2016). Nonlinear propagation and control of acoustic waves in phononic superlattices, *Comptes Rendus Physique*, *17*(5), 543-554.
doi: https://doi.org/10.1016/j.crhy.2016.02.004

[16] Brunet, T., Leng, J., & Mondain-Monval, O. (2013). Soft acoustic metamaterials. *Science*, *342*(6156), 323–324.
doi: 10.1126/science.1241727

[17] Liu, Z. (2000). Locally resonant sonic materials. *Science*, *289*(5485), 1734–1736.
doi: 10.1126/science.289.5485.1734

[18] Chang, I.-L., Liang, Z.-X., Kao, H.-W., Chang, S.-H., & Yang, C.-Y. (2018). The wave attenuation mechanism of the periodic local resonant metamaterial. *Journal of Sound and Vibration*, *412*, 349–359.
doi: 10.1016/j.jsv.2017.10.008

[19] Liang, Z., Li, J., (2011) Extreme acoustic metamaterial by coiling up space. *Physical Review Letters, 108*.
doi: 10.1103/PhysRevLett.108.114301

[20] Luukkala, M., Heikkila, P., & Surakka, J. (1971). Plate wave resonance — a contactless test method. *Ultrasonics*, *9*(4), 201–208.
doi: 10.1016/0041-624x(71)90387-8

[21] Amireddy, K. K., Balasubramaniam, K., & Rajagopal, P. (2017). Deep subwavelength ultrasonic imaging using optimized holey structured metamaterials. *Scientific Reports*, *7*(1).
doi: 10.1038/s41598-017-08036-4

[22] Zangeneh-Nejad, F., & Fleury, R. (2019). Active times for acoustic metamaterials. *Reviews in Physics*, *4*, 100031.
doi: 10.1016/j.revip.2019.100031

[23] Zhang, Y., Song, Z., Wang, X., Cao, W., & Au, W. W. L. (2017). Directional acoustic wave manipulation by a porpoise via multiphase forehead structure. *Physical Review Applied*, *8*(6).
doi: 10.1103/physrevapplied.8.064002

[24] Herbold, E. B., & Nesternko, V. F. (2015). Solitary and shock waves in strongly nonlinear metamaterials, *AIP Conference Proceedings, 955*(231).
https://doi.org/10.1063/1.2833017

[25] Khajehtourian, R., & Hussein, M. I. (2014). Dispersion characteristics of a nonlinear elastic metamaterial. *AIP Advances*, *4*(12), 124308.
doi: 10.1063/1.4905051

[26] Ba'ba'a, H. A., Attarzadeh, M. A., & Nouh, M. (2018). Experimental evaluation of structural intensity in two-dimensional plate-type locally resonant elastic metamaterials. *Journal of Applied Mechanics*, *85*(4).
doi: 10.1115/1.4039042

[27] Peng, H., & Pai, P. F. (2014). Acoustic metamaterial plates for elastic wave absorption and structural vibration suppression. *International Journal of Mechanical Sciences*, *89*, 350–361.
doi: 10.1016/j.ijmecsci.2014.09.018

[28] Li, Y., Zhu, L., & Chen, T. (2017). Plate-type elastic metamaterials for low-frequency broadband elastic wave attenuation. *Ultrasonics*, *73*, 34–42.
doi: 10.1016/j.ultras.2016.08.019

[29] Nouh, M., Aldraihem, O., & Baz, A. (2015). Wave propagation in metamaterial plates with periodic local resonances. *Journal of Sound and Vibration*, *341*, 53–73.
doi: 10.1016/j.jsv.2014.12.030

[30] Andreassen, E., Manktelow, K., & Ruzzene, M. (2015). Directional bending wave propagation in periodically perforated plates. *Journal of Sound and Vibration*, *335*, 187–203.
doi: 10.1016/j.jsv.2014.09.035

[31] Wu, Y., Yang, M., Sheng, P., (2018). Perspective: Acoustic metamaterials in transition, *Journal of Applied Physics*, *123*, 090901.
https://doi.org/10.1063/1.5007682

[32] Beeby, S. P., Tudor, M. J., & White, N. M. (2006). Energy harvesting vibration sources for microsystems applications. *Measurement Science and Technology*, *17*(12).
doi: 10.1088/0957-0233/17/12/r01

[33] Zhu, R., Liu, X., Hu, G., Yuan, F., & Huang, G. (2015). Microstructural designs of plate-type elastic metamaterial and their potential applications: a review. *International Journal of Smart and Nano Materials*, *6*(1), 14–40.
doi: 10.1080/19475411.2015.1025249

[34] Chappell, J., Sloman, A., (2005). Natural and artificial meta-configured altricial information-processing systems, *International Journal of Unconventional Computing, 3.3*, 211-239

[35] Kern, S., (1875). "New method of quantitative analysis of ordinary alloys". *Chemical News and Journal of Industrial Science*. London: Chemical news office. XXXI (795): 76

[36] Quinquenet, S., Ollivon, M., Grabielle-Madelmont, C., & Serpelloni, M. (1988). Polimorphism of hydrated sorbitol. *Thermochimica Acta*, *125*, 125–140.
doi: 10.1016/0040-6031(88)87217-4

[37] Emerson, T. A., Lozzi, A., Bai, H., and Manimala, J. M. (2018). *Dynamic characterization and control of a metamaterials-inspired smart composite*. San Antonio, Tx. ASME Smart Materials, Adaptive Structures and Intelligent Systems (SMASIS) conference.

[38] Veelaert, P., & Bogaerts, W. (1999). Ultrasonic potential field sensor for obstacle avoidance. *IEEE Transactions on Robotics and Automation*, *15*(4), 774–779.
doi: 10.1109/70.782033

[39] Gibbs, G., Jia, H., & Madani, I. (2017). Obstacle detection with ultrasonic sensors and signal analysis metrics. *Transportation Research Procedia*, *28*, 173–182.
doi: 10.1016/j.trpro.2017.12.183

[40] Borriello, G., Liu, A., Offer, T., Palistrant, C., Sharp, R., *WALRUS: Wireless acoustic location with room-level resolution using ultrasound*, Seattle, Wa. Proceedings of the 3rd International Conference on Mobile Systems (MobiSYS).

[41] Liu, B., Luo, Z., & Gang, T. (2017). Influence of low-frequency parameter changes on nonlinear vibro-acoustic wave modulations used for crack detection. *Structural Health Monitoring*, *17*(2), 218–226.
doi: 10.1177/1475921716689385

[42] Cummer, S. A., Christensen, J., & Alù, A. (2016). Controlling sound with acoustic metamaterials. *Nature Reviews Materials*, *1*(3).
doi: 10.1038/natrevmats.2016.1

[43] Martynowicz, P. (2015). Vibration control of wind turbine tower-nacelle model with magnetorheological tuned vibration absorber. *Journal of Vibration and Control*, *23*(20), 3468–3489.
doi: 10.1177/1077546315591445

[44] Wright, R. I., & Kidner, M. R. F. (2004). Vibration absorbers: A review of applications in interior noise control of propeller aircraft. *Journal of Vibration and Control*, *10*(8), 1221–1237. doi: 10.1177/1077546304041368

[45] Elias, S. (2018). Seismic energy assessment of buildings with tuned vibration absorbers. *Shock and Vibration*, 2018, 1–10. doi: 10.1155/2018/2051687

[46] Xiang, H. J., Shi, Z. F., Wang, S. J., & Mo, Y. L. (2012). Periodic materials-based vibration attenuation in layered foundations: experimental validation. *Smart Materials and Structures*, *21*(11), 112003. doi: 10.1088/0964-1726/21/11/112003

[47] Fang, N., Xi, D., Xu, J., Ambati, M., Srituravanich, W., Sun, C., & Zhang, X. (2006). Ultrasonic metamaterials with negative modulus. *Nature Materials*, *5*(6), 452–456. doi: 10.1038/nmat1644

[48] Krushynska, A. O., Bosia, F., Miniaci, M., & Pugno, N. M. (2017). Spider web-structured labyrinthine acoustic metamaterials for low-frequency sound control. *New Journal of Physics*, *19*(10), 105001. doi: 10.1088/1367-2630/aa83f3

[49] C. Sheehan, S. Valiya Valappil, and J. M. Manimala (2018). *Passive Mechanical Wave Manipulation using Nonlinear Metamaterials.* San Antonio, Tx. ASME Smart Materials, Adaptive Structures and Intelligent Systems (SMASIS) conference.

[50] Rao, S. S., (2004). Mechanical Vibrations

[51] Ormondroyd, J., & DenHartog, J. P., (1928). The theory of the dynamic vibration absorber, *Journal of Applied Mechanics*, *50*, 9-22.

[52] Ozer, M. B., & Royston, T. J. (2004). Extending Den Hartog's vibration absorber technique to multi-degree-of-freedom systems. *Journal of Vibration and Acoustics*, *127*(4), 341–350. doi: 10.1115/1.1924642

[53] Kitis, L., Wang, B., & Pilkey, W. (1983). Vibration reduction over a frequency range. *Journal of Sound and Vibration*, *89*(4), 559–569. doi: 10.1016/0022-460x(83)90357-7

[54] Snowdon, J. (1975), Platelike dynamic vibration absorbers. *Journal of Manufacturing Science and Engineering*. 97(1). https://doi.org/10.1115/1.3438595

[55] Kerlin, R. (1988). Predicted attenuation of the plate-like dynamic vibration absorber when attached to a clamped circular plate at a non-central point of excitation. *Applied Acoustics*, *23*(1), 17–27. doi: 10.1016/0003-682x(88)90078-3

[56] Yang, C., Li, D., & Cheng, L. (2011). Dynamic vibration absorbers for vibration control within a frequency band. *Journal of Sound and Vibration*, *330*(8), 1582–1598. doi: 10.1016/j.jsv.2010.10.018

[57] Ryaboy, V. M. (2016). Practical aspects of design, tuning and application of dynamic vibration absorbers. *Proceedings of Meetings on Acoustics*, *26*. doi: 10.1121/2.0000231

[58] Bian, Y., Liang, X., & Gao, Z. (2018). Vibration reduction for a flexible arm using magnetorheological elastomer vibration absorber. *Shock and Vibration*, 2018, 1–13. doi: 10.1155/2018/9723538

[59] Lerner, A. A., & Cunefare, K. (2007). Performance of MRE-based vibration absorbers. *Journal of Intelligent Material Systems and Structures*, *19*(5), 551–563. doi: 10.1177/1045389x07077850

[60] Herzog, R., (1994). Active versus passive vibration absorbers, *Journal of Dynamic Systems Measurement and Control*, *116.* DOI: 10.1115/1.2899231

[61] Borglund, D., & Kuttenkeuler, J. (2002). Active wing flutter suppression using a trailing edge flap. *Journal of Fluids and Structures*, *16*(3), 271–294. doi: 10.1006/jfls.2001.0426

[62] Verstraelen, E., Habib, G., Kerschen, G., & Dimitriadis, G. (2017). Experimental passive flutter suppression using a linear tuned vibration absorber. *AIAA Journal*, *55*(5), 1707–1722. doi: 10.2514/1.j055397

[63] Williams, K., Chiu, G., & Bernhard, R. (2002). Adaptive-passive absorbers using shape-memory alloys. *Journal of Sound and Vibration*, *249*(5), 835–848. doi: 10.1006/jsvi.2000.3496

[64] Abhishek, G., Manobala, K. (2018). Development of actively tuned vibration absorber for washing machine, *International Research Journal of Engineering and Technology*, *5*(4)

[65] Sun, J. Q., Jolly, M. R., & Norris, M. A. (1995). Passive, adaptive and active tuned vibration absorbers—A Survey. *Journal of Vibration and Acoustics*, *117*(B), 234–242. doi: 10.1115/1.2838668

[66] "US bolts - tightening torques." Engineering ToolBox, www.engineeringtoolbox.com/us-bolts-torques-d_2055.html.

[67] Irvine, T. (n.d.). Bending frequencies of beams, rods, and pipes . Retrieved from http://www.vibrationdata.com/tutorials2/beam.pdf

[68] Tao, H., Strikwerda, A. C., Fan, K., Padilla, W. J., Zhang, X., & Averitt, R. D. (2010). MEMS based structurally tunable metamaterials at terahertz frequencies. *Journal of Infrared, Millimeter, and Terahertz Waves*, *32*(5), 580–595.
doi: 10.1007/s10762-010-9646-8

[69] Hedayati, R., Leeflang, A. M., & Zadpoor, A. A. (2017). Additively manufactured metallic pentamode meta-materials. *Applied Physics Letters*, *110*(9), 091905.
doi: 10.1063/1.4977561

APPENDICES

APPENDIX A

A-1 Metamaterials-Inspired Smart Composite

Drawing inspiration from the meta-structures investigated in this work, a 'metamaterials-inspired smart composite' plate deemed the MISC pate combining vibration isolation, energy harvesting and potentially structural health monitoring was designed and manufactured. Its internal multifunctional resonator plate was made using stainless steel utilizing a chemical etching process. An initial "simple" cantilever design was created as shown in figure A-1, however, the tri-pronged design was formed to create a symmetrical effect and avoid the preferential pickup of the simple design. While the tri-pronged design gave symmetry it also stiffened the structure so a third "re-entrant" design was formed and manufactured for use.

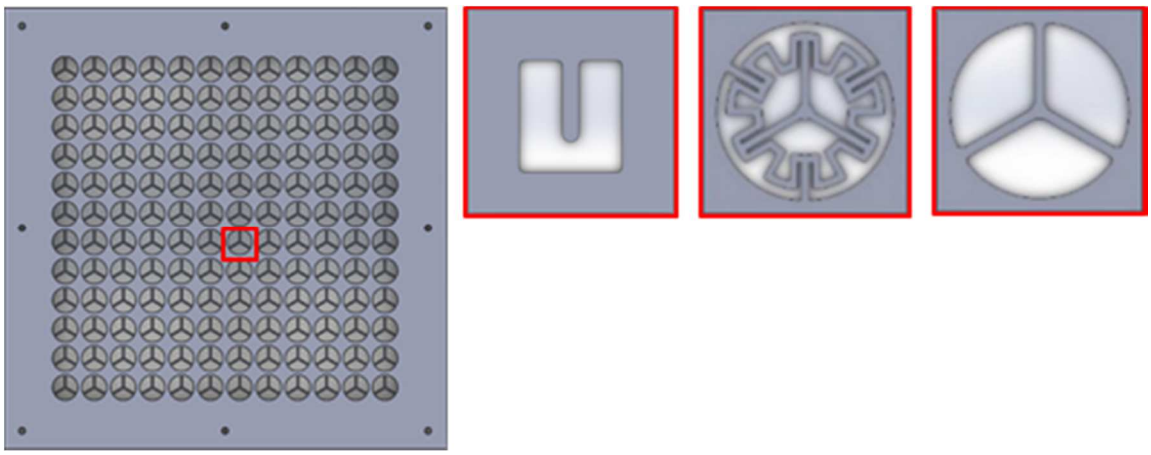

Figure A-1: [left to right] Tri pronged plate, and Simple, Tri-pronged, Reentrant design unit cell.

An understanding of the model is created by assuming a harmonic base excitation using an input displacement (y_0) and a circular frequency (ω). The equation of motion of the tip magnets can be derived by:

$$m\ddot{y_1} + c\dot{y_1} + ky_1 = ky_0\sin(\omega t) + c\omega y_0\cos(\omega t) \quad (A1)$$

Where c and k are the damping coefficients and stiffness of the single unit.

$$y_1(t) = y_0(t)\sin(\omega t) \quad (A2)$$

The tip deflection can be calculated by:

$$y_2(t) = a_0 \sin(\omega t + \emptyset) \quad (A3)$$

With,

$$a_0 = y_0\left[\frac{1 + \left(2\zeta\frac{\omega}{\omega_0}\right)^2}{\left(1 - \frac{\omega}{\omega_0}\right)^2 + \left(2\zeta\frac{\omega}{\omega_0}\right)^2}\right] \quad (A4)$$

$$\emptyset = \tan^{-1}\left[\frac{-2\zeta\left(\frac{\omega}{\omega_0}\right)^3}{1 - (1 - 4\zeta^2)\left(\frac{\omega}{\omega_0}\right)^2}\right] \quad (A5)$$

Where ζ is the damping ratio given by

$$\zeta = \frac{c}{2\sqrt{km}} \quad (A6)$$

The assumptions of the magnet acting only in the y direction, and heating losses are neglected, and back EMF flow being neglected allows the use of Faradays law giving:

$$emf = -NA\,\frac{6\mu\mu_o\omega}{4\pi}\left(\frac{a_o\cos(\omega t + \emptyset) - y_o\cos(\omega t)}{[d_o - a_o sin(\omega t + \emptyset) + y_o\sin(\omega t)]^4} - \frac{a_o\cos(\omega t + \emptyset) - y_o\cos(\omega t)}{[d_o + a_o\sin(\omega t + \emptyset) - y_o\sin(\omega t)]^4}\right) \quad (A7)$$

However, to understand the multi-unit array a more complex approach is taken, one that effectively preserves the mass, resonance frequency, and the plate's stiffness. To model the plate system a lumped mass approach shown in figure A-2 is taken based on the unit-cell design coupled with the overall plate design.

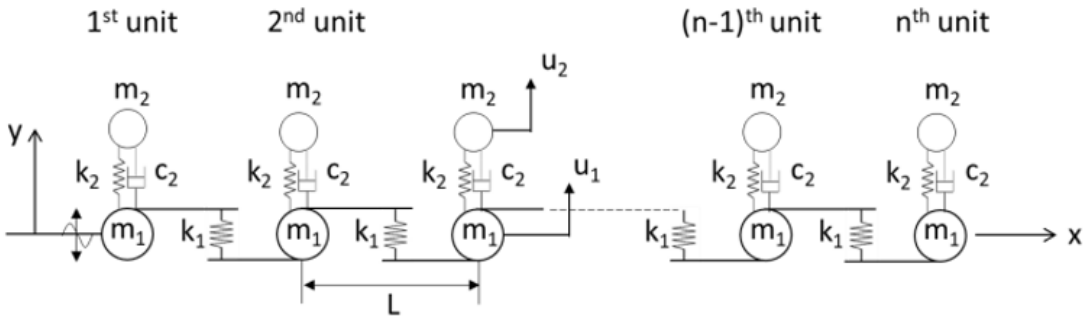

Figure A-2: Reduced order model for the MISC plate configuration.

The resulting forces are summed up into a matrix as in figure A-3 and since a harmonic solution was assumed a linear matrix can be configured to solve for the unknown amplitudes. A single force is assumed to act on the plate since there is a single input excitation source. An unknown within the equations is that of the damping since without experimental results this would be unknown so for later cases on the plate damping is considered 1.0.

$$\begin{Bmatrix} u_1^{(1)} \\ u_2^{(1)} \\ u_1^{(2)} \\ \vdots \\ \vdots \\ \vdots \\ \vdots \\ u_1^{(n)} \\ u_2^{(n)} \end{Bmatrix} = \begin{bmatrix} A_1 & A_2 & A_3 & & & & & & & \\ A_4 & A_5 & 0 & & \cdots & & & 0 & & \\ A_3 & 0 & 0 & & & & & & & \\ & & & \ddots & A_2 & A_3 & 0 & 0 & 0 \\ & \vdots & & & A_4 & A_5 & 0 & 0 & 0 & 0 \\ & & & & A_3 & 0 & A_6 & A_2 & A_3 & 0 \\ & & & & 0 & 0 & A_4 & A_5 & 0 & 0 \\ & 0 & & & 0 & 0 & A_3 & 0 & A_1 & A_2 \\ & & & & 0 & 0 & 0 & 0 & A_3 & A_5 \end{bmatrix}^{-1} \begin{Bmatrix} \bar{F}/m_1 \\ 0 \\ 0 \\ \vdots \\ \vdots \\ \vdots \\ \vdots \\ 0 \end{Bmatrix}$$

Where the values for A_1 to A_6 are:

$$A_1 = \left(-\omega^2 + \frac{k_1}{m_1} + \frac{k_2}{m_1} - i\omega\frac{c_2}{m_1}\right) \qquad (A8a)$$

$$A_2 = \left(-\frac{k_2}{m_1} + i\omega\frac{c_2}{m_1}\right) \tag{A8b}$$

$$A_3 = \left(-\frac{k_1}{m_1}\right) \tag{A8c}$$

$$A_4 = \left(-\frac{k_2}{m_1} + i\omega\frac{c_2}{m_1}\right) \tag{A8d}$$

$$A_5 = \left(-\omega^2 + \frac{k_2}{m_1} - i\omega\frac{c_2}{m_1}\right) \tag{A8e}$$

$$A_6 = \left(-\omega^2 + \frac{2k_1}{m_1} + \frac{k_2}{m_1} - i\omega\frac{c_2}{m_1}\right) \tag{A8f}$$

After understanding the forces acting on the plate, the ability to correlate the results with experimental results was given. After manufacturing the re-entrant design the plate was sandwiched between a core and face sheet as shown in figure A-3. Neodymium magnets were attached at the center of the resonators for energy harvesting purposes and an array of coils were wound about offsets on the core plate. The plates are sandwiched between two face sheets allowing uniform stiffness throughout the configuration.

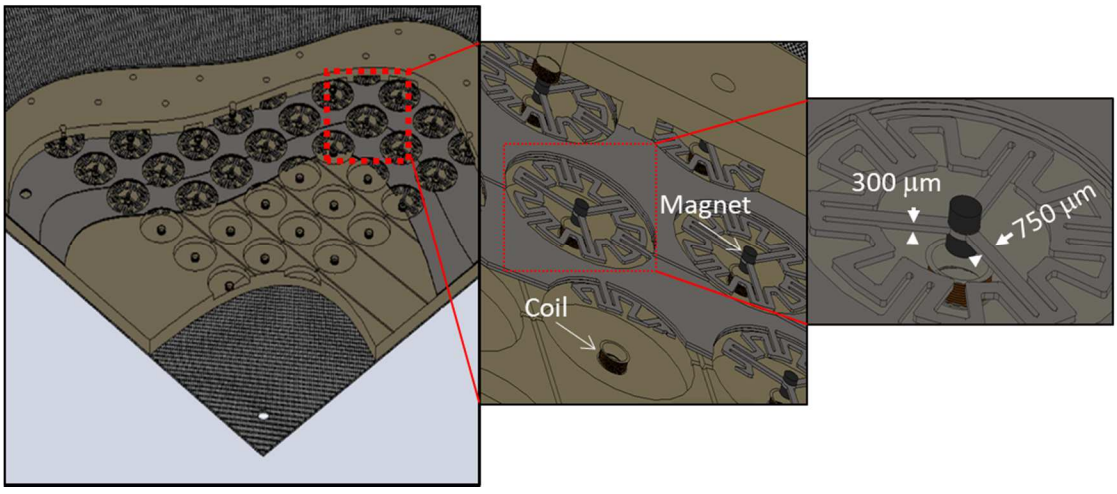

Figure A-3: Cutaway views of the CAD model for the reentrant array test article.

The first test configured on the resonators was a tap test, this shows the time displacement history of the cantilever beam unit, which allows the finding of the damping coefficient to be 0.31. The second test on the cantilever beam unit was an EMF generation test; both tests are shown in figure A-3. When comparing the max values between the simulation and experiment results, 114 Hz and 120 Hz respectively, there is seen to be a close correlation, but not quite an exact correlation. It is also seen that the EMF generated for simulations is around 1.0 while the experimental has a voltage of 0.81 mV, which is about 20% off what is expected, these differences can be explained due to electromagnetic losses.

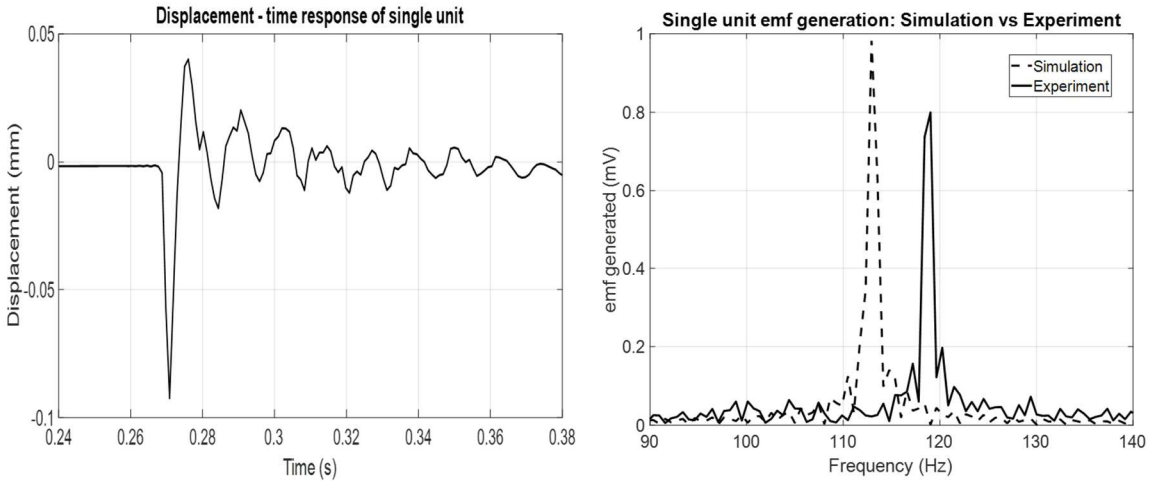

Figure A-4: [left to right] Single unit tap test; Comparison of single unit EMF spectra.

A further study of the EMF output for the tri pronged design over a range of frequencies is shown in figure A-4, however, a damping coefficient is assumed as 1.0 due to the complexities of the plate. From simulations, the natural frequency comes to be 323.71 Hz with a maximum EMF value of 0.75 mV. However, the experimental results showed that the EMF output comes out as 0.66 mV at a frequency of 350 Hz. Further testing the tri pronged design at specific locations such as the S(1,1) location shows a maximum EMF output of 0.6 mV at the 323.71 Hz, while experiments give 0.45 mV at the same location. The plate pickup locations are shown within figure A-5, in which S(1,1) is nearest the shaker head and the S(6,6) location is at the center of the plate.

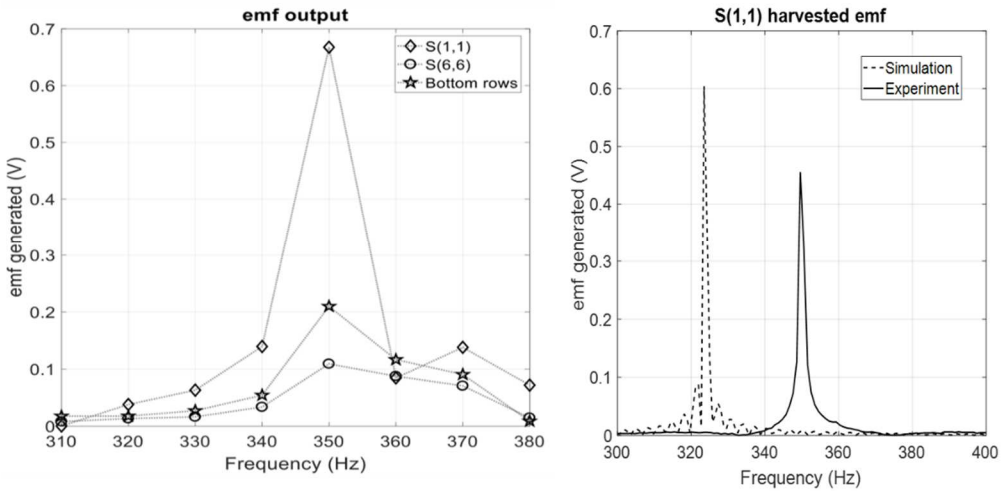

Figure A-5: [left to right] EMF harvested for tri-pronged plate, Comparison of simulated and experimental peak EMF at cell S(1,1).

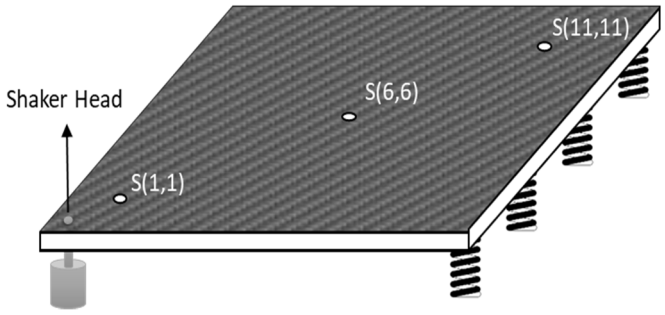

Figure A-6: Locations of monitored units.

APPENDIX B

B-1 Base-Attached PATVA 'Left' Cantilever Results

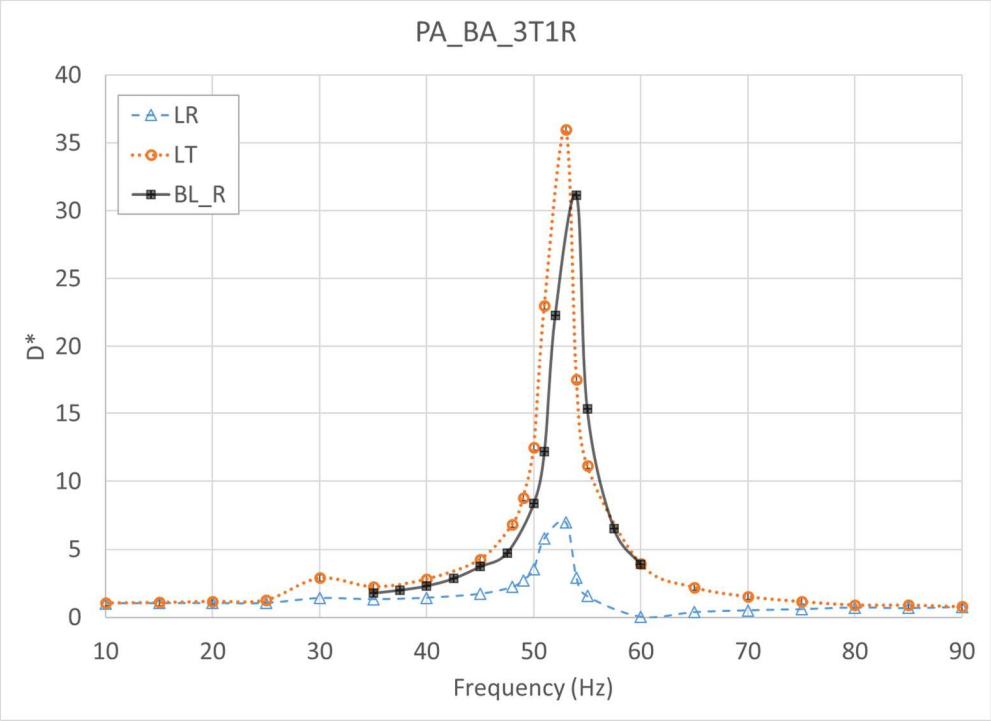

Figure B-1: Normalized displacement transmissibility for the base-attached passive-adaptive TVA with 3 tip and 1 riding masses.

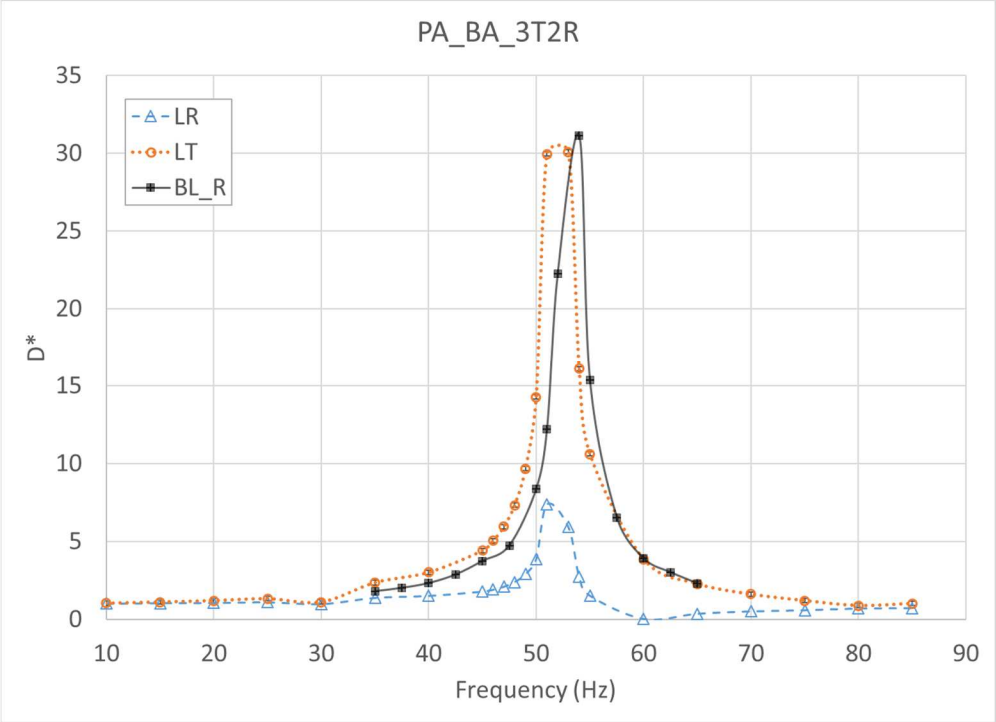

Figure B-2: Normalized displacement transmissibility for the base-attached passive-adaptive TVA with 3 tip and 2 riding masses.

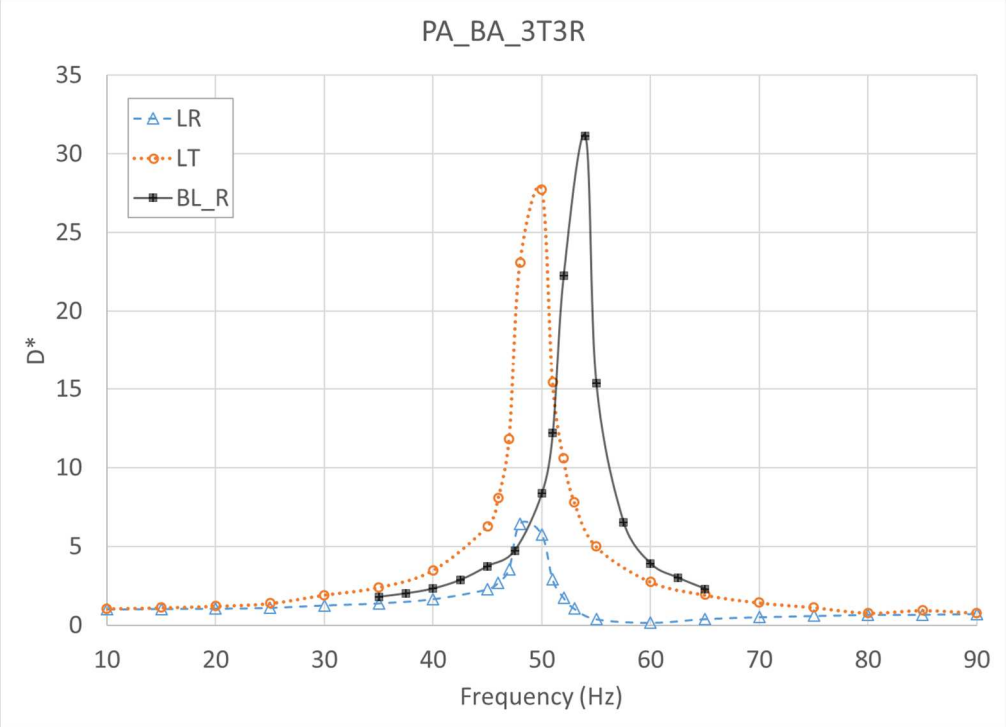

Figure B-3: Normalized displacement transmissibility for the base-attached passive-adaptive TVA with 3 tip and 3 riding masses

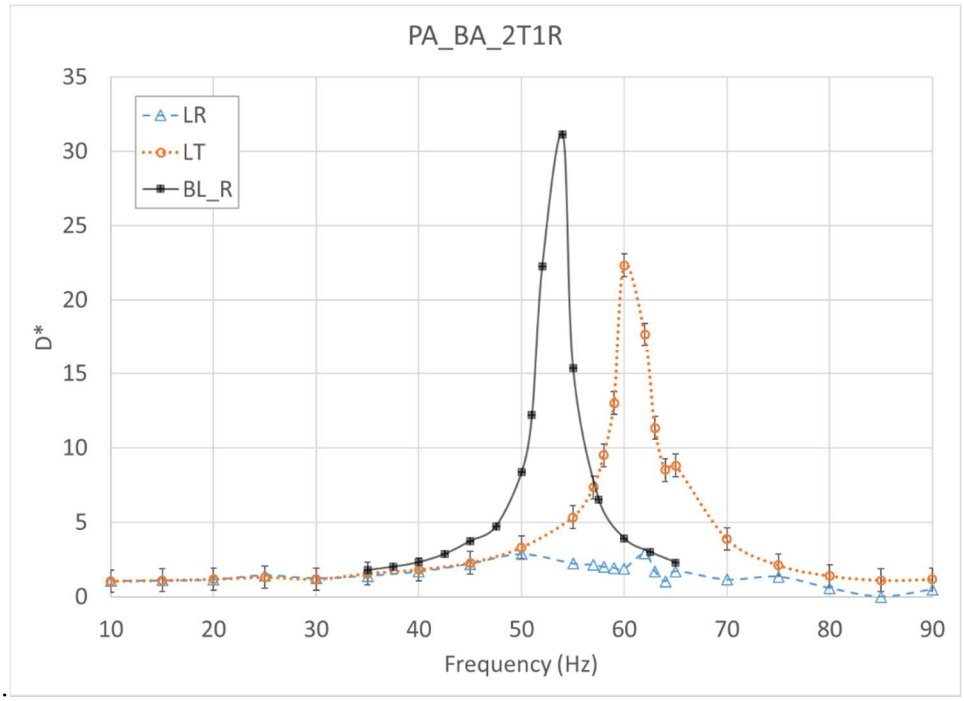

Figure B-4: Normalized displacement transmissibility for the base-attached passive-adaptive TVA with 2 tip and 1 riding masses.

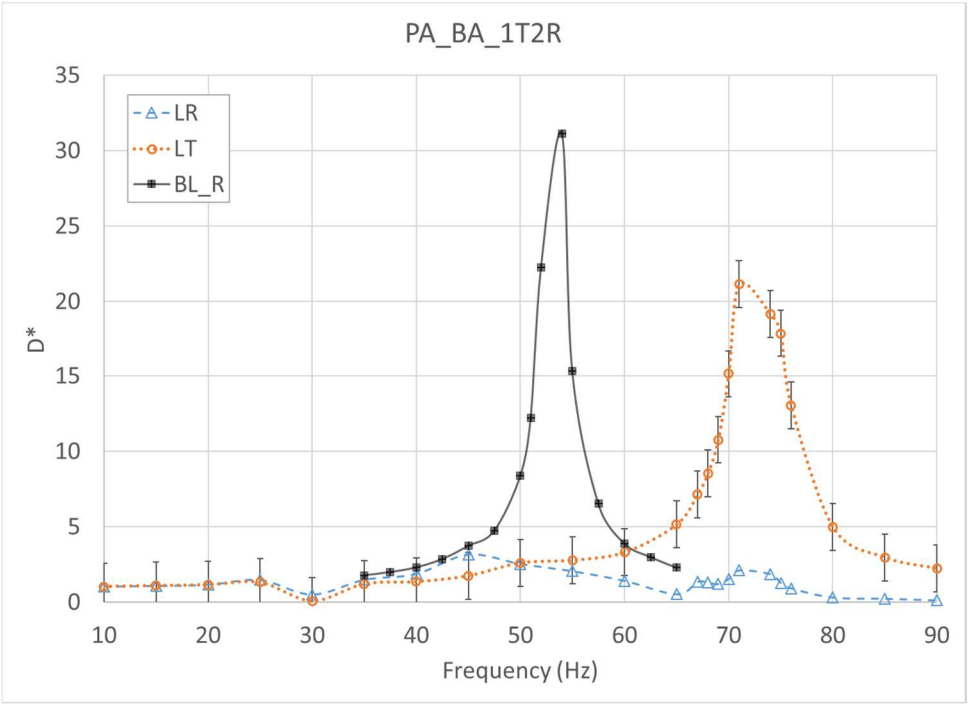

Figure B-5: Normalized displacement transmissibility results for the passive-adaptive base-attached TVA with 1 tip and 2 riding masses.

B-2 Tip-Attached PATVA 'Left' Cantilever Results

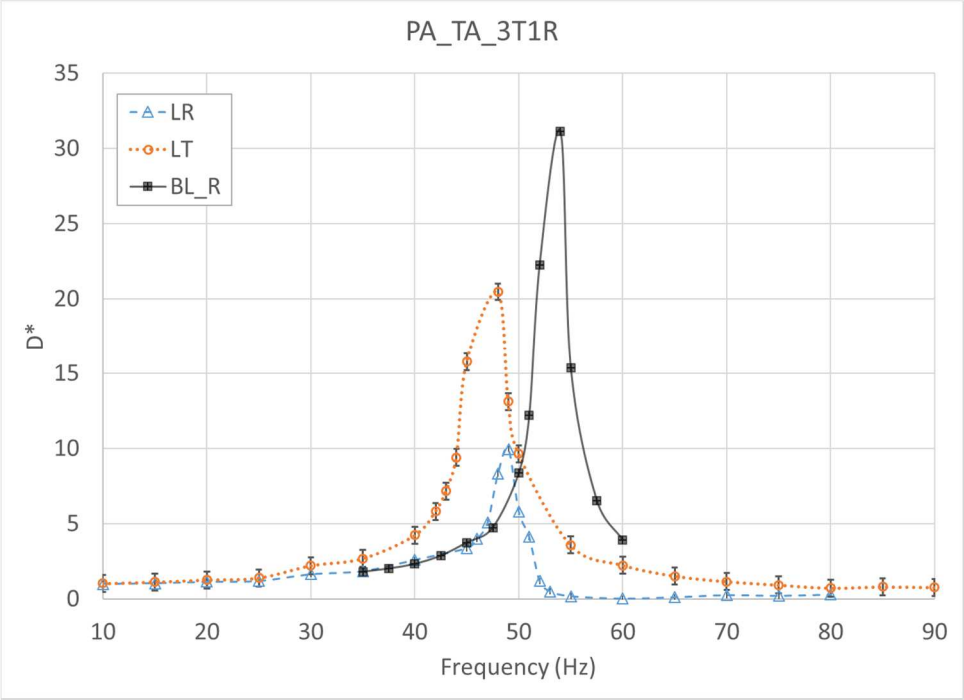

Figure B-5: Normalized displacement transmissibility for the tip-attached passive-adaptive TVA with 3 tip and 1 riding masses.

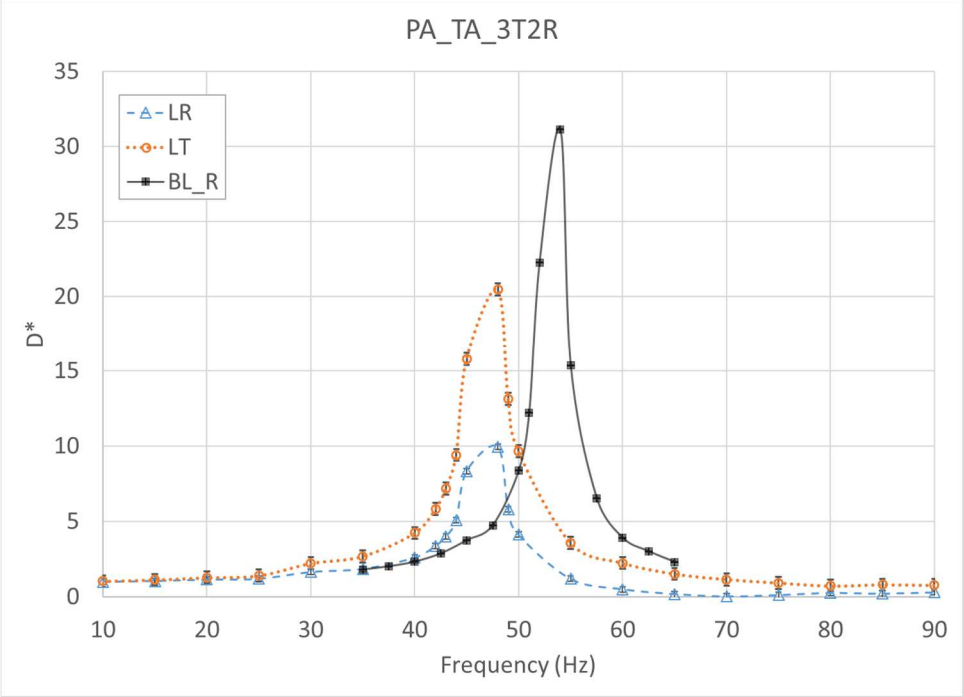

Figure B-6: Normalized displacement transmissibility for the tip-attached passive-adaptive TVA with 3 tip and 2 riding masses.

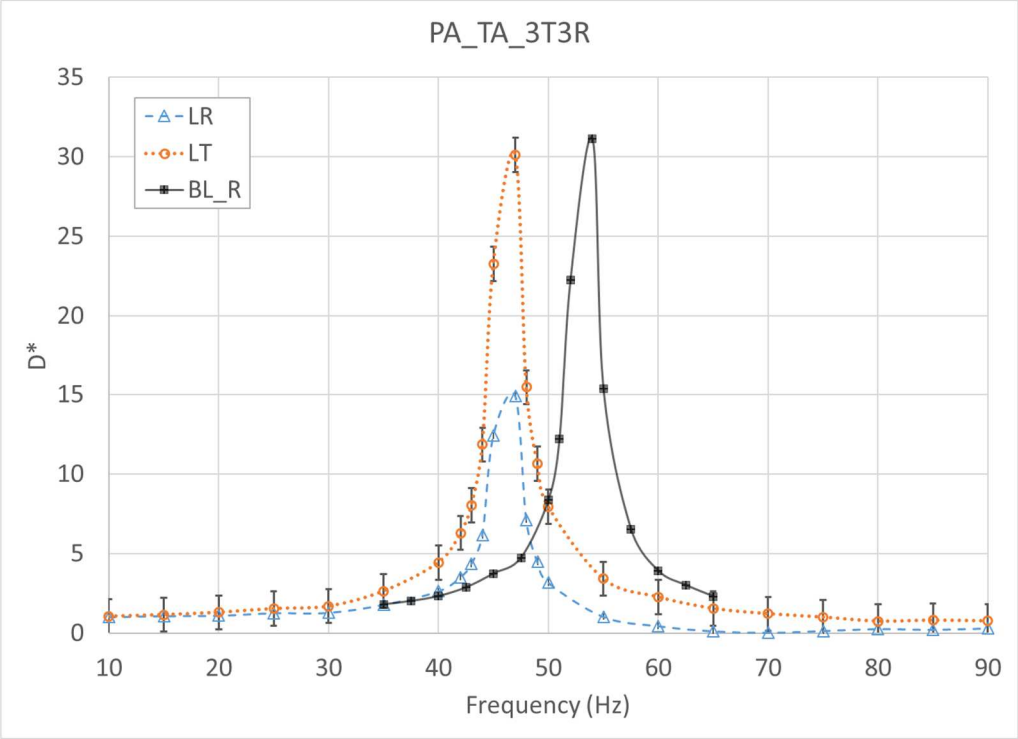

Figure B-7: Normalized displacement transmissibility for the tip-attached passive-adaptive TVA with 3 tip and 3 riding masses.

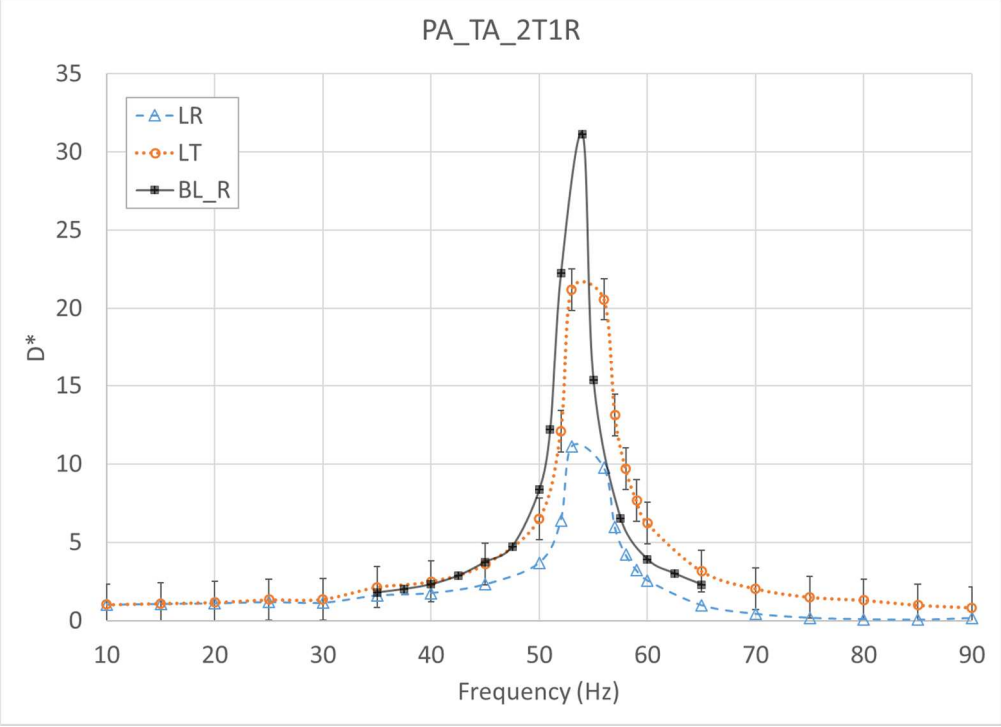

Figure B-8: Normalized displacement transmissibility for the tip-attached passive-adaptive TVA with 2 tip and 1 riding masses.

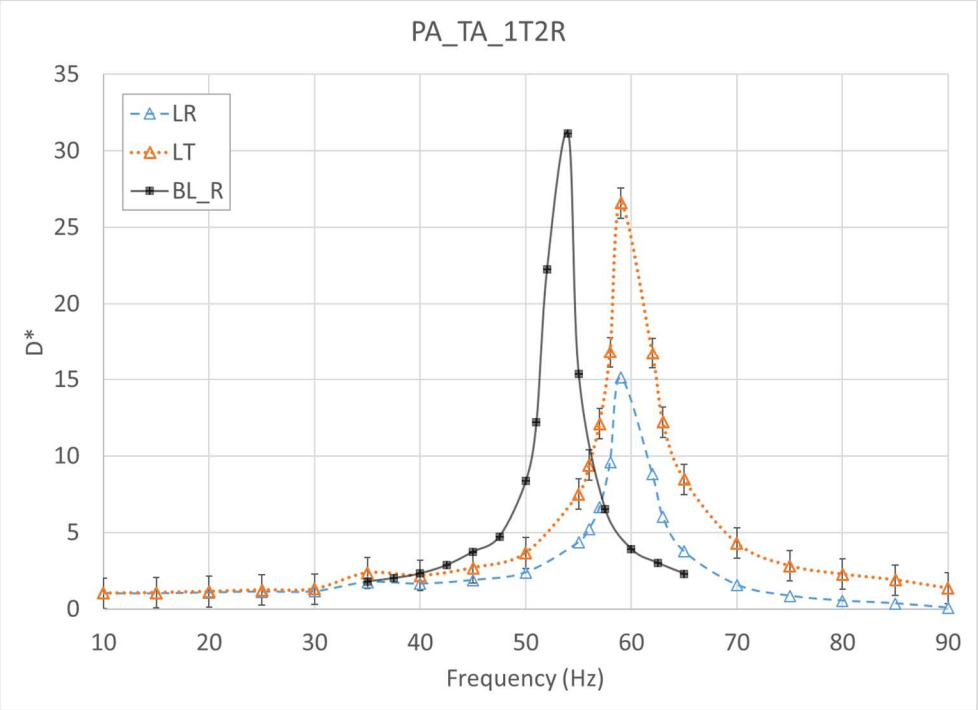

Figure B-9: Normalized displacement transmissibility for the tip-attached passive-adaptive TVA with 1 tip and 2 riding masses.

VITA

Timothy Allen Emerson

Candidate for the Degree of

Master of Science

Thesis: EXPERIMENTAL DYNAMIC CHARACTERIZATION OF META-CONFIGURED STRUCTURES FOR AEROSPACE APPLICATIONS

Major Field: Mechanical and Aerospace Engineering

Biographical:

Education:

Completed the requirements for the Master of Science in Mechanical and Aerospace Engineering at Oklahoma State University, Stillwater, Oklahoma in July, 2020.

Completed the requirements for the Bachelor of Science in Mechanical Engineering at Oklahoma State University, Stillwater, Ok, 2018.

Experience:

Graduate Research Assistant — August 2018-March 2020
Solid and Structural Dynamics Lab, OSU

Systems Engineer II — March 2020-Present
The Boeing Company, OKC, OK

Journal Publications:

1. T. Emerson and J. M. Manimala, "Passive-Adaptive Mechanical Wave Manipulation using Nonlinear Metamaterial Plates," Acta Mechanica, 2020 (Accepted)

Conference Publications:

1. T. Emerson, A. Lozzi, H. Bai, and J. M. Manimala, "Dynamic Characterization and Control of a Metamaterials-Inspired Smart Composite," In proceedings of the ***ASME Smart Materials, Adaptive Structures and Intelligent Systems (SMASIS) conference***, San Antonio, TX, Sep, 2018
2. T. Emerson and J. M. Manimala, "Towards Engineering Metamaterials-Inspired Smart Composites," presented at the ***2nd Annual MAE Graduate Research Symposium***, Oklahoma State University, Stillwater, OK, Nov 2018